

# The Future of Memristors: Materials Engineering and Neural Networks

Kaixuan Sun, Jingsheng Chen, and Xiaobing Yan\*

**From Deep Blue to AlphaGo, artificial intelligence and machine learning are booming, and neural networks have become the hot research direction. However, due to the size limit of complementary metal–oxide–semiconductor (CMOS) transistors, von Neumann-based computing systems are facing multiple challenges (such as memory walls). As the number of transistors required by the neural network increases, the development of neural networks based on the von Neumann computer is limited by volume and energy consumption. As the fourth basic circuit element, memristor shines in the field of neuromorphic computing. The new computer architecture based on memristor is widely considered as a substitute for the von Neumann architecture and has great potential to deal with the neural network and big data era challenge. This article reviews existing materials and structures of memristors, neurophysiological simulations based on memristors, and applications of memristor-based neural networks. The feasibility and advancement of implementing neural networks using memristors are discussed, the difficulties that need to be overcome at this stage are put forward, and their development prospects and challenges faced are also discussed.**

## 1. Introduction

### 1.1. Historical Background of Memristor

In 1971, Leon Chua reasoned from symmetry arguments that there should be a new element, predicted as the fourth fundamental passive circuit element (in addition to resistor, capacitor, and inductor) in the world, which he called a memristor (short for memory resistor), the circuit symbol of memristor is shown in **Figure 1a**.<sup>[1]</sup> And the resistive switching (RS) effect demonstrated by Hewlett Packard laboratory in 2008, has attracted extensive research attention for its high scalability and versatility.<sup>[2]</sup>

K. Sun, Prof. X. Yan  
 Key Laboratory of Brain-Like Neuromorphic Devices  
 and Systems of Hebei Province  
 College of Electron and Information Engineering  
 Hebei University  
 Baoding 071002, P. R. China  
 E-mail: yanxiaobing@ime.ac.cn  
 Prof. J. Chen, Prof. X. Yan  
 Department of Materials Science and Engineering  
 National University of Singapore  
 Singapore 117576, Singapore

 The ORCID identification number(s) for the author(s) of this article can be found under <https://doi.org/10.1002/adfm.202006773>.

DOI: [10.1002/adfm.202006773](https://doi.org/10.1002/adfm.202006773)

In recent years, as Gordon Moore predicted that the number of transistors on a microprocessor chip doubles every two years or so, the size of complementary metal–oxide–semiconductor (CMOS) transistors has continued to shrink, the performance of digital computers based on CMOS transistors has increased significantly in recent years.<sup>[3]</sup> However, since the establishment of the von Neumann architecture in 1945, basic computers have not been able to escape this architecture.<sup>[4]</sup> In addition, the amount of data has grown exponentially with the advent of the Internet of Things (IoT) and cloud computing. In the next few years, the energy efficiency and processing speed of computers will become important factors restricting development. Therefore, the shortcomings of traditional architecture of digital computers are a growing problem. At the device level, leakage cur-

rent grows up to be a problem as the size of the transistor approaches physical limits. At the architectural level, in the von Neumann architecture, the central processing unit (CPU) will be idle while data is being input or output. As the growth rate of CPU speed and memory capacity is much larger than the data traffic between the two parties, the bottleneck problem is becoming more and more serious (von Neumann bottleneck).<sup>[5]</sup> The performance mismatch between the two units leads to a considerable long latency (memory wall),<sup>[6]</sup> which will force processor designs to use heterogeneous cores with high parallelism.<sup>[10]</sup> Graphic processing unit (GPU) with multicore and fast memory access structure is one of the successful attempts to improve computing speed and energy efficiency.<sup>[7,9]</sup> But the delay problem still exists, the delay of the line becomes more important than the delay of the gate. Long lines not only have transmission delay problems, but also energy consumption problems.<sup>[8]</sup>

In-memory computing is resurfacing as an alternative to von Neumann architecture. First proposed in the 1960s,<sup>[11]</sup> in-memory computing can have a simple structure and faster calculation speed—without the need to move data outside the fabric, as shown in **Figure 2**. However, it was not paid enough attention, probably because of the satisfying improvement of computing capability fuelled by the rapid development of transistors in the past few decades. Various emerging electronic devices, taking advantage of physical phenomena such as spin, phase transition or ionic transport,<sup>[12–15]</sup> are becoming more mature both in theory and practice. New computing systems

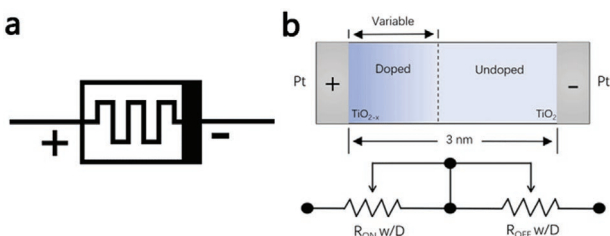


**Figure 1.** a) Memristor symbol. b) The  $\text{Pt}/\text{TiO}_{2-x}/\text{TiO}_2/\text{Pt}$  memristor. Below is the equivalent circuit of the device. b) Adapted with permission.<sup>[2]</sup> Copyright 2008, Springer Nature.

using the in-memory computing concept have built upon these beyond-CMOS devices and nanotechnology, offering an attractive solution to the energy consumption and speed issues. As Moore's Law approaches physical limits, traditional von Neumann buildings are facing challenges.<sup>[16]</sup> Among these, the neural network based on memristor stands out as a promising candidate.

## 1.2. The Memristor and Spiking Neural Network (SNN)

The memristor, also known as a RS, is an electronic device whose internal states are dependent on the history of the current and/or voltage that has experienced.<sup>[1,2]</sup> Its resistance can be reversibly switched between a high-resistance state (HRS) and a low-resistance state (LRS) when the bias voltage achieves a certain level. With simple peripheral circuits, pulses are applied and the resulting voltage response allows these two states to represent "1" and "0" in a binary system. At present, resistive random access memory (RRAM) has been mass-produced, but it will take time until it is applied in large-scale. Compared with traditional read-only memory, RRAM has the

characteristics of fast speed, high reliability, nonvolatile, multivalue storage, and high density. These storage characteristics can respond to the needs of emerging applications. At the same time, it is manufactured using a traditional CMOS process and requires only slight adjustments.<sup>[17–31]</sup>

Memristors are usually made of top electrode (TE) and RS layer and bottom electrode (BE) presents a sandwich structure. There are a variety of technologies for fabricating the RS layer, such as atomic layer deposition (ALD),<sup>[32]</sup> sputter,<sup>[33]</sup> pulsed layer deposition (PLD),<sup>[34]</sup> sol-gel process,<sup>[35]</sup> chemical solution deposition (CSD),<sup>[26–28,36]</sup> chemical vapor deposition (CVD),<sup>[37,38]</sup> e-beam evaporation deposition,<sup>[39]</sup> and molecular beam epitaxy (MBE).<sup>[40,41]</sup> Among a variety of fabricating methods, sputter, which can deposit well-controlled thin films, is most popular. CSD is a cost effective and highly flexible method that allows for good film quality at moderate annealing temperatures. ALD is a sophisticated deposition technique that can deposit ultrathin films ( $<10$  nm) of good quality as one of the most promising techniques for bringing memristors into commercialization.<sup>[41,42]</sup> Besides, ALD technology was proved the possibility of control of dopant<sup>[43]</sup> and oxygen vacancy<sup>[44]</sup> as well as tuning of the memristive switching properties via multilayered thin films.<sup>[45]</sup> In addition to the thin film memristor family, nanoparticle assemblies consisting of a large number of nanoparticles could also act as the insulating layer, the fabrication of this type of memristor is simple and inexpensive.<sup>[46,47]</sup>

RS requires only a small amount of energy because memristive switching devices can be made quite small, it can have a very high stack density ( $<2$  nm),<sup>[48]</sup> and the switching speed can be very fast ( $<0.1$  ns).<sup>[49]</sup> Speeds up response time because no information is lost when the device is turned off. In addition, the change in the conductivity of most memristors is the result of ion movement, such as the migration of metal ions,<sup>[50]</sup> oxygen vacancies,<sup>[51]</sup> and carriers captured in the interface state,<sup>[52]</sup> this is very similar to the phenomenon observed

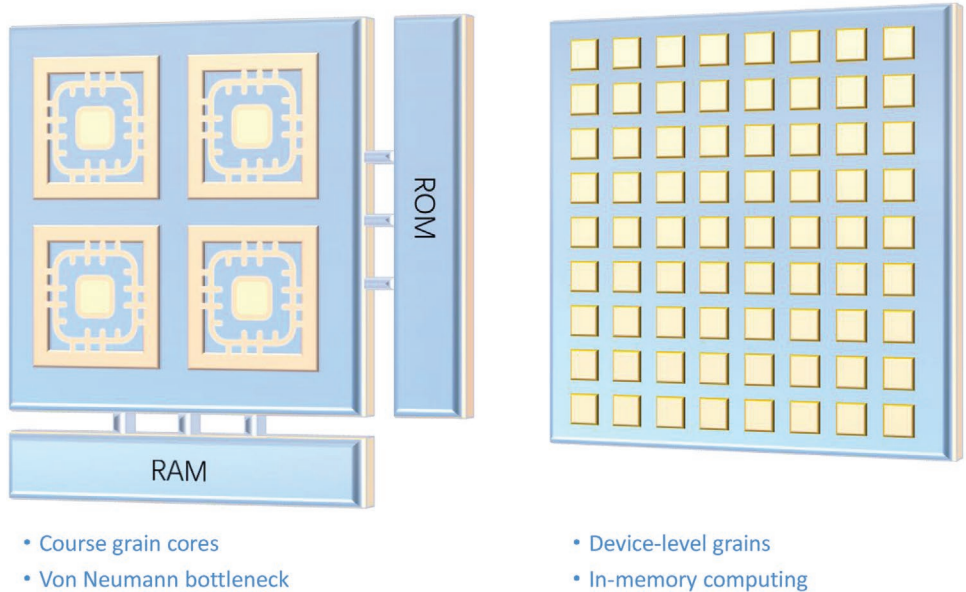


**Figure 2.** A traditional structure in which the CPU is separated from the memory (on the left side) and a memory processing unit (MPU) (right side) for memory computing.

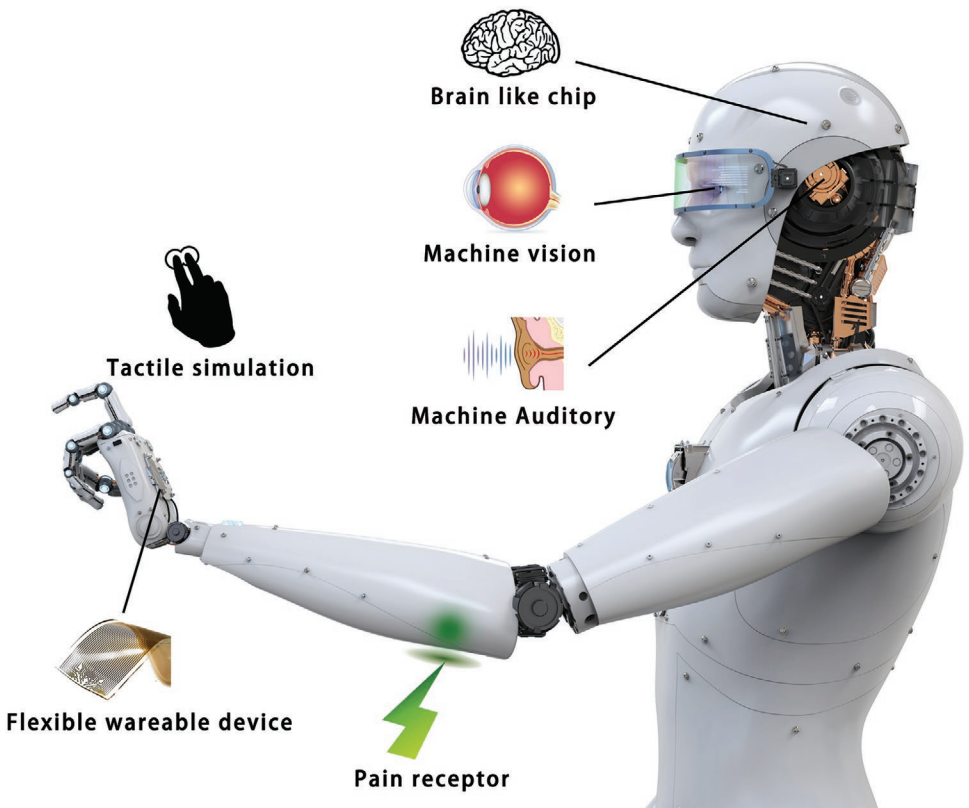


**Figure 3.** The application prospect of memristor in the fields of bionic intelligent products and human–computer interaction.

in biological synapses and neurons. So it can be called brain-like computing. In particular, phase-change memristors can work in a typical neural way with its unique response to pulses.<sup>[53]</sup> SNNs have become the third generation neural network model of future neural networks. It is more energy efficient than artificial neural networks (ANNs), and their size is much small, and low energy consumption,<sup>[56]</sup> similar to or even smaller than the biological nervous system. In recent years, many SNNs have been developed that mimic the actual functions of the biological nervous system through synaptic plasticity, spatiotemporal recognition, long- and short-term memory, and so on.<sup>[54,55]</sup>

Memristors and memristor-based SNNs are bound to be related to today's and tomorrow's computing needs, producing a wide range of applications such as robotics, machine vision, speech recognition, tactile perception, medicine, and cognitive processing, to name a few (Figure 3). Among them, one of the most promising applications of memristors is artificial synapses. Here, we review the existing memristor materials (conventional oxides, 2D materials, etc.) and explain their RS mechanisms in detail (conducting filament or channel of metal ions and oxygen vacancies, etc.), and their association with neurophysiology reveals the basis of brain-like nerve calculations. At the same time, we also pay attention to the advanced application of memristor, neural network technology based on memristors, and the future prospects and challenges of memristors and memristor-based neural networks.

## 2. Investigation of Storage Materials of Memristor

In this chapter, we mainly introduce the materials of oxide, 2D, ferroelectric, and solid electrolyte as RS layers. Table 1 shows a comparison of the recently published memristor electrical parameters (bold items represent the best performance in this column). Although the RS mechanism may vary depending on the electrodes and RS layers (such as oxygen vacancy accumulation or silver ion redox reactions). Stability can be improved by adding additional layers (e.g., a graphene layer) or introducing doping (e.g., doped Au). The electrode materials of these devices are mostly inert metal such as Pt, and TiN electrodes can be used instead to solve the problem of difficult etching in mass production. The long-term performance of these devices looks promising, but variability issues can still affect high and low resistance values.

### 2.1. Conventional Oxides

Similar to the memristor structure used by HP Labs in 2008 (Figure 1b), most memristors are constructed with electrodes and RS layers which usually consist of insulator or semiconductor dielectrics, of which binary oxides account for a large part due to simple fabrication process, compatible with COMS technology, etc. The elements that have been reported to have RS characteristics in binary oxides are shown in Table 2. Among them, silicon oxide ( $\text{SiO}_2$ ),<sup>[84]</sup> titanium oxide ( $\text{TiO}_2$ ),<sup>[85]</sup>

**Table 1.** Summary of electrical performance of memristors with different structures.

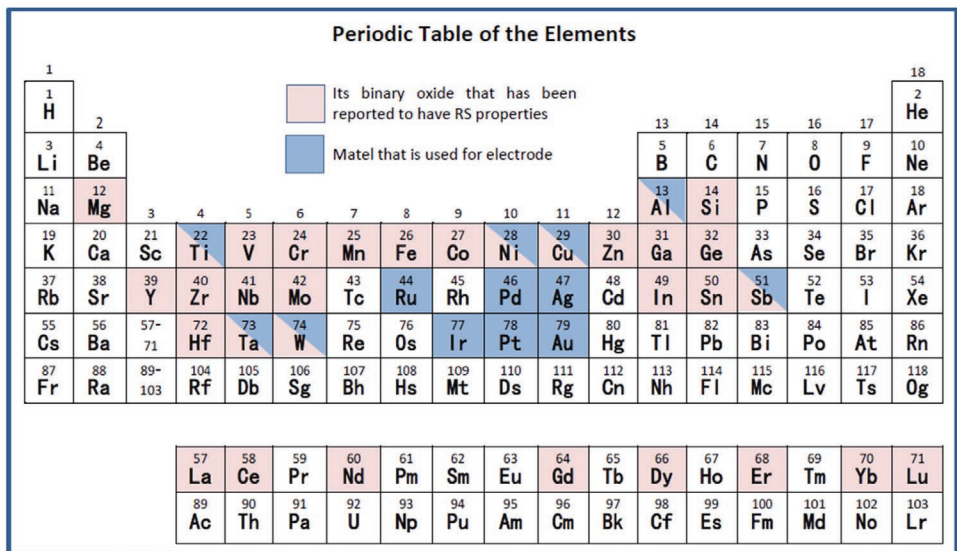
Design principle	Device structure	$R_{\text{off}}/R_{\text{on}}$	$V_{\text{set}}$ [V]	$V_{\text{reset}}$ [V]	$t_{\text{set}}$ [ns]	$t_{\text{reset}}$ [ns]	Endurance/retention	RS mechanism	Ref
High-performance	TiN/Ta <sub>2</sub> O <sub>5</sub> /TiN	360	2.0	-2.0	<10	<10	-	Conductive filament	[57]
Multistate	Au/MoS <sub>2</sub> /Au	10 <sup>7</sup>	3.0	-2.0	-	-	20 cycles/10 <sup>4</sup> s	Schottky barrier	[58]
Quasi-2D halide perovskites	Ag/PEA <sub>2</sub> Cs <sub>3</sub> Pb <sub>4</sub> I <sub>13</sub> /Pt	10 <sup>9</sup>	0.18	-	-	-	200 cycles/2 × 10 <sup>3</sup> s	Schottky barrier	[59]
Bipolar-type RRAM	Pt/TiO <sub>2</sub> /TiN	≈100	+2.0	-2.0	-	-	-	Schottky barrier	[60,71]
Eliminating negative-SET behavior	Ag/ZrO <sub>2</sub> /graphene/Pt	≈10 <sup>10</sup>	1.0 or -2.5	-1.0	<30	<100	10 <sup>4</sup> s	Conductive filament	[61]
Versatile, fully integrative	Au/SAM-SURMOF/Au	10 <sup>6</sup>	±1.0	-	-	-	10 <sup>3</sup> s	Charge trapping/detrapping	[62]
Low work voltage, high off/on resistance	Pt/n-Type TiO <sub>2</sub> /p-Type NiO/Pt	10 <sup>6</sup>	-1.0 to -0.5	0.5–1.0	<150	<150	-	Conductive filament	[63]
Multilevel changes in resistance	ITO/LaAlO <sub>3</sub> /SrTiO <sub>3</sub>	200	-1.3–1.6	5.0	2.5 × 10 <sup>4</sup>	15	>2000 cycles/>10 <sup>4</sup> s	Conductive filament	[64]
Build ANN	Au /Pt/TiO <sub>2-x</sub> /Pt/Ti	5 × 10 <sup>4</sup>	-1.3–0.7	0.7–1.2	200	1000	-	Schottky barrier	[65]
High stability	Ta/HfO <sub>2</sub> /Pd	500	1.1	-1.3	50	50	>10 <sup>6</sup> cycles/10 years@RT	Conductive filament	[66,67]
low-temperature switching	Pt/HfO <sub>x</sub> /TiN	≈10	1.7	-1.6	5 × 10 <sup>4</sup>	5 × 10 <sup>4</sup>	-	Conductive filament	[68]
2D materials	Al/WS <sub>2</sub> /Pt	10 <sup>3</sup>	1.6	-1.5	-	-	>10 <sup>4</sup> cycles/>25 hours	Conductive filament	[69]
High neuromorphic accuracies	Pt/TiN/PCMO/Pt	≈60	-2.5	2.0	10 <sup>4</sup>	10 <sup>4</sup>	-	Schottky barrier	[70,76]
Access device	TE (Cu doped)/MIEC/BE (Cu doped)	≈20	0.25	-0.35	100	-	10 <sup>10</sup> cycles	Ionic transport	[72]
3D CMOS hybrid circuit	Pt/Ti/Al <sub>2</sub> O <sub>3</sub> /TiO <sub>x</sub> /Pt/Ta	10	0.7	-0.7	-	-	>500 cycles/10 <sup>4</sup> s	Schottky barrier	[73]
Self-compliant, highly nonlinear and wide on/off-window	TiN/Al <sub>2</sub> O <sub>3</sub> /TiO <sub>2</sub> /TiN	100	3.0	-	10	10	-	Self-nonlinear memristor Tunneling	[74]
High stability	Cu/a-Si/WO <sub>3</sub> /Pt	-	1.25	-1.25	10 <sup>5</sup>	10 <sup>5</sup>	10 <sup>9</sup> cycles	Space charge limited current	[75]
Low energy consumption	TiN/TaO <sub>x</sub> /HfAl <sub>y</sub> O <sub>x</sub> /TiN	6	2.0	-3.0	50	50	-	Oxygen vacancies	[77]
Excellent selector characteristics	Pt/VO <sub>2</sub> /Pt	50	0.4	-0.4	<20	-	-	Metal-insulator transition	[78]
Ultimate scalability	Pt/Ti/α-SrTiO <sub>3</sub> /Pt	10 <sup>3</sup> –10 <sup>4</sup>	1.9	-1.3	-	-	>10 <sup>6</sup> cycles/>10 <sup>5</sup> s	Schottky barrier	[79]
Unipolar	Ag/Ti/CeO <sub>2-x</sub> /Pt	10 <sup>5</sup>	3.5	1.0	-	-	>10 <sup>4</sup> s	Schottky barrier	[80]
High-density memory	Ag/N-GST/Pt	10 <sup>4</sup>	0.2	-0.14	-	-	10 <sup>5</sup> cycles@85 °C	Phase-change	[81]
Highly transparent	W/egg albumen/ITO/PET	10 <sup>3</sup>	2.0	-			100 cycles/>10 <sup>4</sup> s	Conductive filament	[82]
Low energy consumption	Ag/ZHO/GOQDs/ZHO/Pt	10 <sup>4</sup>	0.08–0.3	-0.14–0.01	13	50	10 <sup>4</sup> s	Conductive filament	[83]

vanadium oxide (VO<sub>2</sub>),<sup>[78]</sup> zirconium oxide (ZrO<sub>2</sub>),<sup>[86]</sup> nickel oxide (NiO),<sup>[87]</sup> zinc oxide (ZnO),<sup>[88]</sup> hafnium oxide (HfO<sub>2</sub>),<sup>[89]</sup> tantalum oxide (Ta<sub>2</sub>O<sub>5</sub>),<sup>[90]</sup> and alumina (Al<sub>2</sub>O<sub>3</sub>)<sup>[91]</sup> are relatively widely studied. Among them, Al<sub>2</sub>O<sub>3</sub> is a very common dielectric material that can be used as a functional layer to limit current, or as an RS layer.<sup>[95,97]</sup> WO<sub>x</sub>-based memristor is forming-free by using a self-aligned feature to enhance the electric field, and has high thermal stability.<sup>[96,98]</sup> TaO<sub>x</sub>-based memristors have extremely high stability and extremely fast switching speeds.<sup>[344,345]</sup> HfO<sub>2</sub>-based memristor has excellent retention and multilevel operation capabilities.<sup>[89]</sup>

More than the RS layer will affect the performance of the memristor, different electrode and dielectric combinations may result in abrupt (digital) or gradual (analog) RS. Devices with abrupt resistance are suitable for memory, similar to binary storage, and devices with gradually changing resistance can be used for multilevel storage of data comparable to analog storage and emulation of biological synapses. For example, for the HfO<sub>2</sub> RS layer, the application of different electrodes may change the switching performance of the memristor and even the RS mode.<sup>[92,93]</sup>

One focus of research is doping and adding a capping layer to improve the performance of oxide-based memristors. Binary

**Table 2.** Summary of the materials that have been used for binary oxide memristor. Metals of the corresponding binary oxides used for the RS layer are colored in pink. Metals used for the electrodes are colored in blue. Adapted with permission.<sup>[31]</sup> Copyright 2012, IEEE.



oxides with dispersed nanoparticles or metallic/semiconducting dopants, such as Pt-dispersed  $\text{SiO}_2$ , Mn-doped  $\text{HfO}_2$ , Na-doped  $\text{WO}_{3-x}$ , Si-doped  $\text{HfO}_2$ , and Si doped  $\text{Ta}_2\text{O}_5$ , have been reported as resistive switching materials.<sup>[337–343]</sup> Such materials exhibit promising switching characteristics such as low variability and low-power operation.<sup>[338,343]</sup> In addition, adding a capping layer can improve the conductance tuning linearity of the memristor, and adjust the electric field and temperature, which are key parameters in neural network applications. Take an example, high durability, high speed and high scalability can be achieved by adding an electrothermal modulation layer or using an asymmetric bilayer structure.<sup>[94,147]</sup> Moreover, oxide-based memristors with a capping layer have become a preferred choice for crossbar arrays at this stage because of their good thermal stability, process compatibility, and multiconductance adjustability.<sup>[248,316]</sup>

## 2.2. 2D Materials

In the field of new materials, the 2D materials represented by graphene because the thickness of the atomic have excellent electrical, optical, thermal, and mechanical properties that traditional materials do not have. The application of 2D materials in the field of functional materials and structural materials has shown great potential, which is expected to be as the foundation materials added in some areas of the future to make the nanoscale electronic devices achieve smaller size, lower power consumption, and higher efficiency.<sup>[99–102]</sup> The 2D materials studied today include a wide variety of materials from conductors and semiconductors to insulators, such as graphene,<sup>[104,105]</sup> BN,<sup>[106,107]</sup> black phosphorus,<sup>[108]</sup> transition metal dichalcogenides (TMDs, such as chalcogenide of W and Mo)<sup>[103,109–111]</sup> and so on, and all of them exhibit superior memristance in small sizes. Figure 4 lists the library of 2D materials.

Layers of 2D materials such as graphene are connected to each other by van der Waals force, and can easily be separated into single layers,<sup>[102]</sup> which has a good application in memristors. Whether it is used as an RS layer<sup>[104,105]</sup> or an electrode,<sup>[112,113]</sup> it shows quite good performance. There are also reports of adding a single layer of graphene between the BE and RS layers, which can prevent conductive wires from penetrating into the bottom electrode.<sup>[114]</sup> In addition to graphene, the RS layers of TMDs memristors have also been extensively studied. Among them, Sangwan et al. studied the complex neuromorphic calculations and defect kinetics in  $\text{MoS}_2$ .<sup>[109,113]</sup> 2D materials exhibit superior memristive properties in small dimensions.

Recently, Yan et al. reported a memristor made of 2D transition metal carbides ( $\text{Ti}_3\text{C}_2\text{T}_x$ ) as a RS layer (Figure 5a,b) and simulated the learning and memory properties of its biological synapses.<sup>[115]</sup> At the same time, they reported a two-terminal artificial electronic device prepared from 2D layered  $\text{WS}_2$  nanosheets (Figure 5c–e) with low power consumption at the femtosecond level.<sup>[116]</sup> Zhang et al. reported the RS characteristics of  $\text{MoTe}_2$  materials and demonstrated the reversible transition of  $\text{MoTe}_2$  devices from 2H semiconductor phase (Figure 5f) to 2Hd high-conductivity phase (Figure 5g) under the action of an electric field. At the same time, as shown in Figure 5h,i, they also used  $\text{Al}_2\text{O}_3/\text{MoTe}_2$  devices to obtain a switching current ratio of  $10^5\text{--}10^6$  and an ultra-HRS over  $10^{12}\ \Omega$ , and can maintain more than  $10^3$  s under ultra HRS, demonstrating the potential of TMDs in this type of RS applications.<sup>[118]</sup>

In fact, 2D materials can not only improve the performance of memristor, but also have great advantages in device preparation process<sup>[117]</sup> and transparent flexible devices. Moreover, many TMDs have unique photoelectric properties, which will be mentioned in Sections 4.2.3. and 6.2. However, there are still some problems that have to be solved in the application of 2D materials. First of all, to realize the application of 2D materials in industry, it is necessary to master the large-area controllable preparation technology of 2D materials, and

Graphene family	Graphene	hBN 'white graphene'	BCN	Fluorographene	Graphene oxide
2D chalcogenides	MoS <sub>2</sub> , WS <sub>2</sub> , MoSe <sub>2</sub> , WSe <sub>2</sub>		Semiconducting dichalcogenides: MoTe <sub>2</sub> , WTe <sub>2</sub> , ZrS <sub>2</sub> , ZrSe <sub>2</sub> and so on	Metallic dichalcogenides: NbSe <sub>2</sub> , NbS <sub>2</sub> , TaS <sub>2</sub> , TiS <sub>2</sub> , NiSe <sub>2</sub> and so on	Layered semiconductors: GaSe, GaTe, InSe, Bi <sub>2</sub> Se <sub>3</sub> and so on
2D oxides	Micas, BSCCO	MoO <sub>3</sub> , WO <sub>3</sub>	Perovskite-type: LaNb <sub>2</sub> O <sub>7</sub> , (Ca,Sr) <sub>2</sub> Nb <sub>3</sub> O <sub>10</sub> , Bi <sub>4</sub> Ti <sub>3</sub> O <sub>12</sub> , Ca <sub>2</sub> Ta <sub>2</sub> TiO <sub>10</sub> and so on	Hydroxides: Ni(OH) <sub>2</sub> , Eu(OH) <sub>2</sub> and so on	Others
	Layered Cu oxides	TiO <sub>2</sub> , MnO <sub>2</sub> , V <sub>2</sub> O <sub>5</sub> , TaO <sub>3</sub> , RuO <sub>2</sub> and so on			

**Figure 4.** Classification and integration of 2D materials. Blue: stable in ambient conditions. Green: probably stable in ambient conditions. Pink: unstable in ambient conditions but stable in inert gas environment conditions. Gray: 3D compounds that can be formed monolayer 2D compounds by exfoliation. Reproduced with permission.<sup>[102]</sup> Copyright 2013, Springer Nature.

then transfer to the available substrate. Another significant problem is the interaction of the 2D materials with substrates and other factors present in their environment. Moreover, the structural and stoichiometric defects and doping are the difficulties in the calculation of 2D material properties, a remaining issue is lateral quantum confinement, where

electronic and optical properties depend on the lateral size of the 2D structures.<sup>[119,120]</sup>

2D materials have become the focus of research in various fields due to their various advantages. In the following research, it may be further developed in these aspects: First, the preparation of large areas of 2D materials will become the focus,

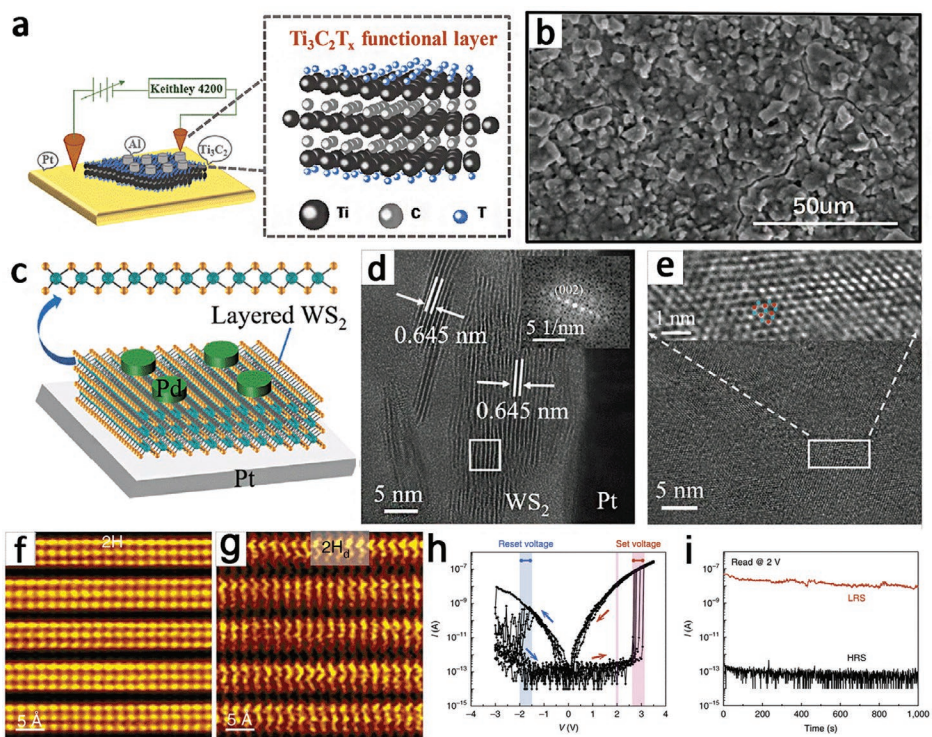


**Figure 5.** Micro analysis of several types of 2D materials that used to make the RS layer. a) Schematic structure of the Al/Ti<sub>3</sub>C<sub>2</sub>T<sub>x</sub>/Pt device and Ti<sub>3</sub>C<sub>2</sub>T<sub>x</sub> atomic structure. b) The scanning electron microscopy (SEM) of the Ti<sub>3</sub>C<sub>2</sub>T<sub>x</sub> film. Reproduced with permission.<sup>[115]</sup> Copyright 2019, Wiley-VCH. c) Schematic of the Pd/WS<sub>2</sub>/Pt device. d) Transmission electron microscope (TEM) and FFT (fast Fourier transfer) images of the WS<sub>2</sub> device. e) TEM image of a different area of the WS<sub>2</sub> device; the upper inset image shows an enlargement of the area outlined with a white rectangle in the main image and also the standard WS<sub>2</sub> unit cell (red and blue dots). Reproduced with permission.<sup>[116]</sup> Copyright 2019, Wiley-VCH. The high-angle annular dark field (HAADF) image of the MoTe<sub>2</sub> material shows f) the initial state and g) the low-resistance state, respectively. h) Cyclic I–V diagram of metal–Al<sub>2</sub>O<sub>3</sub>/MoTe<sub>2</sub>–metal device. i) Retention data of LRS and HRS of the same equipment as (h). Reproduced with permission.<sup>[118]</sup> Copyright 2019, Springer Nature.

so that it can be implemented in the industrial field. Second, increase the stability of monolayer 2D materials. For example, 2D black phosphorus has good application potential in various aspects, but its surface state is extremely unstable, especially monolayer 2D black phosphorus. In the future, improving the stability of such 2D materials is critical to their wide application. Third, 2D materials that can satisfy the high performance and low power consumption of devices will be at the heart of research. Finally, the high sensitivity and ultrathin retractable shape of 2D materials enable them to have further development in the direction of biosensing and flexible electronics.

### 2.3. Ferroelectric Material

The ferroelectric tunnel junctions (FTJs) composed of two metal electrodes separated by an ultrathin ferroelectric barrier. As a

promising candidate for nonvolatile memristor, it has recently received wide attention. Studies have demonstrated that the tunnel resistance effect in the ferroelectric tunnel junction triggers a change in the potential energy barrier associated with the iron polarization reversal.<sup>[121–123]</sup> Therefore, this bistable device system can switch between open LRS and HRS states with an external bias.

Over recent years, solid-state FTJs with various ferroelectrics such as BaTiO<sub>3</sub>,<sup>[125,126]</sup> PbZr<sub>0.2</sub>Ti<sub>0.8</sub>O<sub>3</sub>,<sup>[127]</sup> and BiFeO<sub>3</sub>,<sup>[128,129]</sup> have been demonstrated by several groups. At present, research of ferroelectric memristors mainly focuses on three aspects of changing electrodes, substrates and doping ferroelectric materials.

In 2013, Zheng et al. uses a heavily doped semiconductor instead of a metal bottom electrode, proposed a Pt/BaTiO<sub>3</sub>/Nb:SrTiO<sub>3</sub> structure (Figure 6a) with fast response time, long retention time (Figure 6c) and good switching reproducibility.<sup>[130]</sup> In 2018, Xiao et al. used mica as the substrate

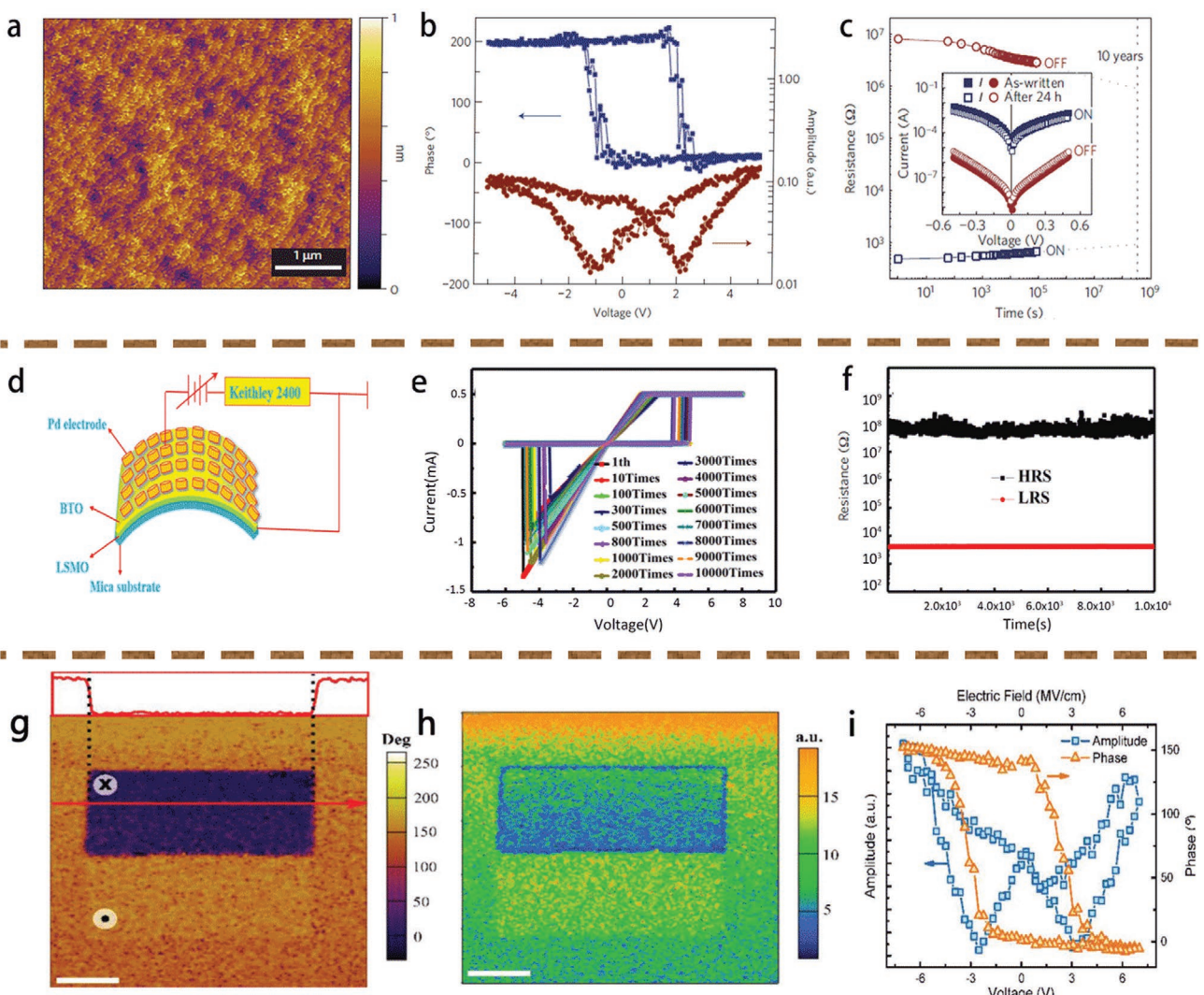


**Figure 6.** Electrical properties of ferroelectric materials. a) Surface morphology of Pt/BaTiO<sub>3</sub>/Nb:SrTiO<sub>3</sub> structure. b) Local piezoresponse force microscopy (PFM) hysteresis loops. c) Retention properties of Pt/BaTiO<sub>3</sub>/Nb:SrTiO<sub>3</sub> device. Reproduced with permission.<sup>[130]</sup> Copyright 2013, Springer Nature. d) Pd/BTO/LSMO/Mica structure and test schematic. e) Recorded I-V curves of bending times. f) Retention characteristics of the Pd/BTO/LSMO/Mica device after bending 10<sup>4</sup> times. Reproduced with permission.<sup>[131]</sup> Copyright 2018, AIP Publishing. g) PFM image of phase upon electrical poling, above is the cross section of the phase diagram along the red arrow. h) PFM image of amplitude upon electrical poling. i) Phase and amplitude change of single-point hysteresis loop. Reproduced with permission.<sup>[124]</sup> Copyright 2018, Wiley-VCH.

and  $\text{La}_{0.7}\text{Sr}_{0.3}\text{MnO}_3$  (LSMO), as the bottom electrode, and proposed a flexible memristor for high temperature applications, as shown as Figure 6d. The flexible memristor has potential for use in wearable and implantable electronic devices due to its high temperature stability, good flexibility and durability (Figure 6e,f), and simple device fabrication processes.<sup>[131]</sup> In the same year, Yoong et al. prepared a single-phase  $\text{Hf}_{0.5}\text{Zr}_{0.5}\text{O}_2$  (HZO) film, the PFM phase diagram and amplitude diagram are shown in the Figure 6g-i, and the brain-like computing capabilities of HZO thin film device are also demonstrated, prove that FTJs has great potential as a memory device and can be implemented as an artificial synapse in a neuromorphic structure.<sup>[124]</sup>

#### 2.4. Solid Electrolyte Materials

Memristors based on solid electrolytes are usually paired with active metal TE (such as Ag, Cu) and inert metal BE (such as Pt, Au, and W). In these devices, active metal TE can be oxidized and reduced directly by chemical redox reaction. The resulting metal ions can pass directly through the fast ion conductor matrix by drift and diffusion.<sup>[132-134]</sup> This will lead to faster switching and lower power consumption.

Hirose first reported the switching behavior caused by silver dendrite formation and quenching caused by redox reaction in 1976, using Ag-photodoped amorphous  $\text{As}_2\text{S}_3$  as the switching layer.<sup>[136]</sup> Terabe et al. developed the Pt/ $\text{Ag}_2\text{S}$ /Ag structure.<sup>[137]</sup> As shown in Figure 7a,b, in this case, a vacuum nanogap is used as the RS layer, and the metal foil grows in the gap to bridge the TE and BE. Since the switch is caused by an electrochemical reaction, increasing the switching bias can reduce the switching time shortened in multiples.<sup>[138]</sup> In addition, reducing the size of the device also produces a faster switch. In

2012, Jang et al. reported the RS characteristics of Au/ $\text{Ag}_2\text{S}$ /Ag structures (insets of Figure 7c) on flexible substrates. As shown in Figure 7c,d, all  $I$ -Vs have clear bipolar RS characteristics.<sup>[139]</sup> In 2005, Kaeriyama et al. proposed a  $\text{CuSO}_4$  solid electrolyte nanoswitch, called a nanobridge, as shown in Figure 7e, which is suitable for reconfigurable large scale integrated circuits due to its small size and low on-resistance. It also has a very low operating voltage (Figure 7f) and has the potential to be a low voltage nonvolatile memory.<sup>[140]</sup>

#### 2.5. Other Materials

In addition to the RS layer materials classified above, there are other less reported materials, including organic materials such as copper tetra-*t*-butylaminoquinodimethane ( $\text{Cu-TCNQ}$ ),<sup>[141]</sup> chitosan,<sup>[142]</sup> and the like. Magnetic tunnel junction, such as  $\text{MgO}$ .<sup>[143]</sup> Mott insulator, such as  $\text{GaTa}_x\text{Se}_y$ .<sup>[135]</sup> Owing to the use of unconventional process manufacturing technology, CMOS compatibility issues and the relatively unstable physical characteristics of the materials themselves, these materials are not common. In addition, heterojunction composed of photosensitive materials will be detailed in Section 4.2.3. For more material, see the review by Wang et al.<sup>[145]</sup>

### 3. Memristor Resistance Switching Mechanism

According to the key feature of  $I$ -V curves, RS devices are roughly divided into three types: bipolar, unipolar, and threshold as shown in Figure 8. Many mechanisms to explain RS are now proposed, including Schottky barrier,<sup>[146]</sup> Pool-Frenkel (P-F) emission,<sup>[147,148]</sup> space charge limited current (SCLC),<sup>[31,152]</sup> trap charging and discharging,<sup>[153-154]</sup> ferroelectric polarization,<sup>[121-124]</sup> electron spin,<sup>[143]</sup> and growth and fracture of conductive

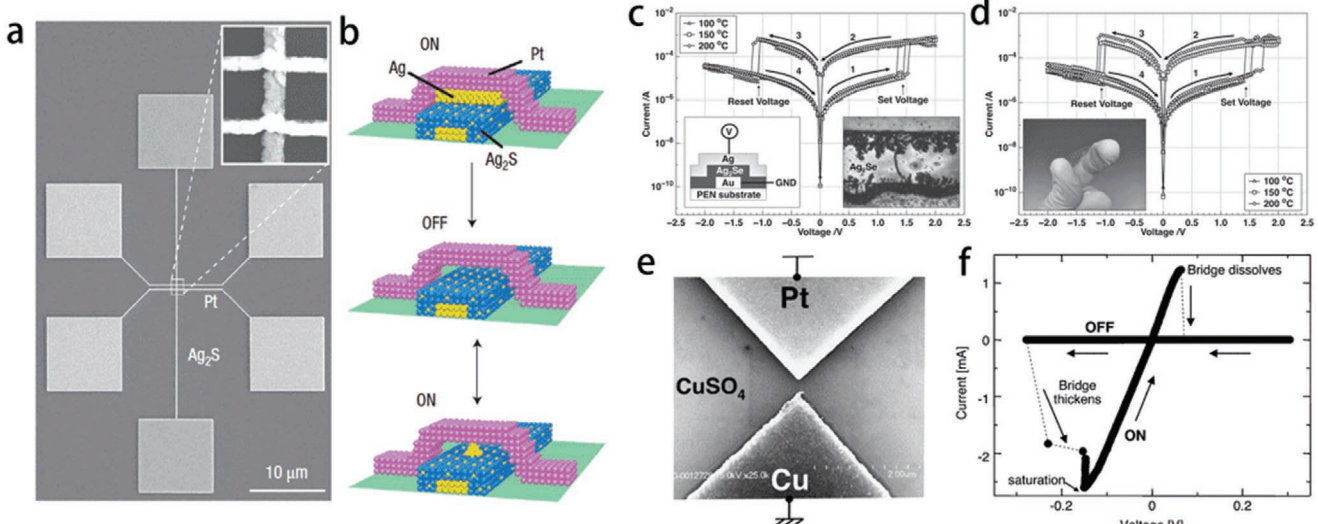


**Figure 7.** a) SEM of an atomic switch of Pt/ $\text{Ag}_2\text{S}$ /Ag device and b) its operating mechanism. Reproduced with permission.<sup>[137]</sup> Copyright 2005, Springer Nature. c) Representative  $I$ -V curves obtained from the Au/ $\text{Ag}_2\text{Se}$ /Ag devices. The illustration shows the structure diagram and micrograph. d)  $I$ -V curves after 100 repeated bending tests. Reproduced with permission.<sup>[138]</sup> Copyright 2006, IOP Publishing. e) SEM micrograph of Cu/ $\text{CuSO}_4$ /Pt structure. f)  $I$ -V characteristics of the e). Reproduced with permission.<sup>[140]</sup> Copyright 2006, Wiley-VCH.

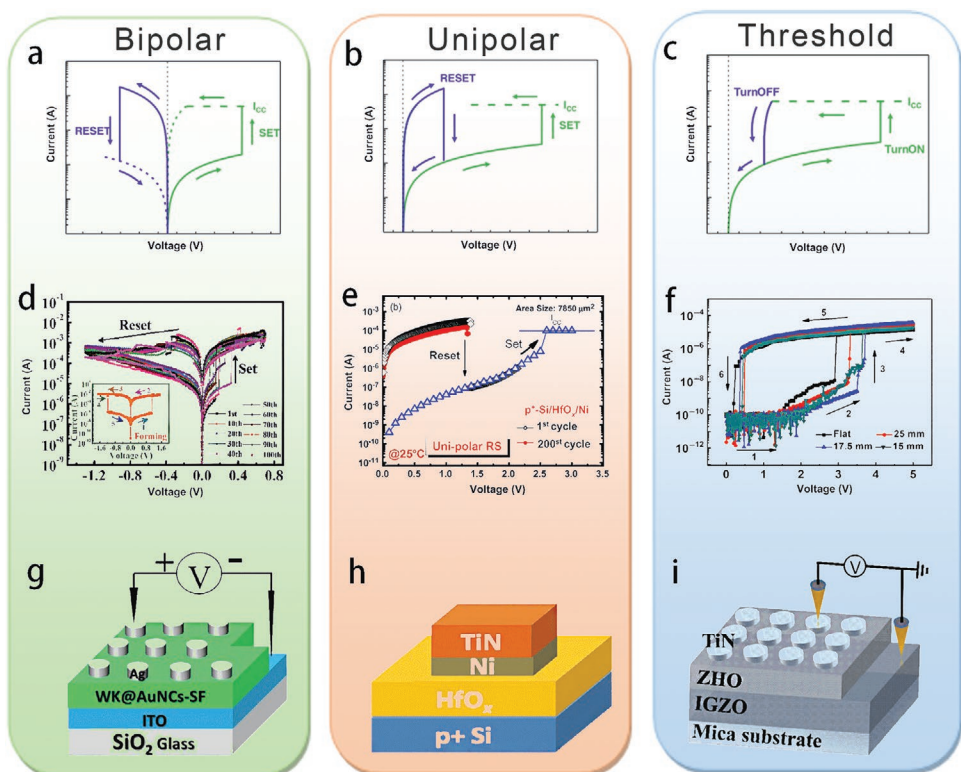


**Figure 8.** Characteristic I-V curve in: a) nonvolatile bipolar characteristic curve, b) nonvolatile unipolar characteristic curve and c) volatile threshold switching characteristic.  $I_{CC}$  is to limit the current to prevent device breakdown. d) I-V curve of structure (g). e) I-V curve of structure (h). f) I-V curve of structure (i). g) A bipolar device structure diagram. h) A unipolar device structure diagram. i) A threshold switch device structure diagram. d,g) Reproduced with permission.<sup>[158]</sup> Copyright 2017, Wiley-VCH. e,h) Reproduced with permission.<sup>[159]</sup> Copyright 2012, IEEE. f,i) Reproduced with permission.<sup>[160]</sup> Copyright 2018, Springer.

filaments,<sup>[156,157]</sup> etc. Among them, the conductive filament mechanism is the most widely studied mechanism, and is the focus of discussion in this section. For other mechanisms, see the review by Guo et al. and Wang et al.<sup>[144,155]</sup>

### 3.1. Conductive Filament or Channel

In the filamentary conduction mechanism, the RS process can be attributed to the growth and fracture of the conductive filament (CF) in the switching layer. According to the chemical composition of the filament, it is divided into two categories: metal-dominated filaments and nonmetal-dominated filaments. Conductive particles migrate and accumulate under the action of an electric field, gradually connecting TE to BE to form CF. Under the action of the reverse field, the conductive particles escape from the CF and the CF are broken, thereby forming a nonvolatile bipolar RS (Figure 8a). Figure 8g is a metal CF-based memristor structure, showing a typical bipolar RS (Figure 8d). In the metal-dominated filament mechanism, the conductive particles are generally TE metal ions. In the nonmetal dominant filament mechanism, defects such as oxygen vacancies act as conductive particles. However, for both CFs, the mechanism of unipolar RS (Figure 8b) is usually interpreted as a CF mode based on the Joule heating effect. The difference is that the RS behavior of unipolar mem-

ristor does not depend on the polarity of the applied voltage, while the RS behavior of bipolar memristors depends on the polarity of the applied voltage. This phenomenon is mostly observed in memristors based on NiO.<sup>[189–191]</sup> Figure 8h is a metal/nonmetal CF-based memristor structure, showing a typical unipolar RS (Figure 8e). In addition, if the CF breaks when the electric field strength drops to a certain degree, a unique threshold behavior occurs (Figure 8c). Figure 8i is a nonmetal CF-based memristor structure, showing a typical threshold RS (Figure 8f).

However, there is a strong random behavior during the growth and fracture of CF. CF does not always dissolve completely during the RESET process,<sup>[161]</sup> so CF devices usually have a forming process. After forming, the SET voltage will be less than the forming SET voltage. When the electrode spacing is large, CF will produce fine branches.<sup>[162]</sup> In this mechanism, CF directly determines the performance of the device. Uncontrolled CF growth lead to uncertainty, but when CF devices are integrated at high density, the growth space of CF is limited, and this problem can be solved by the size being small enough.

#### 3.1.1. Electrochemical Metallization Mechanism (ECM)

In ECM, the redox reactions of a metal electrode controls the RS. In terms of material selection, TE needs to select active

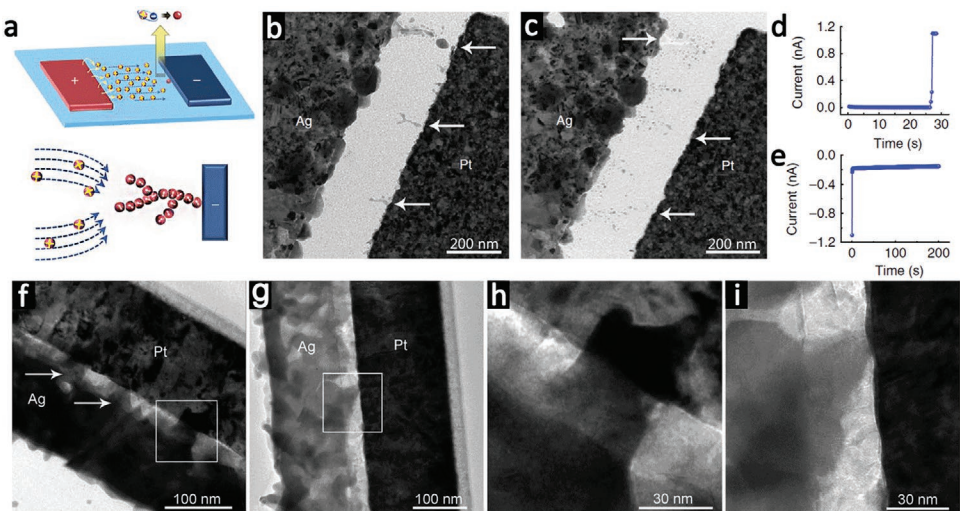


**Figure 9.** Observation of metal CF dynamics in memristors. a) Schematic diagram of dendritic CF growth in Ag/SiO<sub>2</sub>/Pt structure. b) TEM image of the Ag/SiO<sub>2</sub>/Pt device after the SET process. The arrows highlight several representative CFs. c) TEM image of the Ag/SiO<sub>2</sub>/Pt device after RESET process. d) Corresponding *I*-*t* curve during the forming process that led to the image in (b), and e) the corresponding *I*-*t* curve of CF annihilation process in (c). Reproduced with permission.<sup>[162]</sup> Copyright 2012, Springer Nature. f) A TEM image of the Ag/Mn:ZnO/Pt device. Multiple CF regions were observed, but there was only one CF region in (g). h,i) Enlarged images of the white frame areas in (f) and (g), respectively. Reproduced with permission.<sup>[169]</sup> Copyright 2009, American Chemical Society.

metals (generally Ag or Cu), and BE is an inert metal (such as Pt). Taking an Ag electrode as an example, when a sufficient positive bias is applied to TE, an oxidation reaction occurs at the TE/insulator interface, Ag atoms are oxidized to Ag<sup>+</sup> ions and electrons, and Ag ions migrate to BE in the RS layer under the action of an electric field. Then the Ag<sup>+</sup> and BE electrons meet, a reduction reaction occurs, and Ag atoms are formed. With the accumulation of Ag, Ag-CF grows and stretches in the RS layer (Figure 9a,b). When TE and BE are connected, the resistance drops sharply, causing a switch from HRS to LRS (Figure 9d). In contrast, when a negative bias is applied to TE, the Ag atoms in CF are dissolved into Ag<sup>+</sup> and electrons by oxidation reaction, CF cracking occurs (Figure 9c), and the current suddenly decreases (Figure 9e), causing a switch from LRS to HRS. From the perspective of growth kinetics, whether Ag-CF starts to grow from TE or BE depends on the position of Ag<sup>+</sup> and BE electrons when the reduction reaction occurs.<sup>[25]</sup> If Ag<sup>+</sup> has a higher mobility than electrons, Ag<sup>+</sup> and electrons meet in the vicinity of BE, and Ag-CF grows from BE to TE.<sup>[164]</sup> This behavior is usually observed in solid electrolytes that contains TE ions, such as the As<sub>x</sub>S<sub>y</sub> lattice provides a fast diffusion channel for Ag<sup>+</sup>,<sup>[163,171]</sup> makes Ag<sup>+</sup> have a higher mobility than electrons. Conversely, if Ag<sup>+</sup> has a lower mobility than electrons, Ag<sup>+</sup> and electrons meet in the vicinity of TE, and Ag-CF grows from TE to BE. This phenomenon is commonly observed when the RS layer is composed of a metal oxide such as SiO<sub>2</sub>,<sup>[165]</sup> HfO<sub>2</sub>,<sup>[166,167]</sup> ZrO<sub>2</sub>,<sup>[86,168]</sup> or ZnO.<sup>[169,170]</sup> As shown in Figure 9f-i, TEM observations confirmed the growth of CF from TE to BE in the ZnO layer.<sup>[169]</sup>

### 3.1.2. Valence Change Mechanism (VCM)

Similar to ECM devices, RS still relies on the growth of CF. However, unlike ECM, there is no electrochemical reaction

happened in VCM devices. TE and BE electrodes usually use inert electrodes or oxides. For example, Pt, TiN, Au, and Ta or indium tin oxide (ITO) and indium gallium zinc oxide (IGZO). The RS layer usually uses metal oxides, such as ZnO, HfO<sub>2</sub>, and Ta<sub>2</sub>O<sub>5</sub> and so on. Figure 10a is a model of a typical VCM device. The switching mechanism in VCM is related to the migration, accumulation, and rearrangement of oxygen vacancies ( $V_{Os}$ ), which leads to the formation of metal oxides with different compositions and new phases.<sup>[176]</sup>

For the Ta<sub>2</sub>O<sub>5</sub> RS layer as an example, the film is in an initial HRS, when a bias voltage is applied, O<sup>2-</sup> escapes from the initial position under the action of an electric field,  $V_{Os}$  are generated, and then accumulate at the BE/oxide interface,<sup>[173,179]</sup> causing the contrast of the oxide layer to be different, as shown in Figure 10g-k. Depending on the bias voltage applied, the Ta<sub>2</sub>O<sub>5</sub> layer acts not only as an oxygen supplier, but also as an oxygen reservoir.<sup>[180,181]</sup> The dark areas near TE and BE both increase with increasing voltage.<sup>[173]</sup> Finally, the two dark areas are connected to form CF, as shown in Figure 10l. While in the ZnO thin film device, the CF growth process is more obvious as shown in Figure 10b-f.

In this case, the redistribution of oxygen vacancies will adjust the stoichiometry of the oxide-based switching layer, and thus the conductivity of the film. Similar to ECM devices, this phase transition caused by ion migration is reversible, reverse bias can promote the combination of O<sup>2-</sup> and  $V_{Os}$  at the TE/oxide interface, leading to CF annihilation. In this case, since the metal electrode hardly participates in ion migration and no impurity residue is introduced into the oxide layer, a longer write/erase endurance cycle is usually obtained in a VCM device.<sup>[177,178]</sup>

### 3.1.3. Phase-Change Mechanism

As a memory material with superior performance that has been mass-produced, phase-change materials have shined

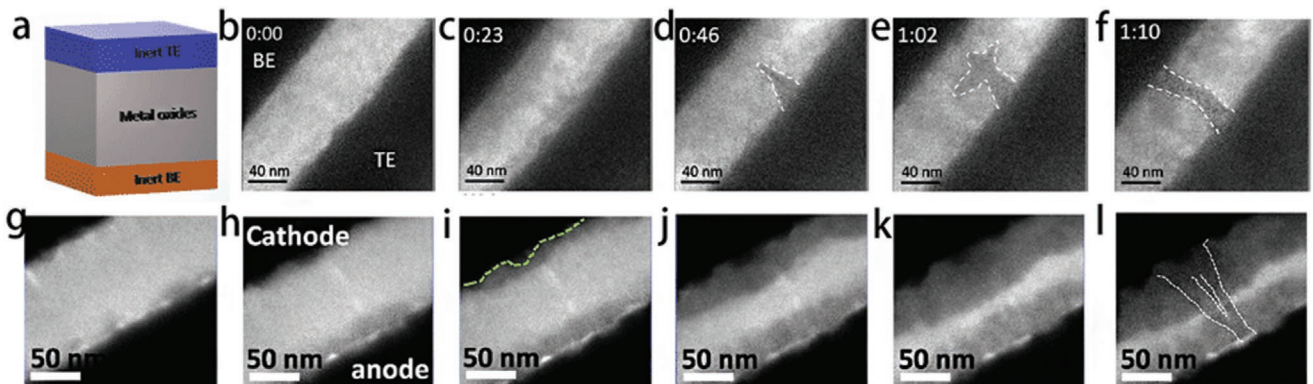


**Figure 10.** The forming process of the CF in situ TEM images with a schematic diagram. a) VCM device structure diagram. b–f) In situ TEM image of filament growth in ZnO thin film device. Reproduced with permission.<sup>[173]</sup> Copyright 2013, American Chemical Society. g–l) In situ TEM image of filament growth in Ta<sub>2</sub>O<sub>5</sub> thin film device. Reproduced with permission.<sup>[182]</sup> Copyright 2015, Wiley-VCH.

in the RS field in recent years. As shown in **Figure 11a**, by applying appropriate electrical pulses, phase-change materials (PCM) shows fast switching behavior between amorphous and crystalline phases. Corresponding to the switching between HRS and LRS. Through the observation of thermal imaging, it was confirmed that the phase-change behavior was caused by thermal change (Figure 11b). Due to the different bonding modes, the amorphous and crystalline phases show quite different structures in terms of structural periodicity and long-range order, which results in unusual electrical and optical properties.<sup>[183]</sup> When an electrical pulse is applied to the PCM, as the number of pulses increases, the volume of the mushroom-shaped amorphous region becomes smaller, and when the crystalline region communicates with the BE, the device is set to LRS. Figure 11c shows a TEM cross-sectional view of

a Ge<sub>2</sub>Sb<sub>2</sub>Te<sub>5</sub> (GST) PCM. The transition from the set state to the reset state, the volume of the amorphous region at the top of the bottom electrode increases, and the LRS state is reached when the bottom electrode is completely covered. The inset shows the diffraction pattern of the amorphous region, indicating that the GST is polycrystalline. PCM have been served in practical applications due to their impressive on/off current ratios, long hold times, and fairly high stability. In addition, large array PCM can be easily integrated in smaller device sizes with high data density, which indicates that it is suitable for modeling biological synapses and neural networks,<sup>[184]</sup> but the durability of PCM in a high temperature environment above 85 °C is a problem, and the thermal interference of the PCM crossbar array makes this problem even more prominent.

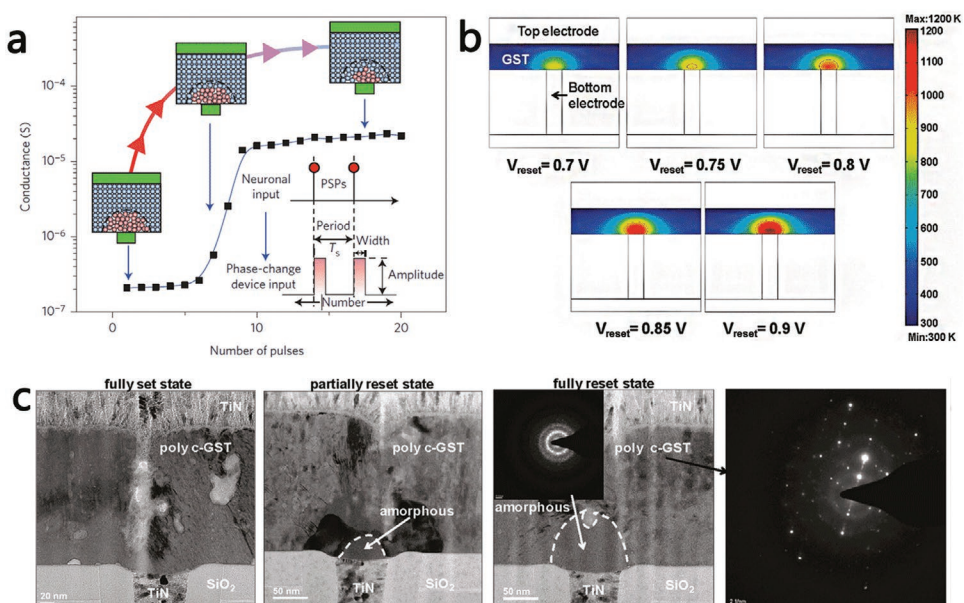


**Figure 11.** a) The phase-change device conductance changes with the crystal number of the pulse sequence. Reproduced with permission.<sup>[185]</sup> Copyright 2016, Springer Nature. b) Temperature of the GST region at different reset voltages are shown. c) Cross-section TEM images of electronic synapses made of GST are shown. Reproduced with permission.<sup>[186]</sup> Copyright 2012, American Chemical Society.

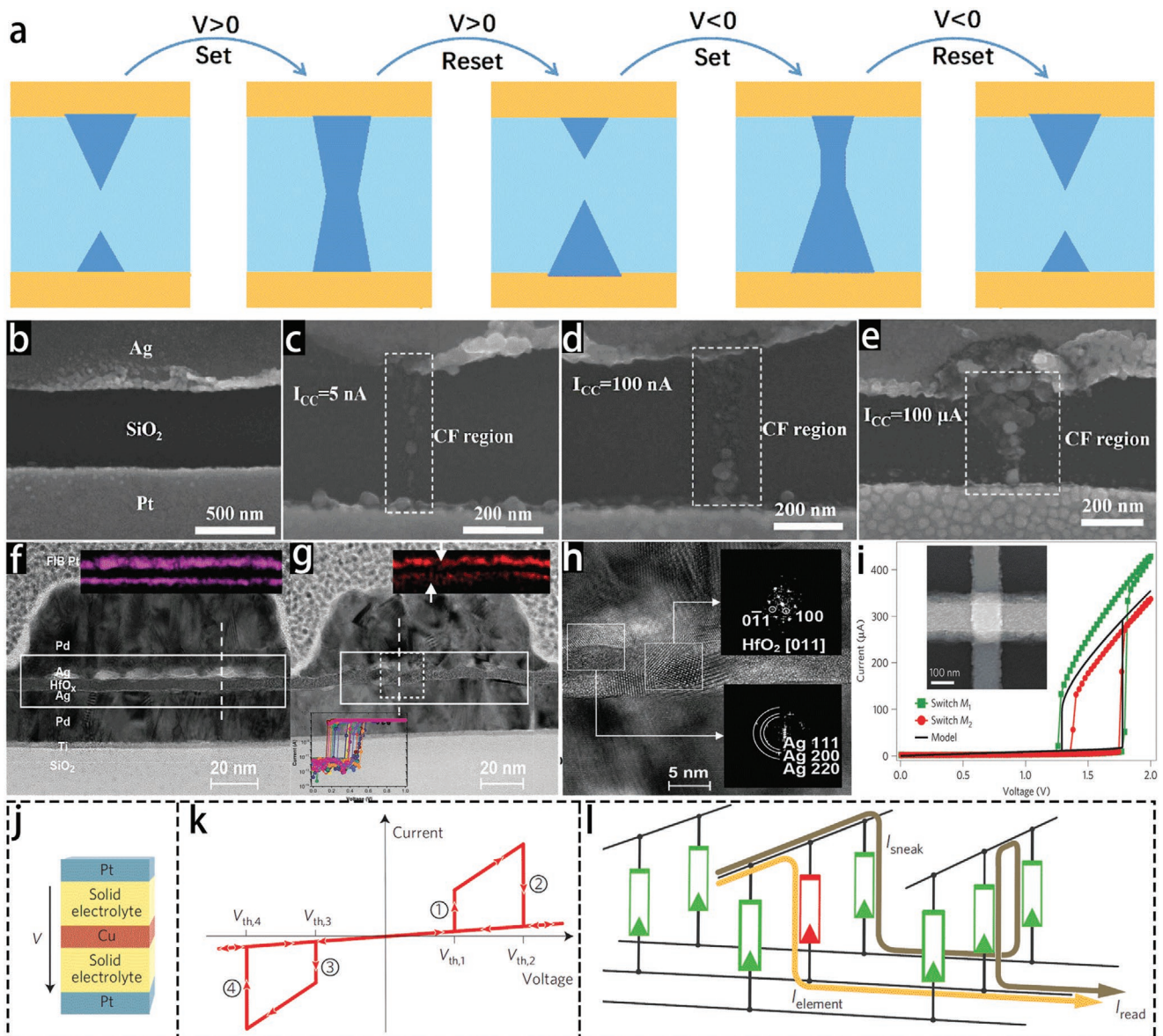


**Figure 12.** Microanalysis of threshold mechanism. a) Schematic diagram of single device threshold switching. b) SEM imaging of a Pt/SiO<sub>2</sub>/Ag planar junction, after electroforming under c) 5 nA, d) 100 nA, and e) 100 μA compliance current. Reproduced with permission.<sup>[188]</sup> Copyright 2014, Wiley-VCH. f) TEM cross-sectional image of a pristine Pd/Ag/HfO<sub>2</sub>/Ag/Pd device. g) TEM cross-sectional image of the measured device. The upper inset shows an EDS map of Ag with I-V shown in the lower inset. h) HRTEM of the dashed white box region in (g) which shows a narrowed Ag gap. Reproduced with permission.<sup>[192]</sup> Copyright 2017, Wiley-VCH. i) Typical I-V curve of NbO<sub>2</sub>-based Mott memristor. The inset is a SEM image of the Pt/NbO<sub>2</sub>/Pt device. Reproduced with permission.<sup>[322]</sup> Copyright 2013, Springer Nature. j) Schematic diagram of the complementary RS structure. k) I-V characteristic of a complementary RS. l) Crossbar array and sneak path issue. Reproduced with permission.<sup>[193]</sup> Copyright 2010, Springer Nature.

### 3.1.4. Threshold Switching Mechanism

The above-mentioned several CF mechanisms are nonvolatile. The threshold switching (TS) is a volatile RS mechanism with unique dynamic characteristics, has greater potential in the field of neuromorphic computing as synapse that will be introduced in next section. When the bias voltage is lower than a certain value, the resistance is switched from LRS to HRS (Figure 8c). Ovshinsky first reported TS in thin-film devices in the 1960s.<sup>[187]</sup> The TS mechanism can be explained as follows (Figure 12a). In 2014, Sun et al. reported observations of

a filament with a planar threshold switch on planar Pt/SiO<sub>2</sub>/Ag cells. As shown in Figure 12c,d, volatile RS was observed at both 5 and 100 nA  $I_{CC}$ . When the  $I_{CC}$  reaches 100 μA, the nanosilver particles are connected as a conductive bridge (Figure 12e), raised a conversion from TS to bipolar switching.<sup>[188]</sup> In 2017, Midya et al. conducted a cross-sectional high-resolution transmission electron microscopy (HRTEM) analysis of nanoscale Pd/Ag/HfO<sub>x</sub>/Ag/Pd vertical connections. Figure 12f,g shows two cross sections of the as-deposition device and the electrically operated device, showing repeatable volatility switching. The FFT corresponding to the left white

box in Figure 12h shows the presence of nanocrystalline Ag.<sup>[192]</sup> The TS device can be used to design and manufacture high-performance selectors due to its special nonlinearity.

In 2010, Linn et al. designed a complementary RS device. As shown as Figure 12j, a typical complementary RS device consists of two anti-serial-connected bipolar memristor cells. In different voltage offset regions, the complementary RS effect is accompanied by a switch polarity inversion (Figure 12k).<sup>[193]</sup> Because all complementary RS always exhibit the same high resistance independent of the stored binary information. It is considered to be an effective method to solve the sneak path problem (Figure 12l) in large-scale integrated passive memristor crossbar, making the application of large passive crossbar structures possible. In 2013, Pickeet et al. used a Mott memristor to achieve a volatile RS (Figure 12i) through a phase transition between metal and insulator, and proved its ability to be used for neuromorphic computing. Wang et al. discuss the TS mechanism in detail, see ref. [194].

## 4. Biological Synaptic Behavior and its Plasticity Simulation

### 4.1. Biological Synapse

Since the first discovery of neuronal cells in humans in 1872, it has been nearly 150 years since today, although there is a clear understanding of bioelectrical phenomena at the level of a single neuron cell, little is known about the specific working methods of biological neural networks. With the development of science and technology, even for the simplest insects (such as an ant or a cockroach), people still do not understand the specific operation of their nervous system.

Bioelectrical phenomena of cells: There are two main manifestations of bioelectrical phenomena at the cellular level, one is the resting potential at rest, and the other is the action potential generated when stimulated. Synapses are elemental to information propagation in the central nervous system, as shown in Figure 13a. Intersynaptic signal transmission is completed by neurotransmitters. At the front of the synapse, when the

action potential comes,  $\text{Ca}^{2+}$  is allowed to enter the presynaptic neuron, which promotes the fusion of synaptic vesicles with the plasma membrane, thereby releasing the neurotransmitter, as shown in Figure 13b. Then the neurotransmitter binds to the postsynaptic cell membrane receptor, changes the postsynaptic potential, and completes the transfer of action potential.<sup>[196,197]</sup>

### 4.2. Artificial Synapse

Artificial synapses are designed to mimic the structure and memory function of biological memory systems.<sup>[198–203]</sup> The basic and decisive factor for the brain's ability to achieve memory and learning is synaptic plasticity.<sup>[204–206]</sup> Therefore, the preparation of artificial synapses and subsequent major activities depend on the simulation of synaptic plasticity, such as long-term enhancement (LTP), long-term depression (LTD), short-term enhancement (STP), short-term depression (STD), and spike-time dependent plasticity (STDP), paired pulse suppression (PPD), and paired pulse promotion (PPF).<sup>[207,208]</sup> In psychology there are two types of memory behaviors, i.e., short- and long-term memory (STM and LTM), both of which are considered to result from the synaptic plasticity. Specifically, the significance of PPF is: In biological synapses, the second action potential spike caused by PSC is higher than the preceding one, and the degree of enhancement is related to the pulse interval. As a result shown in Figure 14b, artificial synapses are enhanced under higher frequency (5000 Hz) pulse stimulation.

Among them, STDP describes the strength of the connections between neurons, perfecting the traditional Hebb synaptic plasticity model proposed in 1949.<sup>[209]</sup> This combination of knowledge results in the proposal of potential artificial architectures for STDP learning systems.<sup>[210–216]</sup> STDP was originally postulated as a family of computer learning algorithms,<sup>[217,218]</sup> and is being used by the machine intelligence and computational neuroscience community.<sup>[219,220]</sup> At the same time its biological and physiological foundations have been reasonably well established during the past decade.<sup>[221,222]</sup> In this section, we present the neuromorphic calculations of memristors based on different mechanisms.

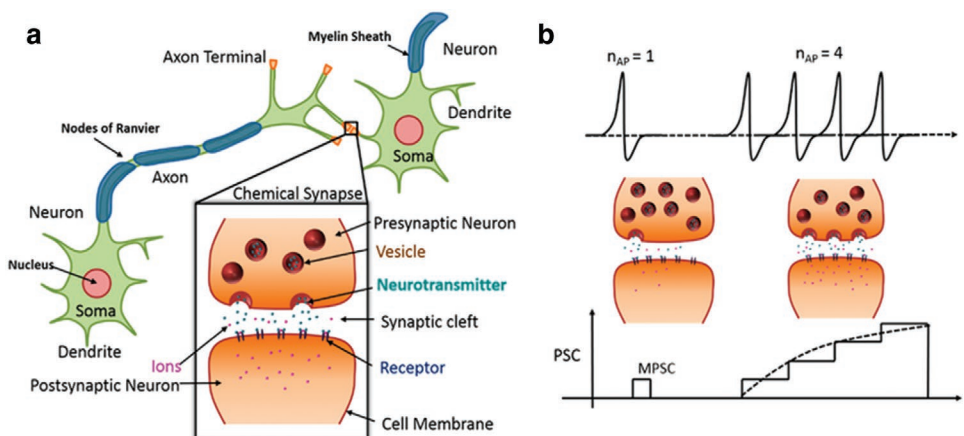


**Figure 13.** Description of a biological synapse. a) The action potential transmission path and the enlarged view of the synapse. b) The postsynaptic current (PSC) increases with the number of the presynaptic potential. Reproduced with permission.<sup>[195]</sup> Copyright 2017, American Chemical Society.

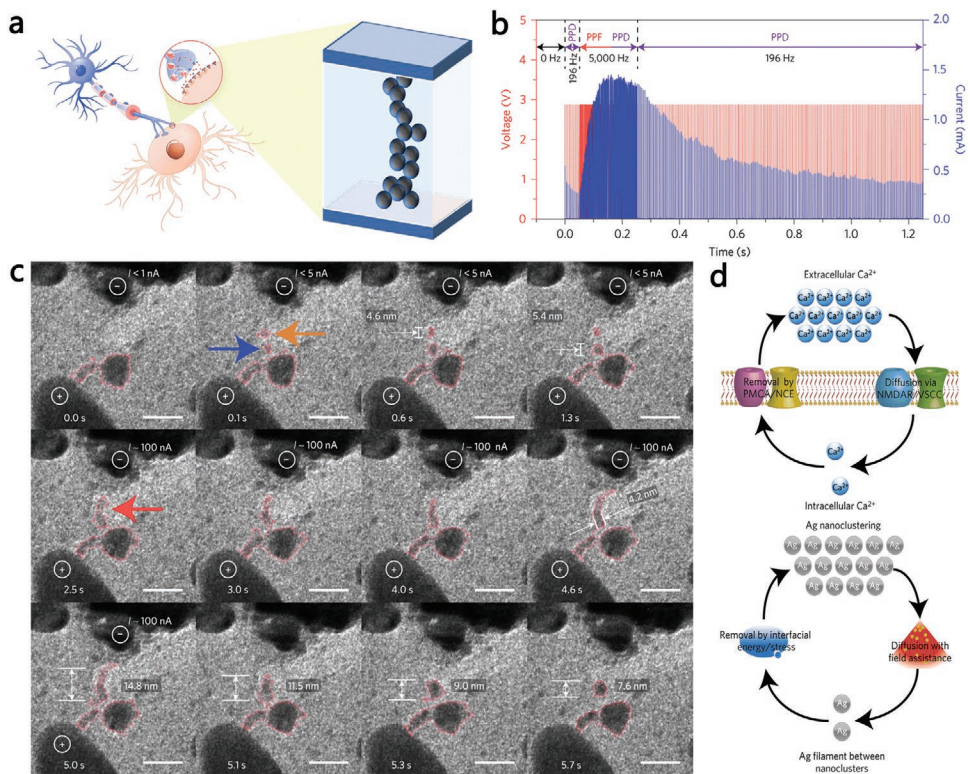


**Figure 14.** The simulation of synaptic weight with CF. a) The biological synapse can be represented by a RS device. b) The simulation of synaptic PPF and PPD behavior, as well as PPD following PPF behavior by the Ag-in-oxide memristors. c) The growth and fracture process of Ag CF under in situ TEM. d) Schematic illustration of the analogy between  $\text{Ca}^{2+}$  and Ag dynamics. Reproduced with permission.<sup>[225]</sup> Copyright 2017, Springer Nature.

#### 4.2.1. Neurophysiological Simulation of CF

CF's growth and fracture behavior of memristors are very similar to changes in synaptic weight in biological synapses. Therefore, CF-based memristors are candidates for artificial synapses.<sup>[223]</sup> The simulation of changes in presynaptic and postsynaptic potentials by a memristor based on the CF mechanism is shown in Figure 14a. So far, many CF-based memristors have been used as artificial synapses, simulate key synaptic learning rules. For the nonvolatile RS mechanisms ECM and VCM, due to the lack of  $\text{Ca}^{2+}$  diffusion kinetics, modulation pulses are generally used to achieve STDP, it shows that synaptic weight can be adjusted and controlled by adjusting the time interval between presynaptic and postsynaptic spikes.

In 2017, Yang and colleagues demonstrated Ag nanoclusters in oxide-based volatile memristors (Figure 14c), in which the diffusion kinetics of Ag atoms are similar to  $\text{Ca}^{2+}$  migration in biological synapses. The simulation of  $\text{Ca}^{2+}$ -like kinetics in memristors should be for the pursuit of more complex artificial synapses, as  $\text{Ca}^{2+}$  kinetics including  $\text{Ca}^{2+}$  accumulation and extrusion are key steps in achieving postsynaptic potential changes. With the help of an electric field, Ag diffuses into the interstitial region between the Ag nanoclusters, similar to the inflow process of  $\text{Ca}^{2+}$ . When electrical stimulation is removed, the interface energy and possible mechanical stress bridge the Ag nanoparticles from the interstitial region, thereby replicating the  $\text{Ca}^{2+}$

extrusion process. Therefore, the Ag dynamics of the diffusion memristor is a functional simulation of the biological synapse (Figure 14d).<sup>[225]</sup> In addition, it has also been shown in biological synapses that prolonged or excessive high-frequency pulse stimulation eventually leads to a transition from promotion to inhibition, which is only caused by an increase in the number of stimulation pulses of the same frequency.<sup>[226]</sup> Experimentally verified, the behavior of PPD and PPF is shown in Figure 14b, similar to the STP of synapses, implying potential for autonomic computing.<sup>[227,228]</sup>

#### 4.2.2. Neurophysiological Simulation of PCM

Sulfide PCM is one of the foremost main candidate for neurally inspired computing technologies, and they are technically mature. Figure 15a shows the biological synapse and the basic concept of emulating it with PCM.<sup>[186]</sup> Similar to CF, through the growth of the crystal phase (Figure 15b), a continuous transition between the resistance levels of phase-change materials is used here to simulate biological synapses in a simulated manner and to achieve synaptic plasticity. Successfully commercialized phase-change material technology has shown great potential in simulating the functionality and plasticity of biological synapses. The artificial synapse shown here is a good simulation of a biological synapse, which implements STDP and cumulative weight change depends on

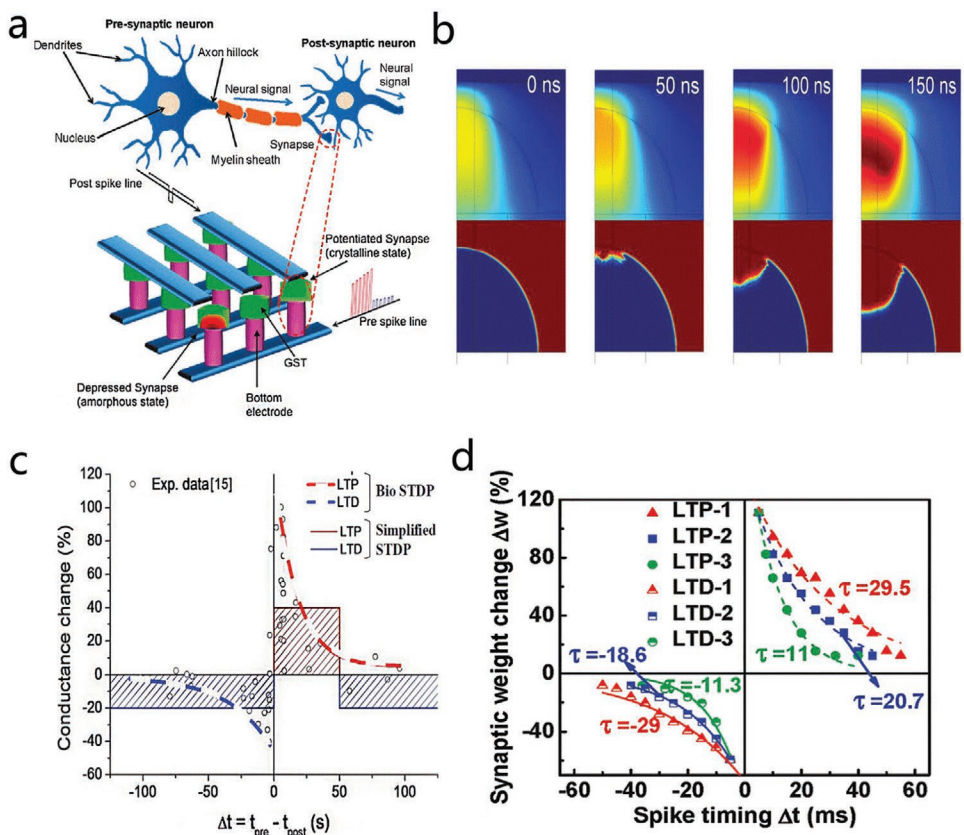


**Figure 15.** Artificial synapse based on a phase-change device. a) In the crossbar array architecture, PCM synapses correspond to biological synapses. b) As the temperature rises, the crystalline phase grows for increasing time (synaptic weight change). Reproduced with permission.<sup>[229]</sup> Copyright 2013, Wiley-VCH. c) Biological STDP and simplified STDP of phase-change synapse. Reproduced with permission.<sup>[230]</sup> Copyright 2011, IEEE. d) For different prepulse amplitudes at intervals, spike timing delay in the range of 10–30 ms for potentiation and –10 to –30 ms for depression. a,d) Reproduced with permission.<sup>[186]</sup> Copyright 2012, American Chemical Society.

the number of pulse pairs, with a maximum weight change of 100% (Figure 15c,d).<sup>[231]</sup> In 2011, Manan et al. used the PCM as an energy-saving synapse, demonstrating a SNN with ≈4 million synapses, enabling complex visual mode extraction with high detection rates and low system learning power consumption.<sup>[230]</sup>

#### 4.2.3. Optoelectronic Resistive Random Access Memory (ORRAM)

In recent years, ORRAM-based artificial photoelectric synapses has become a hot topic and has been studied by many teams, which have huge potential in simulating biological vision systems, and can even go beyond the visible light region. Although this technology is yet to mature, it will reduce the complexity and power consumption of integrated circuits and help the development of neural networks in machine vision.

In 2017, Tan et al. found that the band curvature of the region and the intrinsic conductive structure of ITO/CeO<sub>2-x</sub>/AlO<sub>y</sub>/Al can be significantly modulated when subjected to light irradiation pulses and electrical stimulation pulses in the ITO/CeO<sub>2-x</sub>/AlO<sub>y</sub>/Al heterojunction (Figure 16a,b), resulting in a durable and adjustable photoresponse in the device. All of the resistance states along with the original

state can be optically programmed, maintained, electrically read and erased in a cyclic operation (Figure 16c). Therefore, the device can convert the wavelength (or frequency) information of the incident beam into an electrical signal and store them at the same time.<sup>[232]</sup> In 2019, Wang et al. reported the optical modulation characteristics of MoS<sub>2</sub>/perylene-3,4,9,10-tetracarboxylicdianhydride (PTCDA) hybrid heterojunction ORRAM (Figure 16d) with both electrical and optical modulation, efficient gate tunability and significant STP and LTP. The PPF behavior of under light stimulation with a pulse width of 400 ms and an interval of 100 ms is shown in Figure 16e.<sup>[234]</sup>

Interestingly, almost all heterojunctions ORRAM exhibit synaptic behavior. Gao et al. used pulsed light stimuli applied to the ITO/Nb:SrTiO<sub>3</sub> heterojunction, and the obtained light response results show typical neurobehavior.<sup>[243]</sup> As shown in Figure 17a, the PPF measurement result is shown for a pair of light pulses with  $\Delta t = 0.5$  s. The PPF curve in Figure 17b also shows quite good performance, the PPF is still above 115% with  $\Delta t = 20$  s. At the same time, the “repetitive learning” phenomenon of the device similar to the human brain has also been confirmed. As shown in Figure 17c, the artificial photoelectric synapse reaches a high learning level (high synaptic weight) after continuous application of 100 light pulses, and after 100 seconds

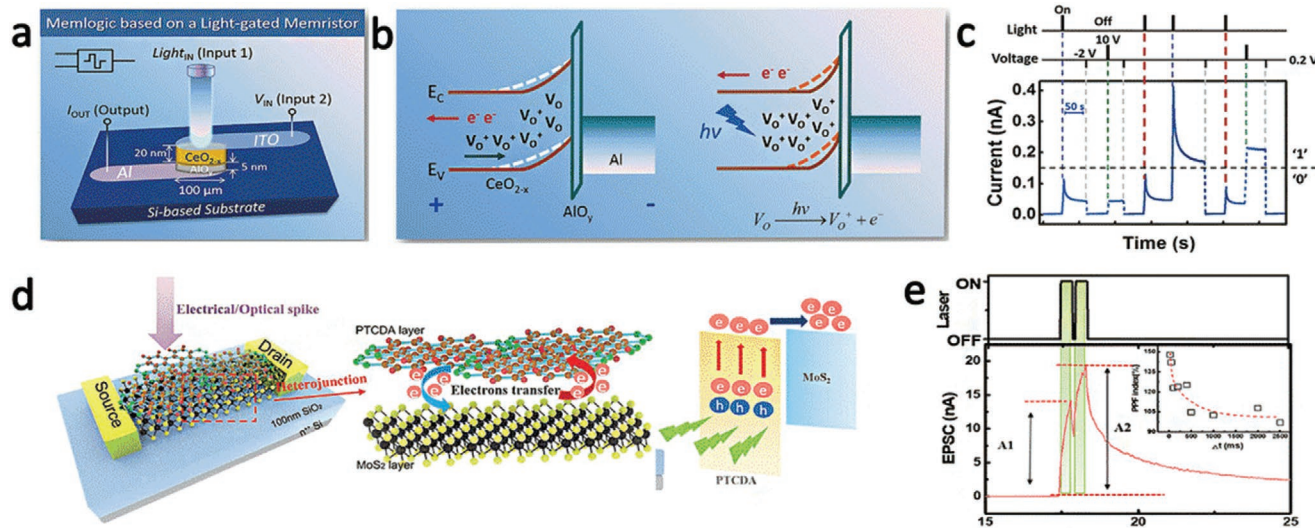


**Figure 16.** Schematic diagram of light regulation of heterojunction ORRAM. a) Schematic diagram of light regulation of ITO/CeO<sub>2-x</sub>/AlO<sub>y</sub>/Al structure. b) Effect of illumination on the ITO/CeO<sub>2-x</sub>/AlO<sub>y</sub>/Al heterojunction Schottky barrier. c) Photoresponse and electrical erasability of the ITO/CeO<sub>2-x</sub>/AlO<sub>y</sub>/Al heterojunction at a read voltage of 0.2V. Reproduced with permission.<sup>[233]</sup> Copyright 2017, American Chemical Society. d) 3d schematic of the MoS<sub>2</sub>/PTCDA structure, and charge transfer under light pulses. e) PPF behavior by MoS<sub>2</sub>/PTCDA heterojunction under dual light pulse stimulation (V<sub>ds</sub> is 0.1V, green area represents laser pulses irradiation). Reproduced with permission.<sup>[234]</sup> Copyright 2019, Wiley-VCH.

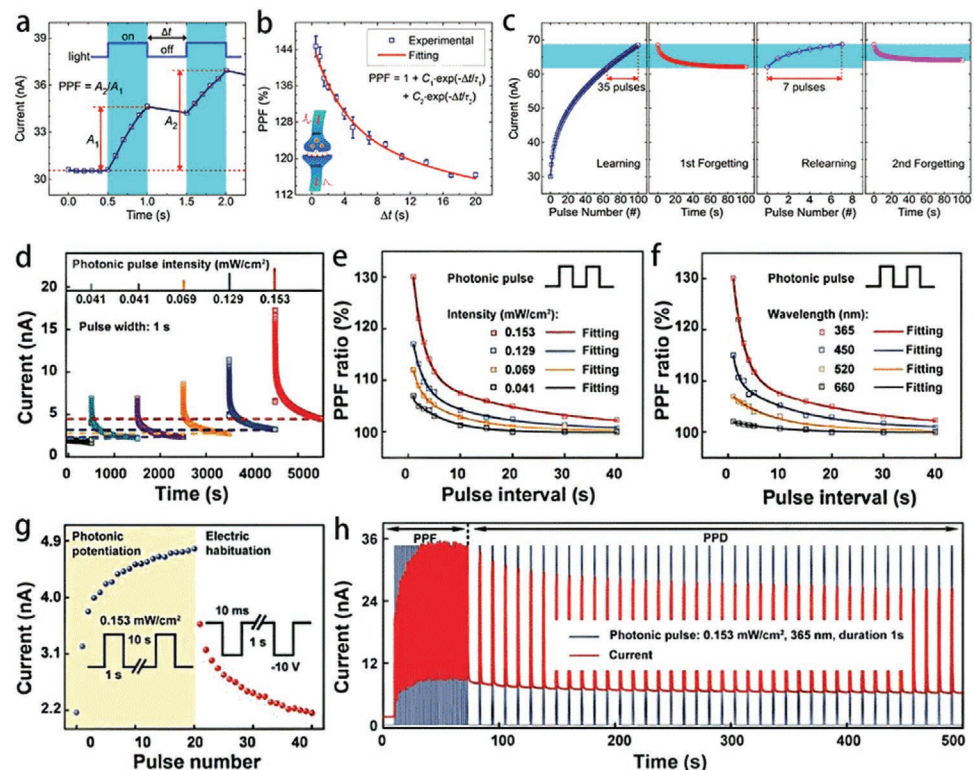


**Figure 17.** Photoresponsive characteristics of the heterojunction artificial optoelectronic synapse under pulsed light stimuli. a) A blue light pulse ( $\Delta t = 0.5$  s) acting on the ITO/Nb: SrTiO<sub>3</sub> heterojunction with a light intensity of 30 mW cm<sup>-2</sup>. b) The PPF is represented by the interval between two light pulses. c) The phenomenon of biological synaptic repetition learning. Reproduced with permission.<sup>[243]</sup> Copyright 2019, American Chemical Society. d) For a single pulse of fixed wavelength and different light intensities, the excitatory postsynaptic current generated by CsPbBr<sub>3</sub> perovskite quantum dots (QDs)-based artificial photon synapses. The PPF effect is simulated with two e) fixed wavelengths, different light intensities, and f) fixed light intensities and different wavelengths of light pulses. g) Response of synaptic devices to light pulse sequences and negative electrical pulse sequences. h) Experimental demonstration of PPD following PPF in the device. Red line: device current, blue line: photonic pulse. Reproduced with permission.<sup>[244]</sup> Copyright 2018, Wiley-VCH.

of darkness (forgetting process), then reapplying the light pulse (relearning), it can be found that only 7 light pulses are required to reach the first time learning's high synaptic weight level, which is far less than the 35 pulses that in the first time. In addition, in the next 100s of forgetting In synapses, synaptic weights of were reduced less than the first time forgetting, which is a good simulation of the process of human brain learning-forgetting-learning-forgetting. This behavior can be described as follows: it takes less time for a person to relearn before losing knowledge, and the memory is more profound after relearning.<sup>[242]</sup>

In 2018, Wang et al. reported artificial optoelectronic synapses based on inorganic perovskite quantum dots. In Figure 17d, during the cumulative modulation of photon pulses, volatile memory is converted to nonvolatile memory, thereby stimulating memory to maintain LTM from STM to brain plasticity. Figure 17e,f summarizes the PPF effect simulated by two identical light pulses, which show that the average PPF increases gradually at different intensities and wavelengths, positively correlated with light intensity and wavelength. Figure 17g shows the reliable enhancement-suppression function under different stimuli, simulating the memory impression of the brain. Figure 17h illustrates the application of photon pulses at different time intervals, tuning the synaptic function from PPF to PPD, which mimics the facilitation-depression transition in the biological neural network.<sup>[244]</sup> As such, the heterojunction can be reasonably regarded as an artificial optoelectronic synapse.<sup>[238–241]</sup>

## 5. Memristor Neural Network (MNN)

In a neural network formed by a large crossbar array constructed by memristors, memristors can directly use physical laws to perform efficient large-scale memory calculations by applying learning algorithms. Although the energy efficiency and computation speed of the recently implemented MNNs are satisfactory, experimental implementation of large-scale memristor crossbar arrays is still in its infancy.

### 5.1. ANN

ANN is a machine learning technology that realizes artificial intelligence by simulating biological neural networks, which was born to understand and replicate human capabilities. The neural network in the human brain is a very complex organiza-

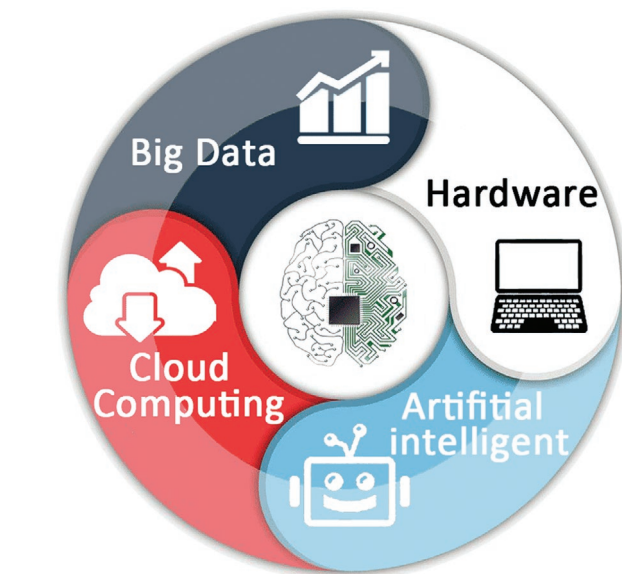


Figure 18. Neural network application field.

tion. There are estimated 100 billion neurons in the adult brain, and each neuron has about 10 000 weights.<sup>[250]</sup> Figure 18 shows several areas in which the neural network may be applied in the future. Businesses are increasingly adopting artificial intelligent (AI) to create new applications, driving the development of AI-optimized chips. These applications include connected devices, autonomous vehicles, on-device personal interfaces, voice interactions and augmented reality (AR).

Recently, artificial neurons based on memristors have been developed, but with limited bio-realistic dynamics and no direct interaction with the artificial synapses in an integrated network.<sup>[251]</sup> And most current research is limited to small size (<1024 memristors), binary device states, or limited reconfigurability. Of course, scientists have developed a large neural network (165 000 synapses) implemented with a PCM array,<sup>[314]</sup> but this work was limited by a sequential interface.<sup>[253]</sup>

ANN is an operation model composed of a large number of interconnected neurons.<sup>[252]</sup> Figure 19a is a simple ANNs flow diagram. Each neuron (circle) represents a specific output function, called a stimulus function. The connection between each two neurons represents the weight value of the signal passing through the connection, called the weight, which is equivalent

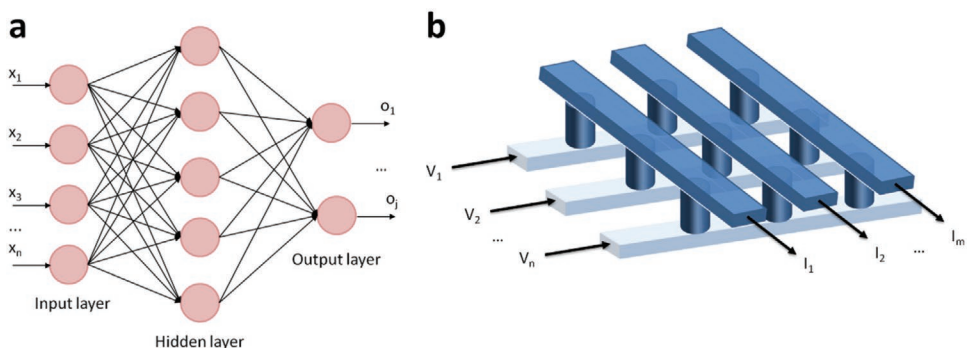
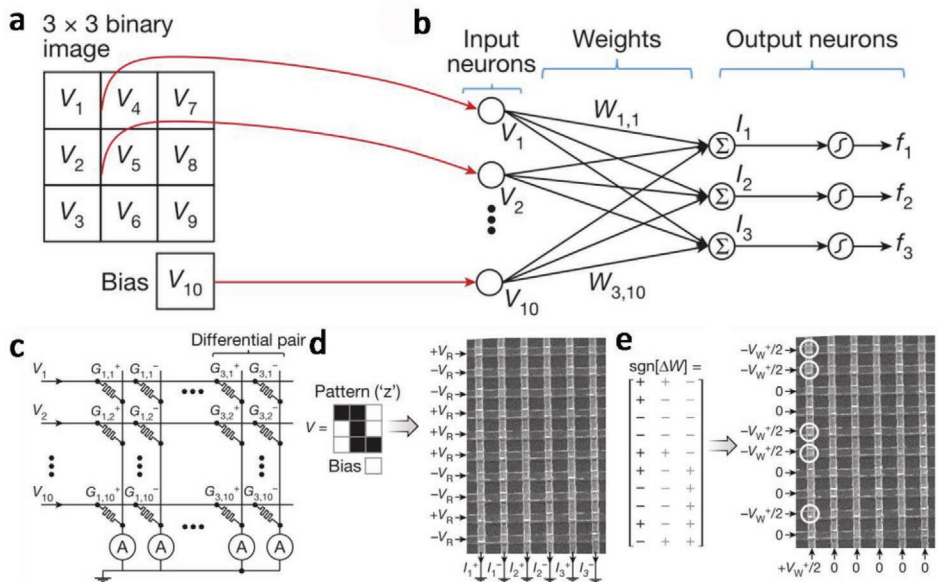


Figure 19. a) A simple neural network topology diagram. b) Schematic of a memristor crossbar.



**Figure 20.** The principle of a simple pattern classification. a) Input image. b) The single-layer perceptron for classification of  $3 \times 3$  binary images. c) Single-layer perceptron realized with a  $10 \times 6$  memristor crossbar. d) Example of classification training for a specific pattern "z." e) Example of weight adjustment for a specific column (first column in this figure). Reproduced with permission.<sup>[328]</sup> Copyright 2015, Springer Nature.

to ANN memory. The output of the network varies with the way that the network is connected, the weight value and the incentive function. In addition, the hardware implementation of the MNNs depends on the memristor crossbar (Figure 19b), which can be achieved by matching with peripheral neuron circuits.<sup>[326]</sup> A core computing operation closely related to the memristor crossbar is the vector matrix multiplication (VMM), which can be naturally implemented in dense crossbar geometries in a single-analog computational step utilizing Ohm's law and Kirchhoff's current law for summation.

Learning is an important part of neural network research, and its adaptability is achieved through learning. Based on changes in the environment, the weights are adjusted to improve the behavior of the system. According to different learning environments, neural network learning methods can be divided into supervised learning and unsupervised learning.

- In supervised learning, the sample data set is input into the network, the network output is compared with the expected output, and after training, each neuron converges to a weight. When the task is input, the neural network calculates the optimal solution. In layman's terms, we teach neural networks how to do things.
- In unsupervised learning, the sample data is input, but the expected output is not given, and the relationship between the data is obtained according to the clustering or a certain model. Therefore, unsupervised learning is more like self-learning, letting neural network learn to do things on their own.

Perceptron is the origin algorithm of ANN and belongs to supervised learning. In 2015, Prezioso et al. built an integrated transistor-free memristor crossbar neural network. As shown in Figure 20a,b, for a  $3 \times 3$  binary image,  $V_1$  to  $V_9$  are the input signals,  $V_{10}$  is a constant bias.  $W_{i,j}$  (with  $i = 1, 2, 3$  and  $j = 1, \dots, 10$ )

are the adjustable weight of synapses in the neural network. This is a single-layer perceptron with ten inputs and three outputs, fully connected with  $10 \times 3 = 30$  synaptic weights, and each weight corresponds to the difference between the conductance values of the two memristors

$$w_{ij} = G_{i,j}^+ - G_{i,j}^- \quad (1)$$

So that the total number of memristors in the crossbar was  $30 \times 2 = 60$  (Figure 20c). And  $I_i$  can be calculated using VMM

$$I_i = \sum_{j=1}^{10} W_{i,j} \cdot V_j \quad (2)$$

Therefore, as shown as Figure 20d, the input signal  $V_R$  in the crossbar is determined according to the color of the pixel ( $+V_R$  for dark colors and  $-V_R$  for light colors). For a specific error matrix, an example of weight adjustment is shown in the Figure 20e. At the step shown, only the synapses whose weights should be increased (marked by "+" in the table on the left) are adjusted, that is, the memristor conductances  $G_{1,1}^+$ ,  $G_{1,2}^+$ ,  $G_{1,5}^+$ ,  $G_{1,6}^+$ , and  $G_{1,9}^+$  are being increased.<sup>[328]</sup>

## 5.2. Deep Neural Network (DNN)

DNNs, also called deep learning, is a method of machine learning based on data representation learning. It is a machine learning method that can simulate the neural structure of the human brain. The concept of deep learning is derived from the research of ANNs. It is developed from the previous ANN model. DNN is a large category, including convolutional neural networks (CNNs), recurrent neural networks (RNNs), and generative adversarial networks (GANs) which have emerged in

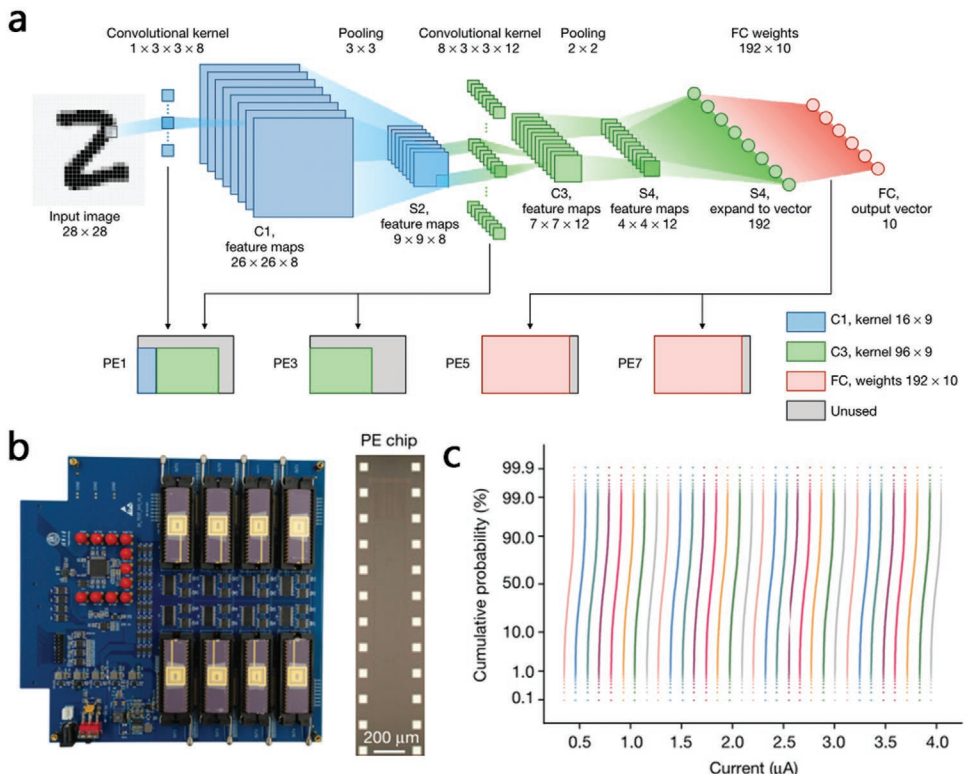


**Figure 21.** Hardware system of memristor-based CNNs. a) Structure of the five-layer memristor CNN used for MNIST image recognition, with alternating convolutional (C1, C3) and subsampling (S2, S4) layers. The input is a  $28 \times 28$  grayscale (8-bit) digit image. b) Left, Hardware implementation of (a): integrated PCB subsystem with 8 cores. Right, an enlarged view of the computing core formed by a  $128 \times 16$  memristor array. c) Cumulative probability distribution of 1024 cells with respect to 32 independent conductance states. Reproduced with permission.<sup>[248]</sup> Copyright 2020, Springer Nature.

recent years, etc. They have their own areas of expertise, for example, CNNs has remarkable ability in image processing and image recognition, RNNs has remarkable ability in processing sound and time series data, and GANs has remarkable ability in generating images. Among them, the memristor-based GAN is still in the simulation stage.<sup>[324,325]</sup>

The “depth” of deep learning refers to the number of hidden layers, so the more complicated the selection problem, the more hidden layers it requires. For example, AlphaGo’s hidden layers of strategy network is 13 layers, and the number of neurons in each layer is 192.<sup>[254]</sup> In this section, two types of DNNs that have been implemented using memristors are introduced.

### 5.2.1. Convolutional Neural Network

In the 1960s, Hubel and Wiesel, when studying neurons in the cat’s cerebral cortex for local sensitivity and direction selection, discovered that their unique network structure can effectively reduce the complexity of the feedback neural network, and then proposed a CNN.<sup>[246]</sup> In 1980, the new recognition machine proposed by Fukushima was the first implementation of a CNN.<sup>[247]</sup>

In CNNs, the neurons in the convolutional layer are only connected to some neuron nodes in the previous layer, that is, the connections between its neurons are not fully connected, and the weight  $w$  and offset  $b$  of the connections between some neurons in the same layer are shared, which greatly reduces the number

of training parameters required. Now, CNNs have become one of the research hotspots in many scientific fields, especially in the field of pattern recognition and classification. Since the network avoids complex preprocessing of the image and can directly input the original image, it has been more widely used. CNNs has achieved great success in the field of image processing and recognition. On the international standard ImageNet dataset, many successful models are based on CNNs.

Recently, Yao et al. constructed a five-layer CNN (Figure 21a) consisting of eight  $128 \times 16$  memristor crossbars (Figure 21b) to achieve high-performance number recognition. This array exhibits remarkably repeatable multilevel conductance states (Figure 21c). It is the first hardware implementation of in-memory computing based on memristor crossbar, and a hybrid training algorithm adapted to the characteristics of memristors and a new parallel architecture of convolution space are proposed. Compared with contemporary state-of-the-art GPUs, its power efficiency has improved by two orders of magnitude, and its performance density has increased by an order of magnitude. It is proved that memristor can be used by DNN to solve the CMOS physical limit problem.<sup>[248]</sup>

### 5.2.2. Hopfield Neural Network (HNN)

In the 1980s, John Hopfield proposed a new neural network,<sup>[275]</sup> which can solve a large class of pattern recognition problems,

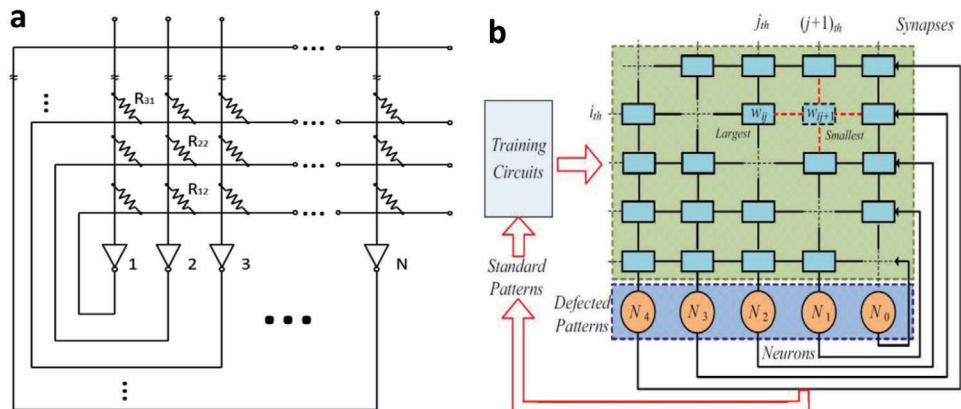


**Figure 22.** HNN schematic diagram of cyclic connection. a) A schematic of  $N$  analog amplifiers interconnected through a network of  $N^2$  resistors  $R$ , that connect the output of amplifier  $i$  to the input of amplifier  $j$ . b) HNN with synaptic weight. Reproduced with permission.<sup>[284]</sup> Copyright 2016, Springer.

and can also give an approximate solution to a class of combinatorial optimization problems. This neural network model is later referred to as the HNNs. HNN is a kind of RNN with feedback connections from output to input, which introduces the related ideas (kinetics) of physics into the structure of neural networks, thus forming HNNs. Each neuron is connected to all other neurons, also known as a fully interconnected network (Figure 22a). If HNN is a convergent stable network, the variation of this feedback and iterative calculation process becomes smaller and smaller. Once the stable equilibrium state is reached, the Hopfield network will output a stable constant value.<sup>[277]</sup> However, there may be no balance point, showing a hyperchaotic behavior.<sup>[276]</sup> In 2017, Kumar et al. used a NbO<sub>2</sub>-based Mott memristor to build an intrinsically coupled oscillator that drives the system to show chaotic behavior. It is further proved that the integration of chaotic oscillator can improve the HNNs implemented by hardware.<sup>[285]</sup>

Since the introduction of the model, HNNs has received extensive attention in various fields.<sup>[278,279]</sup> It has well-known capabilities to solve traveling salesman problems and location assignment problems.<sup>[280,281]</sup> But the traditional HNNs is realized by constructing MOS transistors as electronic synapses.<sup>[282]</sup> In 1987, Bell Labs successfully developed the first neural network chip based on HNN,<sup>[283]</sup> which brings new life to HNNs with the emergence of memristors, HNN based on memristor came into being. In 2015, Duan et al. proposed a “small world” HNNs model based on memristor, which is closer to the human brain neural network and show superior performance than the original regular nerve in digital identification, etc.<sup>[284]</sup> Figure 22b shows the small world HNN with synaptic weights.

HNNs also provides models that mimic human memory. In 2015, Kim et al. proposed a memristor-based synapse consisting of four memristor bridge circuits and three transistors.<sup>[286]</sup> In 2016, Yang et al. improved the memristor bridge circuit so that it can realize the synaptic operation of nerve cells without transistors. They use it to build a 3-bit memristor HNN, showing the ability of associative memory.<sup>[292]</sup> In addition, in 2017, Sheridan et al. reported an experimental implementation of a sparse coding algorithm using a biological heuristic method for the first time using a  $32 \times 32$  memristor cross-switch.<sup>[245]</sup> In 2019, Wang et al. for the first time achieve pattern and video

classification of field-trained large-scale redox memristor-based CNNs and convolutional RNNs.<sup>[249]</sup>

### 5.3. SNN

Real biological neurons communicate with each other using electrical pulses “spikes,” which affected Maass to write his influential paper: Networks of spiking neurons: the third generation of neural network models.<sup>[255]</sup>

As a third generation neural network model, SNN can realize higher-level biological neural simulation. In addition to neuron and synaptic states, SNN incorporates the concept of time into its operations. The current ANN is a second-generation neural network. They are usually fully connected, receiving consecutive values and outputting consecutive values. Although contemporary neural networks have enabled us to achieve breakthroughs in many fields, they are biologically inaccurate and do not mimic the working mechanisms of biological brain neurons. SNNs are fundamentally different from current popular neural networks and machine learning methods. There are three necessary conditions for building an SNN: external stimulus coding, building a neuron model, and developing learning rules.

Various encodings have been proposed so far, but they are all special cases of fully temporal code. In a fully temporal coding, coding relies on the precise timing of all spikes.<sup>[269]</sup> Binary encoding is all-or-nothing encoding: attractive due to its simplicity, but it completely ignores timing properties and the multiplicity of spikes. Rate coding is another abstraction of the timing nature of spikes because only the rate of the spikes in the interval is used as a measure of the transmitted information. Latency coding uses the timing of the spikes, rather than the multiplicity of the spikes, closely related to this is sequential coding, a coding around the order in which neurons emit their first peak.<sup>[268]</sup> Predictive spike coding provides a method to perform analog-to-digital conversion and digital-to-analog conversion at the somatic cells and synapses of neurons, respectively.<sup>[270–272]</sup> Probabilistic spike coding is related to the efficient use of spiking neurons for reasoning and is usually considered in the context of computational neuroscience.<sup>[273,274]</sup>

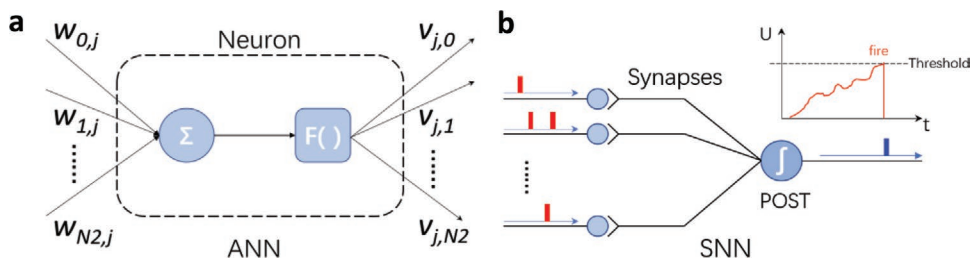


Figure 23. a) Traditional artificial neuron model. b) A LIF spiking neuron model.

SNN was born to bridge the gap between neuroscience and machine learning using models that are best suited for biological neuronal mechanisms. Real neurons in the human brain show a variety of spike behavior, and several spiking neurons models that has the biological characteristics of STDP learning rules have been proposed in order to simulate real neuron behavior. These models are usually expressed as various complex dynamic systems, the most famous of which is the Hodgkin–Huxley (H–H) model,<sup>[256]</sup> the Izhikevich model is a simplification of the Hodgkin–Huxley model,<sup>[257]</sup> others such as leakage-integration-fire (LIF) models, quadratic integral and launch models, and other more complex models, representing the different trade-offs between neuroscience realism and computational complexity. Among them, the LIF model is one of the most widely used models. An alternative to dynamic system models is the so-called spike response model (SRM),<sup>[258]</sup> in which the membrane potential does not need to be simulated by a differential equation, but the membrane potential is used as the sum of the integral kernels. In this view, a neuron (understood to include its incoming synapses) is equivalent to a mathematical operator as it maps the sequence of peaks in the input to the sequence of peaks in the output.<sup>[259]</sup>

Take the LIF model as an example. The ANN simply uses the weight to continuously calculate forward, as shown in Figure 23a, which finds the corresponding value of the middle layer, and then uses the back propagation (BP) to reduce the value of the loss function. But the SNN sends the nerve spikes (discrete events that occur at random points in time) instead of continuous values. The membrane potential of the neuron does not work in normal time, as long as the pulse is sent over, exceeding the threshold of the membrane potential, the excited neurons transmit a pulse forward (Figure 23b), thereby reducing energy consumption and calculating faster, and the membrane potential drops back to the original level immediately after the transfer, waiting for the next pulse. In addition, SNNs are usually sparsely connected and take advantage of special network topologies. Traditional ANNs requires layer by layer calculations, and the amount of calculation is much larger. Figure 24 shows two different models of spiking neurons. Among them, as shown as Figure 24a, Yi et al. designed a H–H Mott spiking neuron to achieve various neuron dynamics by changing the values of passive  $R$  and  $C$  elements without changing the parameters of the VO<sub>2</sub> device.<sup>[260]</sup> As shown as Figure 24b, Zhang et al. designed a LIF Mott spiking neuron, constructed high-performance hardware SNNs, and realized high-precision MNIST digital recognition.<sup>[289]</sup>

Although SNN is superior, compared to ANN, the challenge of SNN comes from several aspects.

First, when most error functions consider actual values and time continuity, in order to coordinate the discontinuity of the spikes, there are several solutions and their disadvantages.

- Linearize the spiking process, but only for occasions with fewer learning steps: Solutions like SpikeProp.<sup>[261]</sup>
- Smear out the spikes for a more continuous calculation: Re-SuMe algorithm.<sup>[262]</sup>
- Using a more complex uninterrupted spiking neuron model or using random neurons with potentially smooth transient ignition intensity, but the network complexity increases dramatically.<sup>[263,264]</sup>
- The predictive pulse coding method is actually approximately continuous signals, other methods rely on the extracted pulsed neuron information.<sup>[265,266]</sup>

Second, the encoding and decoding of pulses is the second challenge of SNN. One is that the neuroscience itself has yet to be explored. On the other hand, the labeling of rate coding or pulse time coding in SNN is also confusing. In principle, spiking neurons replace sigmoidal neurons, communication becomes sparse, and calculations only need to be performed when the link is activated, unlike traditional ANNs that are performed at each time step. But encoding and decoding are stumbling blocks.

Third, the reasonable correlation of pulsed neural computing with biologically pulsed neurons is also a challenge. Since the calculation of SNN is so similar to that of biological neural networks, there is reasonable to expect that there is a good interaction between computational-driven methods based on computational science and neuroscience based on data. Neuroscience tells us SNN models, and effective SNNs can clarify the calculation principles and neural coding behind phenomena such as STDP.<sup>[267]</sup>

#### 5.4. Pave the Way for SNN with Traditional ANN

Although the hardware implementation of SNN still has problems, some ANN hardware implementations are relatively easy. Recently, Rivu et al. designed the ANN–SNN converter using diffusion memristors and shunt capacitors (Figure 25).<sup>[288]</sup> This is equivalent to the value of a neuron in a traditional ANN, which is used to encode the frequency of the spike, also basically the way to implement SNN using memristor at this stage.

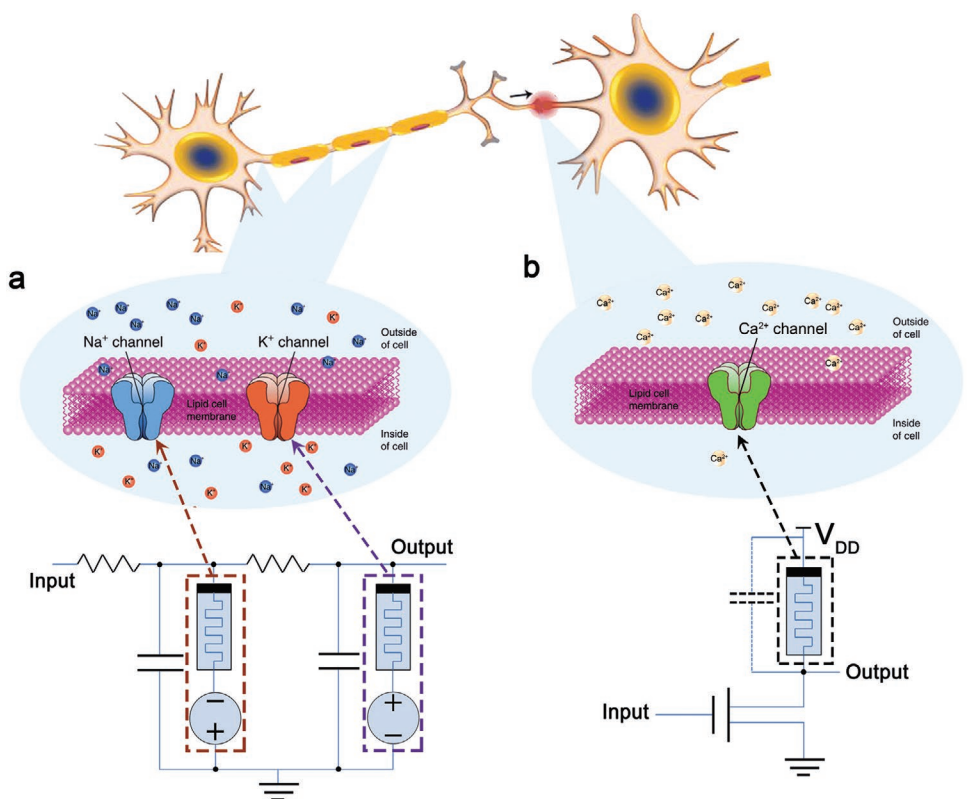


**Figure 24.** Two types of Mott spiking neurons. a) H–H neurons were constructed using two  $\text{VO}_2$ -based memristors, simulating the mechanism of voltage-gated  $\text{Na}^+$  and  $\text{K}^+$  ions passing through the cell membrane, enabling the generation and repetition of action potentials at the cell body and axon nodes. Adapted with permission.<sup>[260]</sup> Copyright 2018, Springer Nature. b) LIF neurons were constructed using  $\text{NbO}_2$ -based memristors, which simulated the inflow and outflow of voltage-gated  $\text{Ca}^{2+}$  ions at the presynapse to achieve the transmission of information between synapses. Adapted with permission.<sup>[289]</sup> Copyright 2019, IEEE.

## 6. Application

The biomimetic characteristics of the memristor as an electronic synapse and neuron have inspired the advent of new information technology in the neuromorphic computing. Innovation in information technology depends not only on complex

algorithms and programming, but also on novel materials and high-performance equipment to achieve human-computer interaction. The application of the memristors can be extended to the artificial nerves on condition of the presence of electronic receptors which can transfer the external stimuli to the internal nerve system. Memristor realizes high-speed 3D memory,

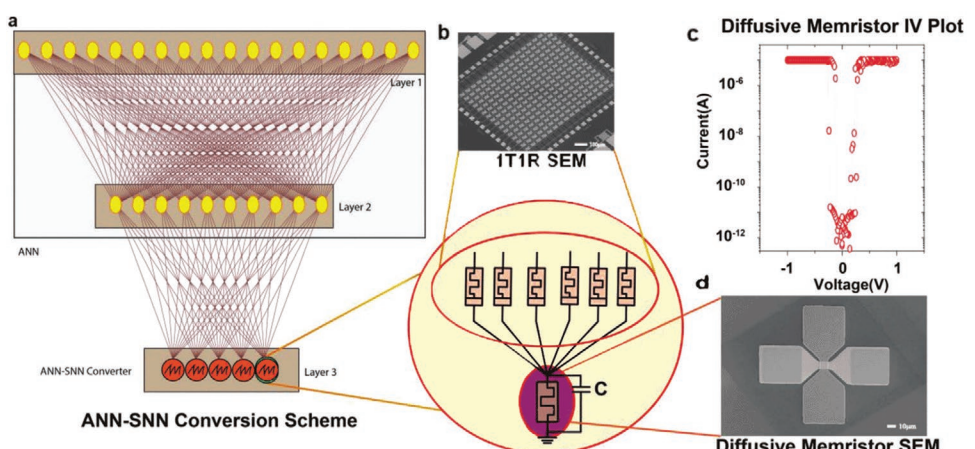


**Figure 25.** ANN–SNN conversion scheme. a) An ordinary two-layer ANN and a third-layer oscillatory neuron. b) SEM image of ANN. c) The I–V curve of a memristor used to create an oscillating neuron. d) SEM image of diffused memristor. Reproduced with permission.<sup>[288]</sup> Copyright 2019, Wiley-VCH.

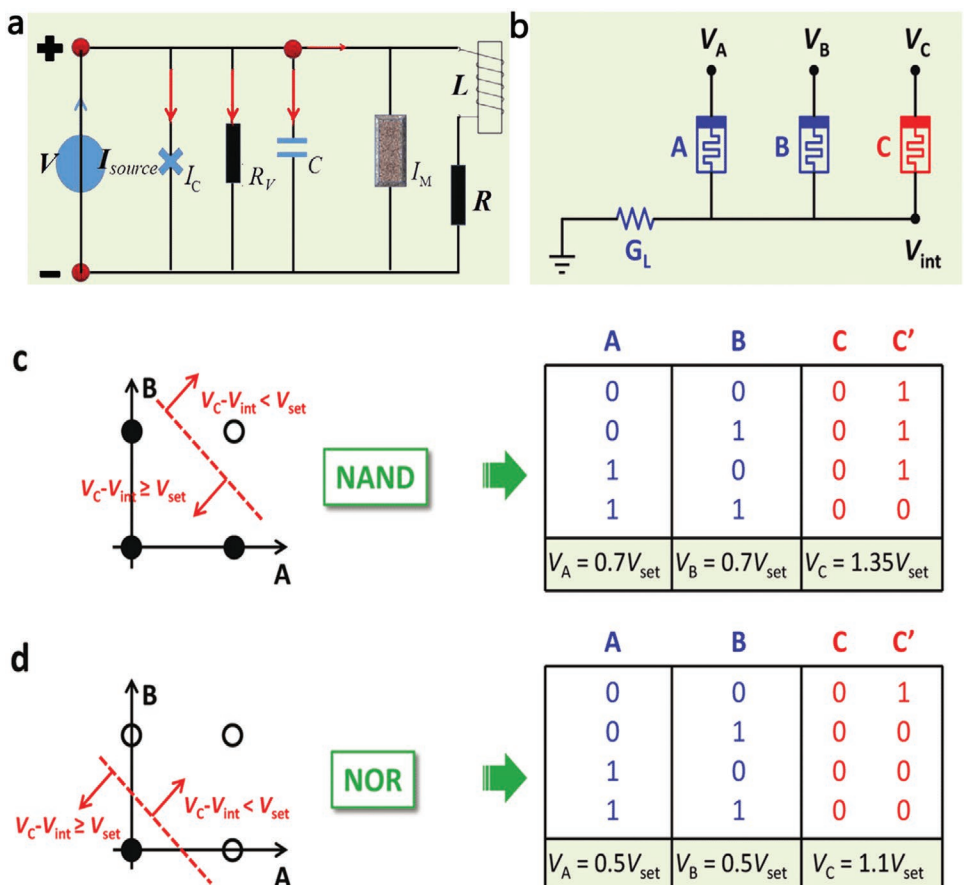


**Figure 26.** Memristor application in circuit. a) The scheme diagram for memristor-coupled circuit. Reproduced with permission.<sup>[290]</sup> Copyright 2018, Elsevier B.V. b) Schematic diagram of memristor array to implement logic gate function. c) NAND operation and d) NOR operation are realized by changing the applied voltage  $V_A$ ,  $V_B$ , and  $V_C$ . Reproduced with permission.<sup>[292]</sup> Copyright 2018, Wiley-VCH.

which will be widely used in integrated circuit disciplines, and will greatly promote the research and development of artificial intelligence to the practical direction.

### 6.1. Application of Active Circuit

As a new circuit element, the most intuitive application of memristor is in circuit applications, which is characterized by the use of memristor characteristics to improve circuit performance and simplify circuits. As early as 2008, Itoh et al. proved that memristors are very useful for oscillating circuits.<sup>[291]</sup> In 2018, Zhang et al. designed a Josephson junction circuit with memristor. It is found that appropriate parameters setting can induce distinct chaotic and periodical states by analyzing the output series. And the chaos encryption based on Josephson junction circuit coupled by memristor is investigated as well.<sup>[290]</sup> The scheme diagram for memristor-coupled circuit as shown in Figure 26a. In 2018, Sun et al. used only a few memristors to form a network, and implemented Boolean logic operations with extremely simple circuits. In addition to the NAND and NOR operations shown in Figure 26c,d, they also implemented XOR operations and one-bit full adder operations.<sup>[292]</sup> Significantly reduces the amount of circuit elements required for logic

gates. The emergence of memristor may inject new vitality into the circuit industry, and the application prospect is very broad.

### 6.2. Application of Bionics

After millions of years of development, natural materials have nearly perfect structures and functions, of which electron transfer is one of the most basic and delicate biological processes.<sup>[293]</sup> Figure 27a-d shows several biological materials used as the RS layer of the memristors, including lignin (Figure 27a), egg albumen (Figure 27b), hemolymph of the silkworm (Figure 27c), Silk protein fibroin (Figure 27d). Silk fibroin is a representative biomolecule and has been extensively studied.<sup>[294,295]</sup> In addition to proteins, sugars (especially polysaccharides) are also widely used as the basis for developing new green storage devices.<sup>[296]</sup> Recently, Fu et al. reported a type of diffusive memristor, fabricated from the protein nanowires harvested from the bacterium *Geobacter sulfurreducens*, that functions at the biological voltages of 40–100 mV. Artificial synapses built from these memristors not only function at biological action potentials (e.g., 100 mV, 1 ms) but also exhibit temporal integration close to that in biological neurons, and the potential of using

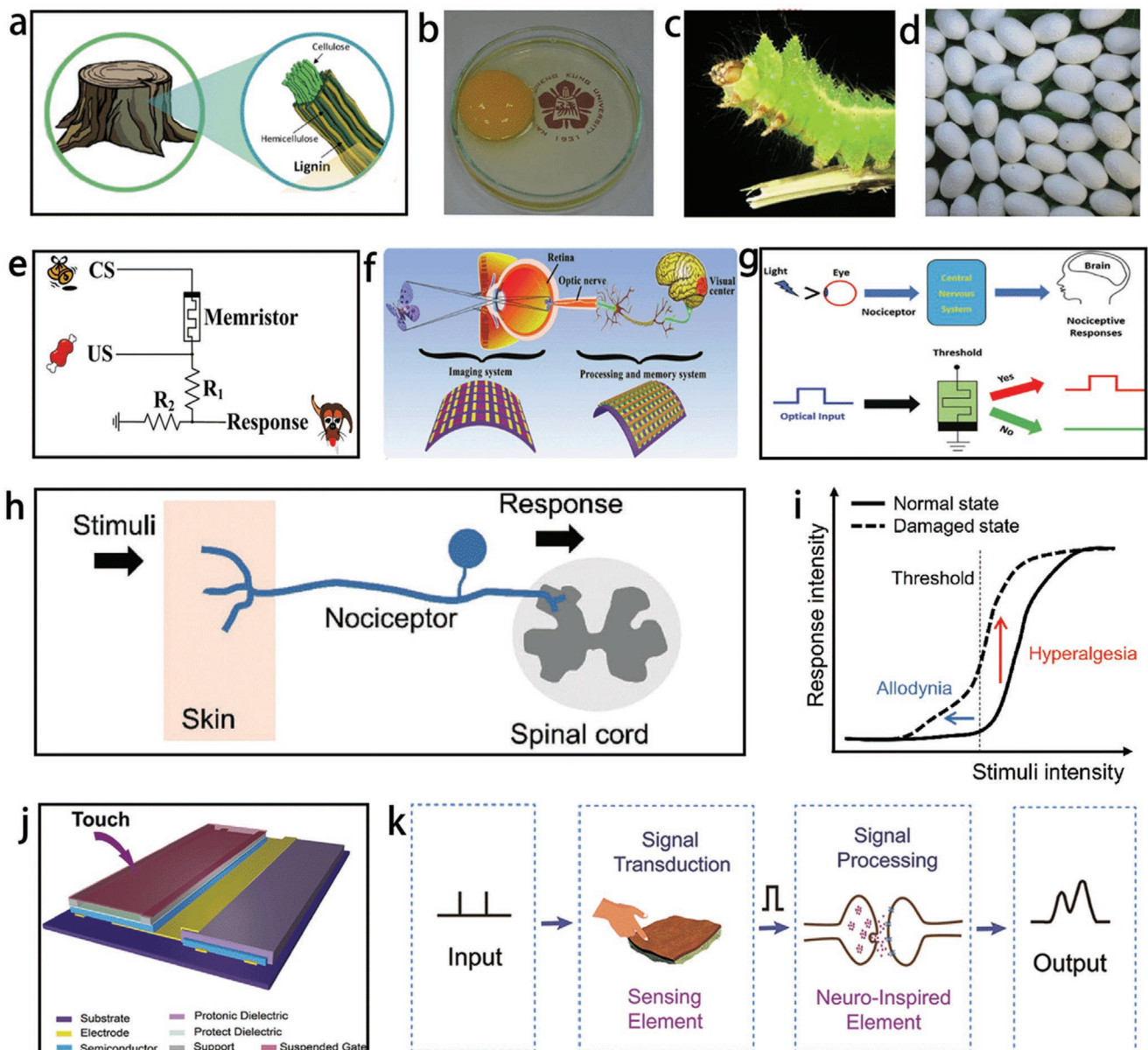


**Figure 27.** Several biomaterials and biomimetic synapses. a) Lignin, one of main components of plants. Reproduced with permission.<sup>[319]</sup> Copyright 2017, American Chemical Society. b) Chicken egg and the extracted egg albumen. Reproduced with permission.<sup>[320]</sup> Copyright 2015, Springer Nature. c) The hemolymph of the silkworm was obtained from the silkworm. Reproduced with permission.<sup>[318]</sup> Copyright 2017, Springer Nature. d) Silk protein fibroin. Reproduced with permission.<sup>[294]</sup> Copyright 2015, Wiley-VCH. e) Extinction and recovery of classical conditioning. Reproduced with permission.<sup>[321]</sup> Copyright 2015, Wiley-VCH. f) Visual memory devices based on memristor image sensors to imitate human visual memory. Reproduced with permission.<sup>[238]</sup> Copyright 2018, Wiley-VCH. g) Working mechanism of the human eye, and threshold-intensity-dependent photo response of the present photodetector. Reproduced with permission.<sup>[300]</sup> Copyright 2019, Wiley-VCH. h) A schematic diagram of the typical nociceptor nervous system. i) Typical stimuli versus response relation in the nociceptor in the normal and damaged states. Reproduced with permission.<sup>[301]</sup> Copyright 2018, Wiley-VCH. j) Schematic diagram of tactile sensing elements. k) Principle of artificial tactile perception system. Reproduced with permission.<sup>[302]</sup> Copyright 2017, Wiley-VCH.

the memristor to directly process biosensing signals is also demonstrated.<sup>[330]</sup> The application of biomaterials and the development of biomimetic devices have benefited from the intersection with biology.

The human body has a complex nervous system. Different types of neurons display different functions. The diversity of memristors makes it easy to simulate these functions. Pavlovian conditioning is a classic case of associative learning

in biological brain. Memristor simulations of Pavlov experiments have been extensively studied.<sup>[297–299]</sup> As shown as Figure 27e, Li et al. proposed a memristive neuromorphic circuit, which can make the classic Pavlov conditioned reflex under a series of conditioned stimuli (CS) and unconditioned stimuli (US).<sup>[321]</sup> In 2018, Chen et al. proposed a simple architecture is proposed, which uses a photoresistor to construct an flexible artificial visual memory system. This opens up new

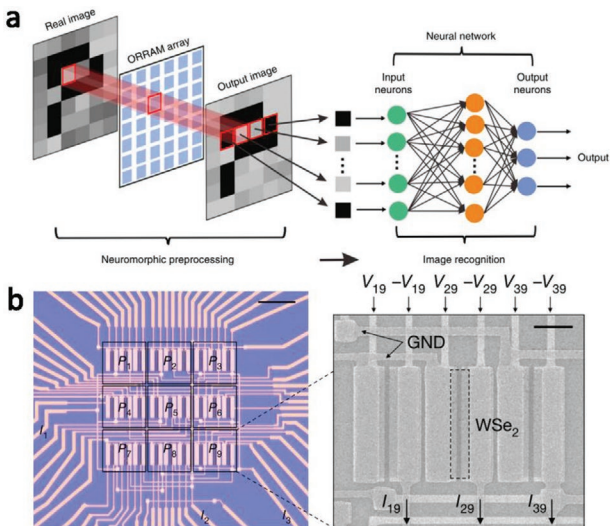


**Figure 28.** a) Illustration of an artificial neuromorphic visual system based on the ORRAM devices for image preprocessing and an artificial neural network for image recognition. Reproduced with permission.<sup>[323]</sup> Copyright 2019, Springer Nature. b) Microscope image of the photodiode array, which consists of  $3 \times 3$  pixels (scale bar, 15  $\mu\text{m}$ ), and SEM image of one of the pixels (scale bar, 3  $\mu\text{m}$ ). Reproduced with permission.<sup>[332]</sup> Copyright 2020, Springer Nature.

opportunities for imitating human visual memory. As shown in Figure 27f, a visual storage device based on a RS storage device and a resistive image sensor can mimic human visual storage.<sup>[238]</sup> The simulation schematic diagram is shown in Figure 27g.<sup>[300]</sup> In 2018, Kim et al. designed a solid-state nociceptor using the threshold switching characteristics of the Pt/Ti/HfO<sub>2</sub>/TiN structure (Figure 27h,i), which shows all thresholds of bionociceptors from a few milliseconds to tens of seconds over a wide time range, necessary functions of relaxation, analgesia, and hyperalgesia.<sup>[301]</sup> In 2017, Zang et al. designed a dual-organic-transistor-based tactile-perception element whose signal transduction and biomimetic signal processing capabilities enabled dynamic tactile sensing using organic transistors, as shown in Figure 27j,k.<sup>[302]</sup> The system has significant perceptual characteristics and has broad application prospects in flexible, low-cost bionic intelligent products and human-machine interface elements. In addition, in terms of hearing, Park et al. for the first time demonstrated an auditory recall on an MNN using electroencephalography experiment in 2013. It could be applied in the development of brain-machine interfaces for restoring speech in paralyzed individuals.<sup>[336]</sup> In 2019, Danesh et al. used MNN to perform simultaneous speech inference and learning in a parallel simulation mode, with an energy efficiency of about  $1.6 \times 10^{17}$  FLOPS W<sup>-1</sup>, which is about seven orders of magnitude higher than the Summit supercomputer.<sup>[335]</sup>

Machine vision technology has taken huge leaps in recent years, and is now becoming an integral part of various intelligent systems, including autonomous vehicles and robotics. After the emergence of photoelectric synapses, scientists began trying to combine volatile photodetectors with nonvolatile memristors to realize the perception and storage of images.<sup>[235–237]</sup> In 2018, such a system integrating perception and storage was

developed by Chen et al.<sup>[238]</sup> The following year, Zhou et al. reported a MoO<sub>x</sub>-based ORRAM, whose arrays are proof-of-concept to provide the potential to simplify neuromorphic vision system circuits and contribute to the development of edge computing and IoT applications. As shown as Figure 28a, the tunable synaptic plasticity of the array allows us to perform a first-stage image processing, such as image contrast enhancement and noise reduction, the efficiency and accuracy of subsequent image processing are greatly improved.<sup>[323]</sup>

With the development of memristive photoelectric synapses in recent years, neural networks based on photoelectric memristors have begun to appear. These networks can usually directly collect and process visual information. In 2019, Feldmann et al. used PCMs for the first time to realize the all-optical, integrated and scalable neuromorphic framework of SNN. Such photonic neurosynaptic networks promise access to the high speed and high bandwidth inherent to optical systems, thus enabling the direct processing of optical telecommunication and visual data.<sup>[331]</sup> In the same year, Zhai et al. used a near-infrared synapse to simulate a single-layer perceptron for supervised learning.<sup>[334]</sup> Recently, Mennel et al. demonstrated that an image sensor can itself constitute an ANN that can simultaneously sense and process optical images. Figure 28b shows an image sensor array that can identify  $3 \times 3$  pixel images, where each pixel consists of three WSe<sub>2</sub> photodiodes/subpixels. The device realizes ultra-fast pattern recognition within 50 ns. The implementation of an analogue deep-learning network becomes feasible by converting the photocurrents into voltages that are then fed into a memristor crossbar.<sup>[332]</sup> Subsequently, Wang et al. used WSe<sub>2</sub>/h-BN/Al<sub>2</sub>O<sub>3</sub> heterostructure device to construct a visual sensor for retinal morphology, which not only realizes the preprocessing of the input image, but also can be used as CNN to realize image recognition.<sup>[303]</sup>

In 2018, Li et al. monolithically integrate HfO<sub>2</sub>-based memristors with a foundry made transistor array into a multiple-layer DNN, which has 97% accuracy and adaptive learning ability comparable to CMOS in the classification of standard machine learning data sets (Figure 29a,b). The ability of on-site learning is proved by experiments, and the competitive classification accuracy is obtained, which proves the adaptive ability of the training algorithm to hardware defects when 11% of the devices are not working (Figure 29c,d).<sup>[309]</sup> In the same year, Jang et al. realized face recognition and classification simulation by using a three layers flexible memristor ANN based on poly 1,3,5-trivinyl-1,3,5-trimethylcyclotrisiloxane (pV3D3) (Figure 29e-h).<sup>[304]</sup> Of course, these are just the tip of the iceberg for memristors and MNNs applications. The uses of MNNs to implement functions such as walking gait classification,<sup>[315]</sup> CIFAR-10 classification<sup>[316,317]</sup> and other MNNs have sprung up. The application of memristor will be more colorful in the future.

## 7. Summary and Outlook

The advantages of MNNs are the speed and energy efficiency in the calculation process, which are reflected in two aspects: one is in device level, the energy of calculation and weight change is the lowest; the other is in structure level, computing is

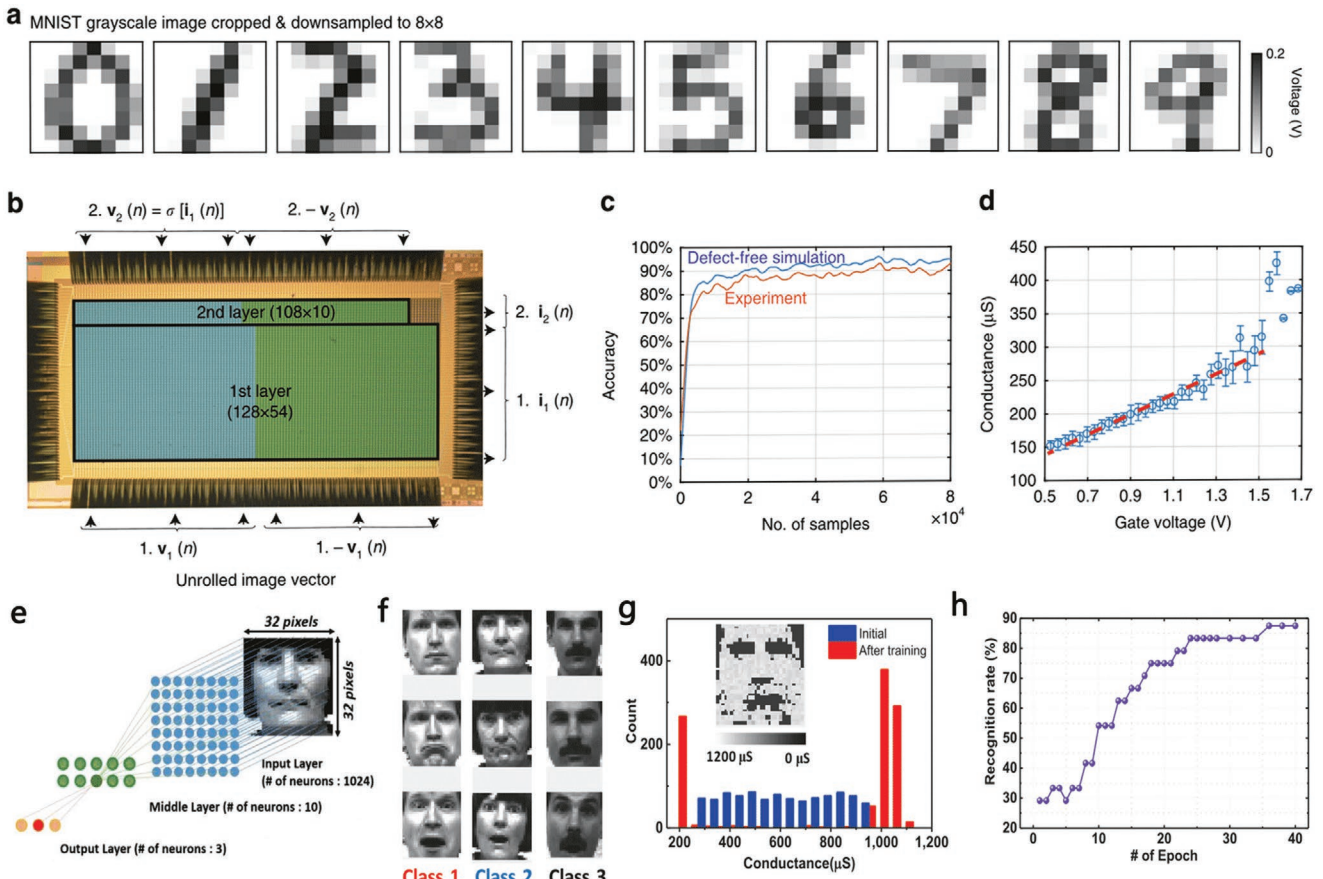


**Figure 29.** Implementation of face recognition and digital recognition. a) Typical handwritten digits. b) Photograph of  $128 \times 64$  integrated array during measurement. c) Experimental data and nondefective simulation results. d) Extract the relationship between conductance and gate voltage during training. Reproduced with permission.<sup>[309]</sup> Copyright 2018, Springer Nature. e) A two-layer ANN for face recognition. The input neurons are connected to the pixels of the input image. f) Nine training pictures of three people. g) Conductance distribution of initial state and post-training state. The illustration is a simulated visual picture. h) Relation between recognition rate and training time. Reproduced with permission.<sup>[304]</sup> Copyright 2019, American Chemical society.

performed in parallel where the information is stored, avoiding data movement and memory wall problems in traditional digital computing. But there are some problems we need to solve in the future.

### 7.1. Memristor Performance Optimization

The advantages of memristors are nonvolatile, high density, high integration, high speed, low power consumption, flexible reconfigurability and so on. Although significant progress has been made in this area in recent years, many challenges remain. For neural network applications, a wide range of resistance values are required to contain more resistance states. The multiresistance of the device can be adjusted by changing the size, quantity or composition of the diameter of the conductance channel or the tunnel gap. Unfortunately, once a metal bridge is formed, reducing its size is often a mutation process. Although a wide range of resistance values can be obtained by adjusting distance of the tunnel gap, this will cause nonlinearity in the  $I$ - $V$  characteristics, because the tunneling current

and the gap size are exponentially dependent. Adjusting the composition may be an effective way. In addition, the channel resistance of the three-terminal ion transistor can also be realized by adjusting the externally doped concentration gradient gate. It should be pointed out that the complex value of the programmable pulse to achieve the change of resistance will inevitably increase the energy consumption.

The very large-scale integration of memristors is hampered by parasitic line resistance and device variability. To address integration challenges, 3D overlays can be a potential solution.<sup>[329]</sup> To address parasitic line resistance, approximate model containing only a few known parameters can be used to compensate for the effects of line resistance.<sup>[327]</sup>

The most important aspect of device variability is the resistance drift, which changes over time or the environment, which can result in undesirable changes in the touch off weight, which can affect the accuracy of the calculation. This problem is more prominent in the sulfur cluster compound phase-change material. The change in the target resistance of a programmable device can blur the difference between resistance levels and levels, which is the main influence factor affecting the accuracy

of the analog calculation. Improvements can be made in three aspects: material device engineering, circuit design, and system design. In material device engineering, for example, doping and dislocation can be used to constrain the size of the CF.<sup>[157,305]</sup> In circuit design, such as the method of encoding the resistance ratio of a memristor by two series memristors and a minimum size transistor.<sup>[306]</sup> In terms of system design, device bias can be reduced by running a protocol, i.e., a closed-loop peripheral circuit with write-verify function.<sup>[307]</sup> Others such as combine long-term storage, near-linear updates of volatile capacitors, and weight-data transfer with “polarity inversion” to cancel out inherent device-to-device variations.<sup>[308]</sup> Conversely, the inherent randomness of RS behavior is one of the useful features of analog biological systems, because randomness plays an important role in the calculation of fault tolerance and robustness of low-precision and noisy devices. Help the system to get rid of the local minimum to reach the global minimum.<sup>[309]</sup>

In neural network calculations, the calculation of Ohm's law requires that the memristor has a good *I*-*V* linear relationship, so that electrical pulses of different amplitudes can be conveniently used for multiplication calculations. Unfortunately, the memristor has a good *I*-*V* linearity in the high conductance range, but the corresponding current is also relatively large. If the low conductance range is utilized, the *I*-*V* linearity is relatively poor, and the resistance has large fluctuations. Generally, pulses with different widths and the same amplitude are used to query the conductance state of the memory and measure the output charge after multiplication. At a fixed amplitude, the charge  $Q = V$  (voltage)  $\times G$  (conductance)  $\times t$  (pulse width). This allows calculations with a low conductance range to facilitate power reduction and a simple peripheral modulation circuit.<sup>[310,311]</sup>

The last point is that linear and symmetric weights are important for the efficiency of network training. That is to say, the device conductance increases (excited) under one polarity (squeezing) under the other polarity, and they should have the same amount of excitation and suppression for the same electrical pulse. Most memristive devices are nonlinear dynamics, and the switching behavior exhibits asynchronous excitement and suppression. Regarding symmetry, it is also possible to deal with both devices and circuits. For example, devices with opposite weights are connected in series to compensate for asynchrony,<sup>[314]</sup> other methods such as optimizing programming pulses<sup>[313]</sup> or using weight-changing rules that are more tolerant of nonlinear programming.<sup>[312]</sup> With some further optimizations, including device variability reduction and device-circuit-architecture-algorithm codesign, processing-in-memristors may become a mainstream computing paradigm for the next generation machine learning platforms.<sup>[333]</sup>

## 7.2. Neural Network System Construction

Although memristor-based DNNs have shown better performance beyond CMOS, DNNs belong to ANNs in a broad sense and have not escaped the category of second generation neural networks. Therefore, DNNs (especially GANs) is only the recent application target of memristor, and the third generation neural networks (SNNs) is the long-term application target of memristor.<sup>[326]</sup>

At first glance, the SNN approach is like a retrogression. We move from continuous output to binary output, and the training of these spikes is not very interpretable. However, spike training enhances our ability to process spatiotemporal data (or real-world sensory data). Space refers to neurons and time refers to spike training. This allows us to process time data naturally without the need for RNN to add extra complexity. It has been proven that spiking neurons are more powerful computational units than traditional artificial neurons.

However, the widespread application of SNN still faces many challenges. Mainly because the discrete and sparse nature of neuron spike behavior makes spike training nondifferentiable, we cannot use gradient descent to train SNN without losing accurate time information. Therefore, although we have unsupervised learning methods (e.g., STDP and Hebb), but it can only be used to solve specific tasks, in order to properly use SNN to solve more challenging real-world tasks (such as regression analysis/inference/temporal pattern recognition, etc.), we need to develop an efficient supervised learning method. This is a daunting task because it involves, given the biological realism of these networks, determining how the human brain learns. Another problem is that it takes a lot of computing power to simulate SNN on normal hardware, because it needs to simulate differential equations. Due to the complexity of impulsive neural networks, researchers have not yet found an effective learning algorithm. The algorithm is required to conform to the characteristics of biological neural networks (growth and death).

In summary, in the future work, in order to adapt to the application of SNN, on the one hand, we urgently need excellent functional material. The memristor based on this material needs to have a wide range of resistance values, low resistance value fluctuations and drift, linear and symmetric weight changes, as well as high absolute resistance values for inference, and require high durability to facilitate repeated programming and training. At the same time, both cost and process difficulty must be considered to facilitate high-density monolithic integration. On the other hand, we need to formulate a general SNN algorithm to reasonably correlate impulsive neural calculations with biological impulsive neurons. The development needs to integrate different disciplines (engineering, biology, physics, etc.) and different levels (algorithms, architectures, systems, circuits, equipment, materials, etc.). Reassuringly, many teams are working on developing SNN supervised learning rules, and we are optimistic about the future of SNN.

Today, memristor-based SNNs are far from being practical tools for most tasks. Although there are some SNN applications in real-time image and audio processing, it is still in the experimental stage. Most memristor-based SNN works are either theoretical or show performance in a simple fully connected second-generation network.<sup>[288,289]</sup> But it should be believed that memristor-based SNNs and biological neurology can have more powerful interactions. The biologically plausible SNNs brings hope for the realization of the brain-computer interface, in the future, it may become a part of the human brain or instead of the human brain to realize information storage and thinking. With the development of diverse neural devices, such as flexible subcutaneous implantation devices, artificial biological sensory systems, a “machine man” in the real sense seems to be close at hand.

## Acknowledgements

This work was financially supported by the National Natural Science Foundation of China (grant nos. 61674050, 61874158, 61825404, and 61732020), the Top-Notch Youth Project in Hebei Province (grant no. BJ2014008), the Outstanding Youth Project of Hebei Province (grant no. F2016201220), the Support Program for the Top Young Talents of Hebei Province (grant no. 70280011807), Training and Introduction of High-Level Innovative Talents of Hebei University (grant no. 801260201300), and Hundred Persons Plan of Hebei Province (grant no. 606999919001). Figures 6, 8, and 19 and the biography for J.C. were updated on February 17, 2021 after initial online publication.

## Conflict of Interest

The authors declare no conflict of interest.

## Keywords

artificial synapses, memristor, neural networks, neuromorphic calculations, resistive switching mechanism

Received: August 11, 2020

Revised: October 15, 2020

Published online: November 13, 2020

- [1] L. Chua, *IEEE Trans. Circuit Theory* **1971**, *18*, 507.
- [2] D. B. Strukov, G. S. Snider, D. R. Stewart, R. S. Williams, *Nature* **2008**, *453*, 80.
- [3] G. E. Moore, *Cramming More Components Onto Integrated Circuits*, McGraw-Hill, NY, USA **1965**, 114.
- [4] J. Von Neumann, *IEEE Ann. Hist. Comput.* **1993**, *15*, 27.
- [5] J. Backus, *Commun. ACM* **1978**, *21*, 613.
- [6] W. A. Wulf, S. A. McKee, *ACM SIGARCH Comput. Archit. News* **1995**, *23*, 20.
- [7] NVIDIA Launches the World's First Graphics Processing Unit: GeForce256, [http://www.nvidia.com/object/IO\\_20020111\\_5424.html](http://www.nvidia.com/object/IO_20020111_5424.html) (accessed: February 2020).
- [8] N. P. Jouppi, A. Borchers, R. Boyle, P. Cantin, C. Chao, C. Clark, J. Coriell, M. Daley, M. Dau, J. Dean, B. Gelb, C. Young, T. V. Ghaemmaghami, R. Gottipati, W. Gulland, R. Hagmann, C. R. Ho, D. Hogberg, J. Hu, R. Hundt, D. Hurt, J. Ibarz, N. Patil, A. Jaffey, A. Jaworski, A. Kaplan, H. Khaitan, D. Killebrew, A. Koch, N. Kumar, et al., in *Proc. of the 44th Annual Int. Symp. on Computer Architecture – ISCA '17*, ACM Press, Toronto, CA **2017**, pp. 1–12.
- [9] J. D. Owens, M. Houston, D. Luebke, S. Green, J. E. Stone, J. C. Phillips, *Proc. IEEE* **2008**, *96*, 879.
- [10] S. Borkar, A. A. Chien, *Commun. ACM* **2011**, *54*, 67.
- [11] W. H. Kautz, *IEEE Trans. Comput.* **1969**, *C-18*, 719.
- [12] S. A. Wolf, D. D. Awschalom, R. A. Buhrman, J. M. Daughton, V. S. von Molnár, M. L. Roukes, A. Y. Chtchelkanova, D. M. Treger, *Science* **2001**, *294*, 1488.
- [13] S. Stathopoulos, L. Michalas, A. Khiat, A. Serb, T. Prodromakis, *Sci. Rep.* **2019**, *9*, 19412.
- [14] N. Locatelli, V. Cros, J. Grollier, *Nat. Mater.* **2014**, *13*, 11.
- [15] T. Mikolajick, C. Dehm, W. Hartner, I. Kasko, M. J. Kastner, N. Nagel, M. Moert, C. Mazure, *Microelectron. Reliab.* **2001**, *41*, 947.
- [16] M. M. Waldrop, *Nat. News* **2016**, *530*, 144.
- [17] L. Chua, *Appl. Phys. A* **2011**, *102*, 765.
- [18] W. Lu, C. M. Lieber, *Nanoscience And Technology: A Collection of Reviews from Nature Journals*, World Scientific, Singapore **2010**, p. 137.
- [19] S. Han, Y. Zhou, V. Roy, *Adv. Mater.* **2013**, *25*, 5425.
- [20] N. J. Tao, *Nanoscience And Technology: A Collection of Reviews from Nature Journals*, World Scientific, Singapore **2010**, p. 185.
- [21] T. Hasegawa, K. Terabe, T. Tsuruoka, M. Aono, *Adv. Mater.* **2012**, *24*, 252.
- [22] S. Liu, W. M. Wang, A. L. Briseno, S. C. Mannsfeld, Z. Bao, *Adv. Mater.* **2009**, *21*, 1217.
- [23] J. C. Scott, L. D. Bozano, *Adv. Mater.* **2007**, *19*, 1452.
- [24] W. Lu, D. S. Jeong, M. Kozicki, R. Waser, *MRS Bull.* **2012**, *37*, 124.
- [25] Y. Yang, P. Gao, L. Li, X. Pan, S. Tappertzhofen, S. Choi, R. Waser, I. Valov, W. D. Lu, *Nat. Commun.* **2014**, *5*, 1.
- [26] A. Pirovano, K. Schuegraf, *Nat. Nanotechnol.* **2010**, *5*, 177.
- [27] A. Sawa, *Mater. Today* **2008**, *11*, 28.
- [28] W. P. Lin, S. J. Liu, T. Gong, Q. Zhao, W. Huang, *Adv. Mater.* **2014**, *26*, 570.
- [29] S. Tappertzhofen, I. Valov, T. Tsuruoka, T. Hasegawa, R. Waser, M. Aono, *ACS Nano* **2013**, *7*, 6396.
- [30] M. D. Ventra, Y. V. Pershin, *Mater. Today* **2011**, *14*, 584.
- [31] H. P. Wong, H. Lee, S. Yu, Y. Chen, Y. Wu, P. Chen, B. Lee, F. T. Chen, M. Tsai, *Proc. IEEE* **2012**, *100*, 1951.
- [32] M. D. Groner, F. H. Fabreguette, J. W. Elam, S. M. George, *Chem. Mater.* **2004**, *16*, 639.
- [33] J. Y. Son, C. H. Kim, J. H. Cho, Y. Shin, H. M. Jang, *ACS Nano* **2010**, *4*, 3288.
- [34] H. Tabata, H. Tanaka, T. Kawai, *Appl. Phys. Lett.* **1994**, *65*, 1970.
- [35] N. Gergel-Hackett, B. Hamadani, B. Dunlap, J. Suehle, C. Richter, C. Hacker, D. Gundlach, *IEEE Electron Device Lett.* **2009**, *30*, 706.
- [36] J. M. Luo, S. P. Lin, Y. Zheng, B. Wang, *Appl. Phys. Lett.* **2012**, *101*, 062902.
- [37] Y. Lee, X. Zhang, W. Zhang, M. Chang, C. Lin, K. Chang, Y. Yu, J. T. Wang, C. Chang, L. Li, *Adv. Mater.* **2012**, *24*, 2320.
- [38] W. Chen, J. Zhao, J. Zhang, L. Gu, Z. Yang, X. Li, H. Yu, X. Zhu, R. Yang, D. Shi, *J. Am. Chem. Soc.* **2015**, *137*, 15632.
- [39] Y. Wang, Y. Chen, F. Xue, F. Zhou, Y. Chang, B. Fowler, J. C. Lee, *Appl. Phys. Lett.* **2012**, *100*, 083502.
- [40] N. C. Patra, S. Bharatan, J. Li, M. Tilton, S. Iyer, *J. Appl. Phys.* **2012**, *111*, 083104.
- [41] D. Fu, X. Zhao, Y. Zhang, L. Li, H. Xu, A. Jang, S. I. Yoon, P. Song, S. M. Poh, T. Ren, *J. Am. Chem. Soc.* **2017**, *139*, 9392.
- [42] D. Panda, T. Tseng, *Thin Solid Films* **2013**, *531*, 1.
- [43] J. J. Yang, N. P. Kobayashi, J. P. Strachan, M. Zhang, D. A. Ohlberg, M. D. Pickett, Z. Li, G. Medeiros-Ribeiro, R. S. Williams, *Chem. Mater.* **2011**, *23*, 123.
- [44] S. Park, J. Lee, J. S. Jang, H. Rhu, H. Yu, B. Y. You, C. S. Kim, K. J. Kim, Y. J. Cho, S. Baik, *Nanotechnology* **2013**, *24*, 295202.
- [45] P. F. Siles, M. de Pauli, C. C. B. Bufon, S. O. Ferreira, J. Bettini, O. G. Schmidt, A. Malachias, *Nanotechnology* **2013**, *24*, 035702.
- [46] T. H. Kim, E. Y. Jang, N. J. Lee, D. J. Choi, K. Lee, J. Jang, J. Choi, S. H. Moon, J. Cheon, *Nano Lett.* **2009**, *9*, 2229.
- [47] A. Younis, D. Chu, I. Mihail, S. Li, *ACS Appl. Mater. Interfaces* **2013**, *5*, 9429.
- [48] S. Pi, C. Li, H. Jiang, W. Xia, H. Xin, J. J. Yang, Q. Xia, *Nat. Nanotechnol.* **2019**, *14*, 35.
- [49] B. J. Choi, A. C. Torrezan, J. P. Strachan, P. G. Kotula, A. J. Lohn, M. J. Marinella, Z. Li, R. S. Williams, J. J. Yang, *Adv. Funct. Mater.* **2016**, *26*, 5290.
- [50] Y. B. Nian, J. Strozier, N. J. Wu, X. Chen, A. Ignatiev, *Phys. Rev. Lett.* **2007**, *98*, 146403.
- [51] J. J. Yang, M. D. Pickett, X. Li, D. A. Ohlberg, D. R. Stewart, R. S. Williams, *Nat. Nanotechnol.* **2008**, *3*, 429.
- [52] J. H. Hur, M. Lee, C. B. Lee, Y. Kim, C. Kim, *Phys. Rev. B* **2010**, *82*, 155321.
- [53] M. Wuttig, N. Yamada, *Nat. Mater.* **2007**, *6*, 824.
- [54] X. Wang, T. Song, F. Gong, P. Zheng, *Sci. Rep.* **2016**, *6*, 27624.
- [55] C. Poon, K. Zhou, *Front. Neurosci.* **2011**, *5*, 108.

- [56] A. Taherkhani, A. Belatreche, Y. Li, G. Cosma, L. P. Maguire, T. M. McGinnity, *Neural Networks* **2020**, 122, 253.
- [57] B. Govoreanu, C. Adelmann, A. Redolfi, L. Zhang, S. Clima, M. Jurczak, *IEEE Electron. Device Lett.* **2013**, 35, 63.
- [58] S. Bhattacharjee, E. Caruso, N. McEvoy, C. Ó Coileáin, K. O'Neill, L. Ansari, G. S. Duesberg, R. Nagle, K. Cherkaoui, F. Gity, *ACS Appl. Mater. Interfaces* **2020**, 12, 6022.
- [59] H. Kim, M. Choi, J. M. Suh, J. S. Han, S. G. Kim, Q. Van Le, S. Y. Kim, H. W. Jang, *NPG Asia Mater.* **2020**, 12, 1.
- [60] J. Shin, I. Kim, K. P. Biju, M. Jo, J. Park, J. Lee, S. Jung, W. Lee, S. Kim, S. Park, *J. Appl. Phys.* **2011**, 109, 033712.
- [61] S. Liu, N. Lu, X. Zhao, H. Xu, W. Banerjee, H. Lv, S. Long, Q. Li, Q. Liu, M. Liu, *Adv. Mater.* **2016**, 28, 10623.
- [62] L. G. S. Albano, T. Parra Vello, D. H. S. de Camargo, R. M. L. Da Silva, A. C. M. Padilha, A. Fazzio, C. C. B. Bufon, *Nano Lett.* **2020**, 20, 1080.
- [63] K. M. Kim, S. J. Song, G. H. Kim, J. Y. Seok, M. H. Lee, J. H. Yoon, J. Park, C. S. Hwang, *Adv. Funct. Mater.* **2011**, 21, 1587.
- [64] S. Wu, L. Ren, J. Qing, F. Yu, K. Yang, M. Yang, Y. Wang, M. Meng, W. Zhou, X. Zhou, *ACS Appl. Mater. Interfaces* **2014**, 6, 8575.
- [65] F. Alibart, E. Zamanidoost, D. B. Strukov, *Nat. Commun.* **2013**, 4, 2072.
- [66] C. Li, M. Hu, Y. Li, H. Jiang, N. Ge, E. Montgomery, J. Zhang, W. Song, N. Dávila, C. E. Graves, *Nat. Electron.* **2018**, 1, 52.
- [67] J. J. Yang, *Memristor Crossbar Arrays for Analog and Neuromorphic Computing*, University of Massachusetts, Amherst, United States **2018**.
- [68] R. Fang, W. Chen, L. Gao, W. Yu, S. Yu, *IEEE Electron. Device Lett.* **2015**, 36, 567.
- [69] U. Das, S. Bhattacharjee, B. Mahato, M. Prajapat, P. Sarkar, A. Roy, *Mater. Sci. Semicond. Process.* **2020**, 107, 104837.
- [70] K. Baek, S. Park, J. Park, Y. Kim, H. Hwang, S. H. Oh, *Nanoscale* **2017**, 9, 582.
- [71] M. D. Pickett, D. B. Strukov, J. L. Borghetti, J. J. Yang, G. S. Snider, D. R. Stewart, R. S. Williams, *J. Appl. Phys.* **2009**, 106, 074508.
- [72] K. Gopalakrishnan, R. S. Shenoy, C. T. Rettner, K. Virwani, D. S. Bethune, R. M. Shelby, G. W. Burr, A. Kellock, R. S. King, K. Nguyen, A. N. Bowers, M. Jurich, B. Jackson, A. M. Friz, T. Topuria, P. M. Rice, B. N. Kurdi, in *2010 Symp. on VLSI Technology*, IEEE, Honolulu, HI **2010**, pp. 205–206.
- [73] B. Chakrabarti, M. A. Lastras-Montaño, G. Adam, M. Preziosi, B. Hoskins, M. Payvand, A. Madhavan, A. Ghofrani, L. Theogarajan, K. Cheng, *Sci. Rep.* **2017**, 7, 42429.
- [74] B. Govoreanu, A. Redolfi, L. Zhang, C. Adelmann, M. Popovici, S. Clima, H. Hody, V. Paraschiv, I. P. Radu, A. Franquet, J. C. Liu, J. Swerts, O. Richard, H. Bender, L. Altimime, M. Jurczak, in *2013 IEEE Int. Electron Devices Meeting (IEDM)*, IEEE, Washington, DC **2013**, 10.2.1.
- [75] H. B. Lv, Q. Liu, Y. T. Li, M. Wang, X. Y. Liu, H. T. Sun, H. W. Xie, X. Y. Yang, Z. L. Huo, S. B. Long, M. Liu, in *2013 5th IEEE Int. Memory Workshop*, IEEE, Monterey, CA **2013**, pp. 182–183.
- [76] J. Jang, S. Park, G. W. Burr, H. Hwang, Y. Jeong, *IEEE Electron. Device Lett.* **2015**, 36, 457.
- [77] P. Yao, H. Wu, B. Gao, S. B. Eryilmaz, X. Huang, W. Zhang, Q. Zhang, N. Deng, L. Shi, H. P. Wong, *Nat. Commun.* **2017**, 8, 1.
- [78] M. Son, et al., *IEEE Electron. Device Lett.* **2011**, 32, 1579.
- [79] H. Nili, S. Walia, S. Balendhran, D. B. Strukov, M. Bhaskaran, S. Sriram, *Adv. Funct. Mater.* **2014**, 24, 6741.
- [80] W. Wang, B. Zhang, H. Zhao, *Results Phys.* **2020**, 16, 103001.
- [81] N. Raeis-Hosseini, S. Lim, H. Hwang, J. Rho, *Adv. Electron. Mater.* **2018**, 4, 1800360.
- [82] X. Yan, X. Li, Z. Zhou, J. Zhao, H. Wang, J. Wang, L. Zhang, D. Ren, X. Zhang, J. Chen, *ACS Appl. Mater. Interfaces* **2019**, 11, 18654.
- [83] X. Yan, L. Zhang, Y. Yang, Z. Zhou, J. Zhao, Y. Zhang, Q. Liu, J. Chen, *J. Mater. Chem. C* **2017**, 5, 11046.
- [84] J. Yao, Z. Sun, L. Zhong, D. Natelson, J. M. Tour, *Nano Lett.* **2010**, 10, 4105.
- [85] K. M. Kim, G. H. Kim, S. J. Song, J. Y. Seok, M. H. Lee, J. H. Yoon, C. S. Hwang, *Nanotechnology* **2010**, 21, 305203.
- [86] W. Guan, S. Long, Q. Liu, M. Liu, W. Wang, *IEEE Electron. Device Lett.* **2008**, 29, 434.
- [87] V. Jousseaume, J. Buckley, Y. Bernard, P. Gonon, C. Vallée, M. Mougenot, H. Feldis, S. Minoret, G. Chamiot-Maitral, A. Persico, A. Zenasni, M. Gely, J. P. Barnes, E. Martinez, H. Grampeix, C. Guedj, J. F. Nodin, B. De Salvo, in *2009 IEEE Int. Interconnect Technology Conf.*, IEEE, Sapporo, JP **2009**, pp. 41–43.
- [88] A. Shih, W. Zhou, J. Qiu, H. Yang, S. Chen, Z. Mi, I. Shih, *Nanotechnology* **2010**, 21, 125201.
- [89] S. Z. Rahaman, Y. Lin, H. Lee, Y. Chen, P. Chen, W. Chen, C. Hsu, K. Tsai, M. Tsai, P. Wang, *Langmuir* **2017**, 33, 4654.
- [90] M. Terai, Y. Sakotsubo, S. Kotsuji, H. Hada, *IEEE Electron. Device Lett.* **2010**, 31, 204.
- [91] Y. Wu, B. Lee, H. P. Wong, *IEEE Electron. Device Lett.* **2010**, 31, 1449.
- [92] K. Lin, T. Hou, J. Shieh, J. Lin, C. Chou, Y. Lee, *J. Appl. Phys.* **2011**, 109, 084104.
- [93] S. Privitera, G. Bersuker, S. Lombardo, C. Bongiorno, D. C. Gilmer, *Solid State Electron.* **2015**, 111, 161.
- [94] W. Wu, H. Wu, B. Gao, P. Yao, X. Zhang, X. Peng, S. Yu, H. Qian, in *2018 IEEE Symp. on VLSI Technol.*, IEEE, Honolulu, HI **2018**, pp. 103–104.
- [95] C. Lin, C. Wu, C. Wu, C. Hu, T. Tseng, *J. Electrochem. Soc.* **2007**, 154, G189.
- [96] C. Ho, E. K. Lai, M. D. Lee, C. L. Pan, Y. D. Yao, K. Y. Hsieh, R. Liu, C. Y. Lu, in *2007 IEEE Symp. on VLSI Technol.*, IEEE, Kyoto, JP **2007**, pp. 228–229.
- [97] W. G. Kim, J. Y. Kim, J. W. Moon, M. S. Joo, H. J. Choi, S. G. Kim, K. J. Lee, K. Hong, S. K. Park, in *2012 4th IEEE Int. Memory Workshop*, IEEE, Milan, ITL **2012**, pp. 1–4.
- [98] W. C. Chien, Y. R. Chen, Y. C. Chen, A. T. H. Chuang, F. M. Lee, Y. Y. Lin, E. K. Lai, Y. H. Shih, K. Y. Hsieh, C.-Y. Lu, in *2010 IEEE Int. Electron Devices Meeting (IEDM)*, IEEE, San Francisco, CA **2010**, 19.2.1.
- [99] K. S. Novoselov, A. K. Geim, S. V. Morozov, D. Jiang, Y. Zhang, S. V. Dubonos, I. V. Grigorieva, A. A. Firsov, *Science* **2004**, 306, 666.
- [100] A. C. Neto, F. Guinea, N. M. Peres, K. S. Novoselov, A. K. Geim, *Rev. Mod. Phys.* **2009**, 81, 109.
- [101] A. K. Geim, *Science* **2009**, 324, 1530.
- [102] A. K. Geim, I. V. Grigorieva, *Nature* **2013**, 499, 419.
- [103] W. Huh, S. Jang, J. Y. Lee, D. Lee, D. Lee, J. M. Lee, H.-G. Park, J. C. Kim, H. Y. Jeong, G. Wang, *Adv. Mater.* **2018**, 30, 1801447.
- [104] M. T. Sharbatli, Y. Du, J. Torres, N. D. Ardonino, M. Yun, F. Xiong, *Adv. Mater.* **2018**, 30, 1802353.
- [105] X. Zhuang, Y. Chen, G. Liu, P. Li, C. Zhu, E. Kang, K. Noeh, B. Zhang, J. Zhu, Y. Li, *Adv. Mater.* **2010**, 22, 1731.
- [106] C. Pan, Y. Ji, N. Xiao, F. Hui, K. Tang, Y. Guo, X. Xie, F. M. Puglisi, L. Larcher, E. Miranda, *Adv. Funct. Mater.* **2017**, 27, 1604811.
- [107] X. Wu, R. Ge, P. A. Chen, H. Chou, Z. Zhang, Y. Zhang, S. Banerjee, M. H. Chiang, J. C. Lee, D. Akinwande, *Adv. Mater.* **2019**, 31, 1806790.
- [108] C. Hao, F. Wen, J. Xiang, S. Yuan, B. Yang, L. Li, W. Wang, Z. Zeng, L. Wang, Z. Liu, *Adv. Funct. Mater.* **2016**, 26, 2016.
- [109] V. K. Sangwan, H. Lee, H. Bergeron, I. Balla, M. E. Beck, K. Chen, M. C. Hersam, *Nature* **2018**, 554, 500.
- [110] V. K. Sangwan, H. Lee, M. C. Hersam, in *2017 IEEE Int. Electron Devices Meeting (IEDM)*, IEEE, San Francisco, CA **2017**, 5.1.1.
- [111] M. Wang, S. Cai, C. Pan, C. Wang, X. Lian, Y. Zhuo, K. Xu, T. Cao, X. Pan, B. Wang, *Nat. Electron.* **2018**, 1, 130.
- [112] Y. Yang, J. Lee, S. Lee, C. H. Liu, Z. Zhong, W. Lu, *Adv. Mater.* **2014**, 26, 3693.
- [113] V. K. Sangwan, D. Jariwala, I. S. Kim, K. S. Chen, T. J. Marks, L. J. Lauhon, M. C. Hersam, *Nat. Nanotechnol.* **2015**, 10, 403.
- [114] A. A. Bessonov, M. N. Kirikova, D. I. Petukhov, M. Allen, T. Ryhänen, M. J. Bailey, *Nat. Mater.* **2015**, 14, 199.

- [115] X. Yan, K. Wang, J. Zhao, Z. Zhou, H. Wang, J. Wang, L. Zhang, X. Li, Z. Xiao, Q. Zhao, *Small* **2019**, *15*, 1900107.
- [116] X. Yan, Q. Zhao, A. P. Chen, J. Zhao, Z. Zhou, J. Wang, H. Wang, L. Zhang, X. Li, Z. Xiao, *Small* **2019**, *15*, 1901423.
- [117] C. Tan, Z. Liu, W. Huang, H. Zhang, *Chem. Soc. Rev.* **2015**, *44*, 2615.
- [118] F. Zhang, H. Zhang, S. Krylyuk, C. A. Milligan, Y. Zhu, D. Y. Zemlyanov, L. A. Bendersky, B. P. Burton, A. V. Davydov, J. Appenzeller, *Nat. Mater.* **2019**, *18*, 55.
- [119] J. V. Lauritsen, J. Kibsgaard, S. Helveg, H. Topsøe, B. S. Clausen, E. Laegsgaard, F. Besenbacher, *Nat. Nanotechnol.* **2007**, *2*, 53.
- [120] P. Miró, M. Audiffred, T. Heine, *Chem. Soc. Rev.* **2014**, *43*, 6537.
- [121] V. Garcia, S. Fusil, K. Bouzehouane, S. Enouz-Vedrenne, N. D. Mathur, A. Barthélémy, M. Bibes, *Nature* **2009**, *460*, 81.
- [122] P. Maksymovych, S. Jesse, P. Yu, R. Ramesh, A. P. Baddorf, S. V. Kalinin, *Science* **2009**, *324*, 1421.
- [123] A. Gruverman, D. Wu, H. Lu, Y. Wang, H. W. Jang, C. M. Folkman, M. Y. Zhuravlev, D. Felker, M. Rzchowski, C. Eom, *Nano Lett.* **2009**, *9*, 3539.
- [124] H. Y. Yoong, H. Wu, J. Zhao, H. Wang, R. Guo, J. Xiao, B. Zhang, P. Yang, S. J. Pennycook, N. Deng, *Adv. Funct. Mater.* **2018**, *28*, 1806037.
- [125] Z. Yan, Y. Guo, G. Zhang, J. M. Liu, *Adv. Mater.* **2011**, *23*, 1351.
- [126] A. Chanthbouala, V. Garcia, R. O. Cherif, K. Bouzehouane, S. Fusil, X. Moya, S. Xavier, H. Yamada, C. Deranlot, N. D. Mathur, *Nat. Mater.* **2012**, *11*, 860.
- [127] H. Yamada, V. Garcia, S. Fusil, S. Boyn, M. Marinova, A. Gloter, S. Xavier, J. Grollier, E. Jacquet, C. Carretero, *ACS Nano* **2013**, *7*, 5385.
- [128] D. Pantel, H. Lu, S. Goetze, P. Werner, D. Jik Kim, A. Gruverman, D. Hesse, M. Alexe, *Appl. Phys. Lett.* **2012**, *100*, 232902.
- [129] M. Hambe, A. Petraru, N. A. Pertsev, P. Munroe, V. Nagarajan, H. Kohlstedt, *Adv. Funct. Mater.* **2010**, *20*, 2436.
- [130] Z. Wen, C. Li, D. Wu, A. Li, N. Ming, *Nat. Mater.* **2013**, *12*, 617.
- [131] Z. Xiao, J. Zhao, C. Lu, Z. Zhou, H. Wang, L. Zhang, J. Wang, X. Li, K. Wang, Q. Zhao, *Appl. Phys. Lett.* **2018**, *113*, 223501.
- [132] S. Choi, G. Park, K. Kim, S. Cho, W. Yang, X. Li, J. Moon, K. Lee, K. Kim, *Adv. Mater.* **2011**, *23*, 3272.
- [133] P. Boolchand, W. J. Bresser, *Nature* **2001**, *410*, 1070.
- [134] I. Valov, I. Sapozhnskaia, A. Nayak, T. Tsuruoka, T. Bredow, T. Hasegawa, G. Staikov, M. Aono, R. Waser, *Nat. Mater.* **2012**, *11*, 530.
- [135] V. Dubost, T. Cren, C. Vaju, L. Cario, B. Corraze, E. Janod, F. Debontridder, D. Roditchev, *Nano Lett.* **2013**, *13*, 3648.
- [136] Y. Hirose, H. Hirose, *J. Appl. Phys.* **1976**, *47*, 2767.
- [137] K. Terabe, T. Hasegawa, T. Nakayama, M. Aono, *Nature* **2005**, *433*, 47.
- [138] T. Tamura, T. Hasegawa, K. Terabe, T. Nakayama, T. Sakamoto, H. Sunamura, H. Kawaura, S. Hosaka, M. Aono, *JPN J. Appl. Phys.* **2006**, *45*, L364.
- [139] J. Jang, F. Pan, K. Braam, V. Subramanian, *Adv. Mater.* **2012**, *24*, 3573.
- [140] S. Kaeriyama, T. Sakamoto, H. Sunamura, M. Mizuno, H. Kawaura, T. Hasegawa, K. Terabe, T. Nakayama, M. Aono, *IEEE J. Solid-State Circuits* **2005**, *40*, 168.
- [141] D. Deleruyelle, C. Muller, J. Amouroux, R. Müller, *Appl. Phys. Lett.* **2010**, *96*, 263504.
- [142] Y. Yan, C. P. Yang, K. Bärner, V. V. Marchenkova, Y. Zeng, *Appl. Surf. Sci.* **2016**, *360*, 875.
- [143] D. C. Worledge, G. Hu, D. W. Abraham, J. Z. Sun, P. L. Trouilloud, J. Nowak, S. Brown, M. C. Gaidis, E. J. O. Sullivan, R. P. Robertazzi, *Appl. Phys. Lett.* **2011**, *98*, 022501.
- [144] R. Guo, W. Lin, X. Yan, T. Venkatesan, J. Chen, *Appl. Phys. Rev.* **2020**, *7*, 011304.
- [145] H. Wang, X. Yan, *Phys. Status Solidi RRL* **2019**, *13*, 1900073.
- [146] T. Fujii, M. Kawasaki, A. Sawa, H. Akoh, Y. Kawazoe, Y. Tokura, *Appl. Phys. Lett.* **2005**, *86*, 012107.
- [147] M. Lee, C. B. Lee, D. Lee, S. R. Lee, M. Chang, J. H. Hur, Y. Kim, C. Kim, D. H. Seo, S. Seo, *Nat. Mater.* **2011**, *10*, 625.
- [148] B. Cho, S. Song, Y. Ji, T. W. Kim, T. Lee, *Adv. Funct. Mater.* **2011**, *21*, 2806.
- [149] C. Lin, S. Wang, D. Lee, T. Tseng, *J. Electrochem. Soc.* **2008**, *155*, H615.
- [150] H. Kim, H. An, E. B. Lee, T. G. Kim, *IEEE Trans. Electron. Devices* **2011**, *58*, 3566.
- [151] Q. Liu, W. Guan, S. Long, R. Jia, M. Liu, J. Chen, *Appl. Phys. Lett.* **2008**, *92*, 012117.
- [152] K. Kinoshita, T. Tamura, M. Aoki, Y. Sugiyama, H. Tanaka, *Appl. Phys. Lett.* **2006**, *89*, 103509.
- [153] G. Agrawal, R. Agrawal, *ACS Appl. Nano Mater.* **2019**, *2*, 1738.
- [154] D. Lee, H. Choi, H. Sim, D. Choi, H. Hwang, M. Lee, S. Seo, I. K. Yoo, *IEEE Electron. Device Lett.* **2005**, *26*, 719.
- [155] Z. Wang, H. Wu, G. W. Burr, C. S. Hwang, K. L. Wang, Q. Xia, J. J. Yang, *Nat. Rev. Mater.* **2020**, *5*, 173.
- [156] K. Szot, W. Speier, G. Bihlmayer, R. Waser, *Nat. Mater.* **2006**, *5*, 312.
- [157] X. Yan, J. Zhao, S. Liu, Z. Zhou, Q. Liu, J. Chen, X. Y. Liu, *Adv. Funct. Mater.* **2018**, *28*, 1705320.
- [158] Y. Xing, C. Shi, J. Zhao, W. Qiu, N. Lin, J. Wang, X. B. Yan, W. D. Yu, X. Y. Liu, *Small* **2017**, *13*, 1702390.
- [159] X. A. Tran, W. Zhu, W. J. Liu, Y. C. Yeo, B. Y. Nguyen, H. Y. Yu, *IEEE Trans. Electron. Dev.* **2012**, *60*, 391.
- [160] X. Yan, Z. Zhou, J. Zhao, Q. Liu, H. Wang, G. Yuan, J. Chen, *Nano Res.* **2018**, *11*, 1183.
- [161] W. Shen, R. Dittmann, R. Waser, *J. Appl. Phys.* **2010**, *107*, 094506.
- [162] Y. Yang, P. Gao, S. Gaba, T. Chang, X. Pan, W. Lu, *Nat. Commun.* **2012**, *3*, 732.
- [163] I. Valov, R. Waser, J. R. Jameson, M. N. Kozicki, *Nanotechnology* **2011**, *22*, 254003.
- [164] I. Valov, M. N. Kozicki, *J. Phys. D: Appl. Phys.* **2013**, *46*, 074005.
- [165] C. Schindler, G. Staikov, R. Waser, *Appl. Phys. Lett.* **2009**, *94*, 072109.
- [166] Y. Wang, Q. Liu, S. Long, W. Wang, Q. Wang, M. Zhang, S. Zhang, Y. Li, Q. Zuo, J. Yang, *Nanotechnology* **2010**, *21*, 045202.
- [167] M. Zhang, S. Long, G. Wang, X. Xu, Y. Li, Q. Liu, H. Lv, X. Lian, E. Miranda, J. Suñé, *Appl. Phys. Lett.* **2014**, *105*, 193501.
- [168] Q. Liu, J. Sun, H. Lv, S. Long, K. Yin, N. Wan, Y. Li, L. Sun, M. Liu, *Adv. Mater.* **2012**, *24*, 1844.
- [169] Y. C. Yang, F. Pan, Q. Liu, M. Liu, F. Zeng, *Nano Lett.* **2009**, *9*, 1636.
- [170] S. Peng, F. Zhuge, X. Chen, X. Zhu, B. Hu, L. Pan, B. Chen, R. Li, *Appl. Phys. Lett.* **2012**, *100*, 072101.
- [171] R. Waser, R. Dittmann, G. Staikov, K. Szot, *Adv. Mater.* **2009**, *21*, 2632.
- [172] D. Kwon, K. M. Kim, J. H. Jang, J. M. Jeon, M. H. Lee, G. H. Kim, X. Li, G. Park, B. Lee, S. Han, *Nat. Nanotechnol.* **2010**, *5*, 148.
- [173] J. Chen, C. Hsin, C. Huang, C. Chiu, Y. Huang, S. Lin, W. Wu, L. Chen, *Nano Lett.* **2013**, *13*, 3671.
- [174] B. J. Choi, D. S. Jeong, S. K. Kim, C. Rohde, S. Choi, J. H. Oh, H. J. Kim, C. S. Hwang, K. Szot, R. Waser, *J. Appl. Phys.* **2005**, *98*, 033715.
- [175] C. Kang, W. Kuo, W. Bao, C. Ho, C. Huang, W. Wu, Y. Chu, J. Juang, S. H. Tseng, L. Hu, *Nano Energy* **2015**, *13*, 283.
- [176] S. Long, L. Perniola, C. Cagli, J. Buckley, X. Lian, E. Miranda, F. Pan, M. Liu, J. Suné, *Sci. Rep.* **2013**, *3*, 1.
- [177] J. J. Yang, M. Zhang, J. P. Strachan, F. Miao, M. D. Pickett, R. D. Kelley, G. Medeiros-Ribeiro, R. S. Williams, *Appl. Phys. Lett.* **2010**, *97*, 232102.
- [178] J. Lee, W. D. Lu, *Adv. Mater.* **2018**, *30*, 1702770.
- [179] R. Waser, M. Aono, in *Nanoscience And Technology: A Collection of Reviews from Nature Journals*, World Scientific, Singapore **2010**, p. 158.
- [180] W. Lee, J. Park, S. Kim, J. Woo, J. Shin, G. Choi, S. Park, D. Lee, E. Cha, B. H. Lee, *ACS Nano* **2012**, *6*, 8166.
- [181] K. M. Kim, S. R. Lee, S. Kim, M. Chang, C. S. Hwang, *Adv. Funct. Mater.* **2015**, *25*, 1527.
- [182] J. Y. Chen, C. W. Huang, C. H. Chiu, Y. T. Huang, W. W. Wu, *Adv. Mater.* **2015**, *27*, 5028.

- [183] S. Raoux, W. Wełnic, D. Ielmini, *Chem. Rev.* **2010**, *110*, 240.
- [184] S. B. Eryilmaz, E. Neftci, S. Joshi, S. Kim, M. BrightSky, H. Lung, C. Lam, G. Cauwenberghs, H. P. Wong, *IEEE Trans. Electron. Devices* **2016**, *63*, 5004.
- [185] T. Tuma, A. Pantazi, M. Le Gallo, A. Sebastian, E. Eleftheriou, *Nat. Nanotechnol.* **2016**, *11*, 693.
- [186] D. Kuzum, R. G. Jeyasingh, B. Lee, H. P. Wong, *Nano Lett.* **2012**, *12*, 2179.
- [187] S. R. Ovshinsky, *Phys. Rev. Lett.* **1968**, *21*, 1450.
- [188] H. Sun, Q. Liu, C. Li, S. Long, H. Lv, C. Bi, Z. Huo, L. Li, M. Liu, *Adv. Funct. Mater.* **2014**, *24*, 5679.
- [189] S. H. Chang, J. S. Lee, S. C. Chae, S. B. Lee, C. Liu, B. Kahng, D. Kim, T. W. Noh, *Phys. Rev. Lett.* **2009**, *102*, 26801.
- [190] H. Y. Peng, Y. F. Li, W. N. Lin, Y. Z. Wang, X. Y. Gao, T. Wu, *Sci. Rep.* **2012**, *2*, 442.
- [191] U. Russo, D. Ielmini, C. Cagli, A. L. Lacaita, *IEEE Trans. Electron. Devices* **2009**, *56*, 186.
- [192] R. Midya, Z. Wang, J. Zhang, S. E. Savel'Ev, C. Li, M. Rao, M. H. Jang, S. Joshi, H. Jiang, P. Lin, *Adv. Mater.* **2017**, *29*, 1604457.
- [193] E. Linn, R. Rosezin, C. Kügeler, R. Waser, *Nat. Mater.* **2010**, *9*, 403.
- [194] Z. Wang, M. Rao, R. Midya, S. Joshi, H. Jiang, P. Lin, W. Song, S. Asapu, Y. Zhuo, C. Li, *Adv. Funct. Mater.* **2018**, *28*, 1704862.
- [195] A. J. Arnold, A. Razavieh, J. R. Nasr, D. S. Schulman, C. M. Eichfeld, S. Das, *ACS Nano* **2017**, *11*, 3110.
- [196] E. G. Gray, *J. Anat.* **1959**, *93*, 420.
- [197] G. F. Striedter, *Neurobiology: A Functional Approach*, Oxford University Press, Oxford **2016**.
- [198] H. Tian, Q. Guo, Y. Xie, H. Zhao, C. Li, J. J. Cha, F. Xia, H. Wang, *Adv. Mater.* **2016**, *28*, 4991.
- [199] Y. van de Burgt, E. Lubberman, E. J. Fuller, S. T. Keene, G. C. Faria, S. Agarwal, M. J. Marinella, A. A. Talin, A. Salleo, *Nat. Mater.* **2017**, *16*, 414.
- [200] Y. H. Liu, L. Q. Zhu, P. Feng, Y. Shi, Q. Wan, *Adv. Mater.* **2015**, *27*, 5599.
- [201] S. Kim, B. Choi, M. Lim, J. Yoon, J. Lee, H. Kim, S. Choi, *ACS Nano* **2017**, *11*, 2814.
- [202] L. Q. Zhu, C. J. Wan, L. Q. Guo, Y. Shi, Q. Wan, *Nat. Commun.* **2014**, *5*, 3158.
- [203] L. Q. Zhu, C. J. Wan, P. Q. Gao, Y. H. Liu, H. Xiao, J. C. Ye, Q. Wan, *ACS Appl. Mater. Interfaces* **2016**, *8*, 21770.
- [204] S. J. Martin, P. D. Grimwood, R. G. Morris, *Annu. Rev. Neurosci.* **2000**, *23*, 649.
- [205] T. V. Bliss, G. L. Collingridge, *Nature* **1993**, *361*, 31.
- [206] D. M. Bannerman, R. Sprengel, D. J. Sanderson, S. B. McHugh, J. N. P. Rawlins, H. Monyer, P. H. Seuberg, *Nat. Rev. Neurosci.* **2014**, *15*, 181.
- [207] G. Indiveri, B. Linares-Barranco, R. Legenstein, G. Deligeorgis, T. Prodromakis, *Nanotechnology* **2013**, *24*, 384010.
- [208] J. J. Yang, D. B. Strukov, D. R. Stewart, *Nat. Nanotechnol.* **2013**, *8*, 13.
- [209] D. O. Hebb, *The Organization of Behavior: A Neuropsychological Theory*, Wiley, New York **1949**.
- [210] G. S. Snider, in *2008 IEEE Int. Symp. on Nanoscale Architectures*, IEEE, Anaheim, CA **2008**, pp. 85–92.
- [211] B. Linares-Barranco, T. Serrano-Gotarredona, *Nat. Preced.* **2009**, <https://doi.org/10.1038/npre.2009.3010.1>.
- [212] B. Linares-Barranco, T. Serrano-Gotarredona, L. A. Camuñas-Mesa, J. A. Pérez-Carrasco, C. Zamarreño-Ramos, T. Masquelier, *Front. Neurosci.* **2011**, *5*, 26.
- [213] T. Serrano-Gotarredona, T. Masquelier, T. Prodromakis, G. Indiveri, B. Linares-Barranco, *Front. Neurosci.* **2013**, *7*, 2.
- [214] O. Bichler, D. Querlioz, S. J. Thorpe, J. Bourgoin, C. Gamrat, *Neural Networks* **2012**, *32*, 339.
- [215] S. Yu, Y. Wu, R. Jeyasingh, D. Kuzum, H. P. Wong, *IEEE Trans. Electron. Devices* **2011**, *58*, 2729.
- [216] O. Bichler, M. Suri, D. Querlioz, D. Vuillaume, B. DeSalvo, C. Gamrat, *IEEE Trans. Electron. Devices* **2012**, *59*, 2206.
- [217] W. Gerstner, R. Ritz, J. L. Van Hemmen, *Biol. Cybern.* **1993**, *69*, 503.
- [218] J. Sjöström, W. Gerstner, *Scholarpedia* **2010**, *5*, 1362.
- [219] A. Delorme, L. Perrinet, S. J. Thorpe, *Neurocomputing* **2001**, *38–40*, 539.
- [220] T. Masquelier, R. Guyonneau, S. J. Thorpe, *Neural Comput.* **2009**, *21*, 1259.
- [221] M. J. Breitwisch, R. W. Cheek, C. H. Lam, D. S. Modha, B. Rajendran, *U.S. Patent No. 8,447,714*, **2013**.
- [222] G. Bi, M. Poo, *Annu. Rev. Neurosci.* **2001**, *24*, 139.
- [223] Z. Lv, Y. Zhou, S. Han, V. Roy, *Mater. Today* **2018**, *21*, 537.
- [224] R. Hanajima, Y. Ugawa, Y. Terao, K. Sakai, T. Furabayashi, K. Machii, I. Kanazawa, *J. Physiol.* **1998**, *509*, 607.
- [225] Z. Wang, S. Joshi, S. E. Savel'ev, H. Jiang, R. Midya, P. Lin, M. Hu, N. Ge, J. P. Strachan, Z. Li, *Nat. Mater.* **2017**, *16*, 101.
- [226] R. S. Zucker, W. G. Regehr, *Annu. Rev. Physiol.* **2002**, *64*, 355.
- [227] L. Feng, P. Molnár, J. V. Nadler, *J. Neurosci.* **2003**, *23*, 5381.
- [228] R. M. Mulkey, C. E. Herron, R. C. Malenka, *Science* **1993**, *261*, 1051.
- [229] M. Cassinero, N. Ciocchini, D. Ielmini, *Adv. Mater.* **2013**, *25*, 5975.
- [230] M. Suri, O. Bichler, D. Querlioz, O. Cueto, L. Perniola, V. Sousa, D. Vuillaume, C. Gamrat, B. DeSalvo, in *2011 IEEE Int. Electron Devices Meeting (IEDM)*, IEEE, Washington, DC **2011**, 4.1.1.
- [231] W. Zhang, R. Mazzarello, M. Wuttig, E. Ma, *Nat. Rev. Mater.* **2019**, *4*, 150.
- [232] H. Tan, G. Liu, X. Zhu, H. Yang, B. Chen, X. Chen, J. Shang, W. D. Lu, Y. Wu, R. Li, *Adv. Mater.* **2015**, *27*, 2797.
- [233] H. Tan, G. Liu, H. Yang, X. Yi, L. Pan, J. Shang, S. Long, M. Liu, Y. Wu, R. Li, *ACS Nano* **2017**, *11*, 11298.
- [234] S. Wang, C. Chen, Z. Yu, Y. He, X. Chen, Q. Wan, Y. Shi, D. W. Zhang, H. Zhou, X. Wang, *Adv. Mater.* **2019**, *31*, 1806227.
- [235] H. Wang, Q. Zhao, Z. Ni, Q. Li, H. Liu, Y. Yang, L. Wang, Y. Ran, Y. Guo, W. Hu, *Adv. Mater.* **2018**, *30*, 1803961.
- [236] S. Nau, C. Wolf, S. Sax, E. J. List-Kratochvil, *Adv. Mater.* **2015**, *27*, 1048.
- [237] H. Wang, H. Liu, Q. Zhao, Z. Ni, Y. Zou, J. Yang, L. Wang, Y. Sun, Y. Guo, W. Hu, *Adv. Mater.* **2017**, *29*, 1701772.
- [238] S. Chen, Z. Lou, D. Chen, G. Shen, *Adv. Mater.* **2018**, *30*, 1705400.
- [239] M. Lee, W. Lee, S. Choi, J. Jo, J. Kim, S. K. Park, Y. Kim, *Adv. Mater.* **2017**, *29*, 1700951.
- [240] R. C. Atkinson, R. M. Shiffrin, *Psychol. Learn. Motiv. - Adv. Res. Theory* **1968**, *2*, 89.
- [241] Z. Q. Wang, H. Y. Xu, X. H. Li, H. Yu, Y. C. Liu, X. J. Zhu, *Adv. Funct. Mater.* **2012**, *22*, 2759.
- [242] G. Liu, C. Wang, W. Zhang, L. Pan, C. Zhang, X. Yang, F. Fan, Y. Chen, R. Li, *Adv. Electron. Mater.* **2016**, *2*, 1500298.
- [243] S. Gao, G. Liu, H. Yang, C. Hu, Q. Chen, G. Gong, W. Xue, X. Yi, J. Shang, R. Li, *ACS Nano* **2019**, *13*, 2634.
- [244] Y. Wang, Z. Lv, J. Chen, Z. Wang, Y. Zhou, L. Zhou, X. Chen, S. Han, *Adv. Mater.* **2018**, *30*, 1802883.
- [245] P. M. Sheridan, F. Cai, C. Du, W. Ma, Z. Zhang, W. D. Lu, *Nat. Nanotechnol.* **2017**, *12*, 784.
- [246] D. H. Hubel, T. N. Wiesel, *J. Physiol.* **1962**, *160*, 106.
- [247] K. Fukushima, *Biol. Cybern.* **1980**, *36*, 193.
- [248] P. Yao, H. Wu, B. Gao, J. Tang, Q. Zhang, W. Zhang, J. J. Yang, H. Qian, *Nature* **2020**, *577*, 641.
- [249] Z. Wang, C. Li, P. Lin, M. Rao, Y. Nie, W. Song, Q. Qiu, Y. Li, P. Yan, J. P. Strachan, *Nat. Mach. Intell.* **2019**, *1*, 434.
- [250] C. M. Bishop, *Neural Networks for Pattern Recognition*, Oxford University Press, Oxford **1995**.
- [251] Z. Wang, S. Joshi, S. Savel'ev, W. Song, R. Midya, Y. Li, M. Rao, P. Yan, S. Asapu, Y. Zhuo, *Nat. Electron.* **2018**, *1*, 137.
- [252] H. D. Beale, H. B. Demuth, M. T. Hagan, *Neural Network Design*, PWS Publishing Company, Boston **1996**.
- [253] M. Hu, C. E. Graves, C. Li, Y. Li, N. Ge, E. Montgomery, N. Davila, H. Jiang, R. S. Williams, J. J. Yang, *Adv. Mater.* **2018**, *30*, 1705914.
- [254] D. Silver, A. Huang, C. J. Maddison, A. Guez, L. Sifre, G. Van Den Driessche, J. Schrittwieser, I. Antonoglou, V. Panneershelvam, M. Lanctot, *Nature* **2016**, *529*, 484.

- [255] W. Maass, *Neural Networks* **1997**, *10*, 1659.
- [256] A. L. Hodgkin, A. F. Huxley, *J. Physiol.* **1952**, *117*, 500.
- [257] E. M. Izhikevich, *IEEE Trans. Neural Networks* **2004**, *15*, 1063.
- [258] W. Gerstner, W. M. Kistler, *Spiking Neuron Models: Single Neurons, Populations, Plasticity*, Cambridge University Press, Cambridge **2002**.
- [259] A. Grüning, S. M. Bohte, presented at *Proc. of the 22nd European Symp. on Artificial Neural Networks (ESANN 2014)*, ESANN, Bruges **2014**.
- [260] W. Yi, K. K. Tsang, S. K. Lam, X. Bai, J. A. Crowell, E. A. Flores, *Nat. Commun.* **2018**, *9*, 1.
- [261] B. Widrow, M. E. Hoff, *Adaptive Switching Circuits*, Stanford Univ Ca Stanford Electronics Labs, Stanford, CA **1960**.
- [262] R. Urbanczik, W. Senn, *Neural Comput.* **2009**, *21*, 340.
- [263] J. J. Wade, L. J. McDaid, J. A. Santos, H. M. Sayers, *IEEE Trans. Neural Networks* **2010**, *21*, 1817.
- [264] T. Natschläger, B. Ruf, *Netw. Comput. Neural Syst.* **1998**, *9*, 319.
- [265] S. M. Bohte, J. N. Kok, H. La Poutre, *Neurocomputing* **2002**, *48*, 17.
- [266] R. V. Florian, *PLoS One* **2012**, *7*, e40233.
- [267] R. Urbanczik, W. Senn, *Nat. Neurosci.* **2009**, *12*, 250.
- [268] S. Thorpe, J. Gauthrais, *Comput. Neurosci.* **1998**, *113*.
- [269] E. M. Izhikevich, *Neural Comput.* **2006**, *18*, 245.
- [270] O. Marre, D. Amodei, N. Deshmukh, K. Sadeghi, F. Soo, T. E. Holy, M. J. Berry, *J. Neurosci.* **2012**, *32*, 14859.
- [271] S. M. Bohte, in *26th Conference on Neural Information Processing Systems*, NeurIPS, Harrahs and Harveys, Lake Tahoe **2012**, p. 1835.
- [272] S. M. Bohte, in *International Conference on Artificial Neural Networks*, Springer, Berlin, Heidelberg **2011**, p. 60.
- [273] W. J. Ma, J. M. Beck, P. E. Latham, A. Pouget, *Nat. Neurosci.* **2006**, *9*, 1432.
- [274] M. Boerlin, S. Denève, *PLoS Comput. Biol.* **2011**, *7*, e1001080.
- [275] J. J. Hopfield, *Proc. Natl. Acad. Sci. USA* **1982**, *79*, 2554.
- [276] V. T. Pham, S. Jafari, S. Vaideyanathan, C. Volos, X. Wang, *Sci. China Technol. Sci.* **2016**, *59*, 358.
- [277] J. Zhang, X. Jin, *Neural Networks* **2000**, *13*, 745.
- [278] J. J. Hopfield, *Proc. Natl. Acad. Sci. USA* **1984**, *81*, 3088.
- [279] J. J. Hopfield, D. W. Tank, *Science* **1986**, *233*, 625.
- [280] J. J. Hopfield, D. W. Tank, *Biol. Cybern.* **1985**, *52*, 141.
- [281] O. Lázaro, D. Girma, *IEEE Trans. Veh. Technol.* **2000**, *49*, 1578.
- [282] M. Verleysen, B. Sirletti, A. Vandemeulebroecke, P. G. Jespers, *IEEE Trans. Circuits Syst.* **1989**, *36*, 762.
- [283] R. E. Howard, D. B. Schwartz, J. S. Denker, R. W. Epworth, H. P. Graf, W. E. Hubbard, L. D. Jackel, B. L. Straughn, D. M. Tenant, *IEEE Trans. Electron. Devices* **1987**, *34*, 1553.
- [284] S. Duan, Z. Dong, X. Hu, L. Wang, H. Li, *Neural. Comput. Appl.* **2016**, *27*, 837.
- [285] S. Kumar, J. P. Strachan, R. S. Williams, *Nature* **2017**, *548*, 318.
- [286] S. G. Hu, Y. Liu, Z. Liu, T. P. Chen, J. J. Wang, Q. Yu, L. J. Deng, Y. Yin, S. Hosaka, *Nat. Commun.* **2015**, *6*, 1.
- [287] J. Yang, L. Wang, Y. Wang, T. Guo, *Neurocomputing* **2017**, *227*, 142.
- [288] R. Midya, Z. Wang, S. Asapu, S. Joshi, Y. Li, Y. Zhuo, W. Song, H. Jiang, N. Upadhyay, M. Rao, *Adv. Electron. Mater.* **2019**, *5*, 1900060.
- [289] X. Zhang, Z. Wang, W. Song, R. Midya, Y. Zhuo, R. Wang, M. Rao, N. K. Upadhyay, Q. Xia, J. J. Yang, Q. Liu, M. Liu, in *2019 IEEE Int. Electron Devices Meeting (IEDM)*, IEEE, San Francisco, CA **2019**, 6.7.1.
- [290] G. Zhang, J. Ma, A. Alsaedi, B. Ahmad, F. Alzahrani, *Appl. Math. Comput.* **2018**, *321*, 290.
- [291] M. Itoh, L. O. Chua, *Int. J. Bifurcation Chaos Appl. Sci. Eng.* **2008**, *18*, 3183.
- [292] Z. Sun, E. Ambrosi, A. Bricallli, D. Ielmini, *Adv. Mater.* **2018**, *30*, 1802554.
- [293] A. Garg, J. N. Onuchic, V. Ambegaokar, *J. Chem. Phys.* **1985**, *83*, 4491.
- [294] H. Wang, Y. Du, Y. Li, B. Zhu, W. R. Leow, Y. Li, J. Pan, T. Wu, X. Chen, *Adv. Funct. Mater.* **2015**, *25*, 3825.
- [295] H. Wang, B. Zhu, X. Ma, Y. Hao, X. Chen, *Small* **2016**, *12*, 2715.
- [296] N. Raeis Hosseini, J. Lee, *ACS Nano* **2015**, *9*, 419.
- [297] C. Wu, T. W. Kim, T. Guo, F. Li, D. U. Lee, J. J. Yang, *Adv. Mater.* **2017**, *29*, 1602890.
- [298] Z. Tan, X. Yin, R. Yang, S. Mi, C. Jia, X. Guo, *Sci. Rep.* **2017**, *7*, 1.
- [299] R. A. John, N. Tiwari, C. Yaoyi, N. T. Ankit, M. Kulkarni, A. Nirmal, A. C. Nguyen, A. Basu, N. Mathews, *ACS Nano* **2018**, *12*, 11263.
- [300] M. Kumar, H. Kim, J. Kim, *Adv. Mater.* **2019**, *31*, 1900021.
- [301] Y. Kim, Y. J. Kwon, D. E. Kwon, K. J. Yoon, J. H. Yoon, S. Yoo, H. J. Kim, T. H. Park, J. Han, K. M. Kim, *Adv. Mater.* **2018**, *30*, 1704320.
- [302] Y. Zang, H. Shen, D. Huang, C. Di, D. Zhu, *Adv. Mater.* **2017**, *29*, 1606088.
- [303] C. Wang, S. Liang, S. Wang, P. Wang, Z. Li, Z. Wang, A. Gao, C. Pan, C. Liu, J. Liu, H. Yang, X. Liu, W. Song, C. Wang, X. Wang, K. Chen, Z. Wang, K. Watanabe, T. Taniguchi, J. J. Yang, F. Miao, *Sci. Adv.* **2020**, *6*, eaba6173.
- [304] B. C. Jang, S. Kim, S. Y. Yang, J. Park, J. Cha, J. Oh, J. Choi, S. G. Im, V. P. Dravid, S. Choi, *Nano Lett.* **2019**, *19*, 839.
- [305] S. Choi, S. H. Tan, Z. Li, Y. Kim, C. Choi, P. Chen, H. Yeon, S. Yu, J. Kim, *Nat. Mater.* **2018**, *17*, 335.
- [306] M. A. Lastras-Montaño, K. Cheng, *Nat. Electron.* **2018**, *1*, 466.
- [307] F. Alibart, L. Gao, B. D. Hoskins, D. B. Strukov, *Nanotechnology* **2012**, *23*, 075201.
- [308] S. Ambrogio, P. Narayanan, H. Tsai, R. M. Shelby, I. Boybat, C. di Nolfo, S. Sidler, M. Giordano, M. Bodini, N. C. Farinha, *Nature* **2018**, *558*, 60.
- [309] C. Li, D. Belkin, Y. Li, P. Yan, M. Hu, N. Ge, H. Jiang, E. Montgomery, P. Lin, Z. Wang, *Nat. Commun.* **2018**, *9*, 1.
- [310] A. Shafee, A. Nag, N. Muralimanohar, R. Balasubramonian, J. P. Strachan, M. Hu, R. S. Williams, V. Srikumar, *Proc. ISCA* **2016**, *44*, 14.
- [311] H. Jiang, K. Yamada, Z. Ren, T. Kwok, F. Luo, Q. Yang, X. Zhang, J. J. Yang, Q. Xia, Y. Chen, in *2018 IEEE Int. Symp. on Circuits and Systems (ISCAS)*, IEEE, Florence, ITL **2018**, pp. 1–4.
- [312] T. Gokmen, Y. Vlasov, *Front. Neurosci.* **2016**, *10*, 333.
- [313] J. Woo, S. Yu, *IEEE Nanotechnol. Mag.* **2018**, *12*, 36.
- [314] G. W. Burr, R. M. Shelby, S. Sidler, C. Di Nolfo, J. Jang, I. Boybat, R. S. Shenoy, P. Narayanan, K. Virwani, E. U. Giacometti, *IEEE Trans. Electron. Devices* **2015**, *62*, 3498.
- [315] C. Li, Z. Wang, M. Rao, D. Belkin, W. Song, H. Jiang, P. Yan, Y. Li, P. Lin, M. Hu, *Nat. Mach. Intell.* **2019**, *1*, 49.
- [316] B. Yan, Q. Yang, W. Chen, K. Chang, J. Su, C. Hsu, S. Li, H. Lee, S. Sheu, M. Ho, Q. Wu, M. Chang, Y. Chen, H. Li, in *2019 Symp. on VLSI Technology*, IEEE, Kyoto, JP **2019**, pp. T86–T87.
- [317] C. Xue, W. Chen, J. Liu, J. Li, W. Lin, W. Lin, J. Wang, W. Wei, T. Chang, T. Chang, T. Huang, H. Kao, S. Wei, Y. Chiu, C. Lee, C. Lo, Y. King, C. Lin, R. Liu, C. Hsieh, K. Tang, M. Chang, in *2019 IEEE Int. Solid-State Circuits Conf. (ISSCC)*, IEEE, San Francisco, CA **2019**, pp. 388–390.
- [318] L. Wang, D. Wen, *Sci. Rep.* **2017**, *7*, 1.
- [319] Y. Park, J. Lee, *ACS Nano* **2017**, *11*, 8962.
- [320] Y. Chen, H. Yu, C. Huang, W. Chung, S. Wu, Y. Su, *Sci. Rep.* **2015**, *5*, 10022.
- [321] Y. Li, L. Xu, Y. Zhong, Y. Zhou, S. Zhong, Y. Hu, L. O. Chua, X. Miao, *Adv. Electron. Mater.* **2015**, *1*, 1500125.
- [322] M. D. Pickett, G. Medeiros-Ribeiro, R. S. Williams, *Nat. Mater.* **2013**, *12*, 114.
- [323] F. Zhou, Z. Zhou, J. Chen, T. H. Choy, J. Wang, N. Zhang, Z. Lin, S. Yu, J. Kang, H. P. Wong, Y. Chai, *Nat. Nanotechnol.* **2019**, *14*, 776.
- [324] F. Liu, C. Liu, preprint arXiv:1806.01775 **2018**.
- [325] Z. Dong, Y. Fang, L. Huang, J. Li, D. Qi, in *2019 Chinese Control and Decision Conf. (CCDC)*, IEEE, Nanchang, CN **2019**, pp. 3069–3074.
- [326] Q. Xia, J. J. Yang, *Nat. Mater.* **2019**, *18*, 309.
- [327] Y. Jeong, M. A. Zidan, W. D. Lu, *IEEE Trans. Nanotechnol.* **2017**, *17*, 184.

- [328] M. Prezioso, F. Merrikh-Bayat, B. D. Hoskins, G. C. Adam, K. K. Likharev, D. B. Strukov, *Nature* **2015**, *521*, 61.
- [329] P. Lin, C. Li, Z. Wang, Y. Li, H. Jiang, W. Song, M. Rao, Y. Zhuo, N. K. Upadhyay, M. Barnell, Q. Wu, J. J. Yang, Q. Xia, *Nat. Electron.* **2020**, *3*, 225.
- [330] T. Fu, X. Liu, H. Gao, J. E. Ward, X. Liu, B. Yin, Z. Wang, Ye Zhuo, D. J. F. Walker, J. Joshua Yang, J. Chen, D. R. Lovley, J. Yao, *Nat. Commun.* **2020**, *11*, 1861.
- [331] J. Feldmann, N. Youngblood, C. D. Wright, H. Bhaskaran, W. H. P. Pernice, *Nature* **2019**, *569*, 208.
- [332] L. Mennel, J. Symonowicz, S. Wachter, D. K. Polyushkin, T. Mueller, *Nature* **2020**, *579*, 62.
- [333] M. Rao, Z. Wang, C. Li, H. Jiang, R. Midya, P. Lin, D. Belkin, W. Song, S. Asapu, Q. Xia, J. J. Yang, in *2019 IEEE Int. Electron Devices Meeting (IEDM)*, IEEE, San Francisco, CA **2019**, 35.4.1.
- [334] Y. Zhai, Y. Zhou, X. Yang, F. Wang, W. Ye, X. Zhu, D. She, W. D. Lu, S.-T. Han, *Nano Energy* **2019**, 104262.
- [335] C. D. Danesh, C. M. Shaffer, D. Nathan, R. Shenoy, A. Tudor, M. Tadayon, Y. Lin, Y. Chen, *Adv. Mater.* **2019**, *31*, 1808032.
- [336] S. Park, A. Sheri, J. Kim, J. Noh, J. Jang, M. Jeon, B. Lee, B. R. Lee, B. H. Lee, H. Hwang, in *2013 IEEE Int. Electron Devices Meeting (IEDM)*, IEEE, Washington, DC **2013**, 25.6.1.
- [337] Z. Wang, S. Ambrogio, S. Balatti, S. Sills, A. Calderoni, N. Ramaswamy, D. Ielmini, in *2015 IEEE Int. Electron Devices Meeting (IEDM)*, IEEE, Washington, DC **2015**, 7.6.1.
- [338] B. J. Choi, A. C. Torrezan, K. J. Norris, F. Miao, J. P. Strachan, M.-X. Zhang, D. A. A. Ohlberg, N. P. Kobayashi, J. J. Yang, R. S. Williams, *Nano Lett.* **2013**, *13*, 3213.
- [339] S. Kim, S. Choi, J. Lee, W. D. Lu, *ACS Nano* **2014**, *8*, 10262.
- [340] S. Mandal, A. El-Amin, K. Alexander, B. Rajendran, R. Jha, *Sci. Rep.* **2015**, *4*, 5333.
- [341] D. Shang, P. Li, T. Wang, E. Carria, J. Sun, B. Shen, T. Taubner, I. Valov, R. Waser, M. Wuttig, *Nanoscale* **2015**, *7*, 6023.
- [342] S. Choi, P. Sheridan, W. D. Lu, *Sci. Rep.* **2015**, *5*, 10492.
- [343] B. J. Choi, A. B. K. Chen, X. Yang, I.-W. Chen, *Adv. Mater.* **2011**, *23*, 3847.
- [344] A. C. Torrezan, J. P. Strachan, G. Medeiros-Ribeiro, R. S. Williams, *Nanotechnology* **2011**, *22*, 485203.
- [345] J. J. Yang, M. X. Zhang, J. P. Strachan, F. Miao, M. D. Pickett, R. D. Kelley, G. Medeiros-Ribeiro, R. S. Williams, *Appl. Phys. Lett.* **2010**, *97*, 232102.



**Kaixuan Sun** received her B.S. degree in Microelectronics Science and Engineering from the school of Physics and Optoelectronic Engineering, Xiangtan University, China in 2018. He is currently a M.E. student at Hebei University. His current research interest is focused on the field of memristors and materials.



**Jingsheng Chen** received his Ph.D. degree from Lanzhou University, China in 1999. He joined the Nanyang technological University as a post-doctor in 1999–2001 and the Data storage Institute, A\*STAR as research scientist in 2001–2007. In the year of 2007, he joined National University of Singapore as an assistant professor and was promoted to associate professor in 2013. His research interest includes high anisotropy magnetic materials, spintronics, multiferroic materials, nanostructure magnetic materials and so on.



**Xiaobing Yan** is currently a professor at the School of Electronic and Information Engineering, Hebei University. He received his Ph.D. degree from Nanjing University in 2011. From 2014 to 2016, he held the Research Fellow position at the National University of Singapore. His current research interest is in the field of memristors and materials.